



Norwegian University of  
Science and Technology

# Monitoring of CO<sub>2</sub> Sequestration at the Longyearbyen CO<sub>2</sub> Lab by Time-lapse Seismic

An Interdisciplinary Rock Physics Study.

**Espen Rødland Mikkelsen**

Master of Science in Electronics

Submission date: June 2009

Supervisor: Åge Kristensen, IET

Co-supervisor: Tor Arne Johansen, UIB  
Martin Landrø, IPT



# Problem Description

As a part of the Longyearbyen CO<sub>2</sub> Lab, a Carbon Capture and Storage (CCS) pilot study is currently being conducted. As it is important to ensure that injected CO<sub>2</sub> stay in the formation for any foreseeable future, monitoring is a vital part of any CCS. Time-lapse seismic is a well proven monitoring technology, and is regarded the best monitoring option for this project.

Injection of CO<sub>2</sub> into a saline aquifer will normally give rise to large seismic anomalies. However, the target sandstone for this project is expected to be thin (5-30m), and have low porosity (5-15%), therefore it is not given that seismic monitoring will be possible.

This thesis will be a feasibility study of time-lapse seismic for monitoring of CO<sub>2</sub> injection at Svalbard, and should include the following aspects:

Build a 2-D rock physical model of the reservoir sandstone and overburden.

Perform seismic modeling to explore time-lapse signal as function of CO<sub>2</sub> saturation and pressure.

If possible, assess the repeatability of snow-streamer seismic data.

Based on results, assess the feasibility of seismic monitoring of the sequestration.

The models should be based on borehole logs and seismic from areas analogous to the planned injection well. Sources of data are seismic and borehole logs from the Reindalen and Adventdalen area.

A test well is currently being drilled at the planned injection cite, if borehole logs from this well are obtained within the timeframe of the thesis, a model for this area should be built and tested as well.

Assignment given: 16. January 2009

Supervisor: Åge Kristensen, IET





# Preface

As I type these words, my time as a student is over. This thesis marks the end of a long and fantastic journey which started out by studying satellites and stars, and ended up in the deep subsurface of the Earth. It's strange how things turn out.

The process of writing this thesis has at times been hard and many times frustrating, but most often inspiring and interesting. Without the help of many people, the previous sentence would be the other way around, therefore I would like to thank:

- My supervisors Åge Kristensen, Tor Arne Johansen, and Martin Landrø. Your help and expert advice have been of great help. A special thanks to Tor Arne, for inspiring the problem formulation for this thesis.
- Alvar Braathen. For having patience with me and not allowing me to draw faults all over the seismic sections.
- Isabelle Lecomte. For always putting me first in line at the Norsar Support, and for taking the time to teach me how to use SeisRox.
- Atle Mørk. For proofreading, and for teaching me the difference between a member and a Member.
- Erik Lindeberg at Sintef. For letting me use the CO2Therm software.
- StatoilHydro. For letting me use the Reindalspasset logg. A special thanks to Ola Eiken, for helping me obtain data and finding old Russian articles.
- UNIS. For enabling me to live at fantastic Svalbard for the duration of my thesis, and providing me with all practicalities I have needed.
- Markus Eckerstorfer. For proofreading, and being a great guy in general.
- All my fellow students. For making the last few years fly by. Best of luck to all of you.

Finally, I would like to thank my family and friends for their patience and support. A special thanks go to my parents, for their unconditional love and support, and for enabling me to follow my own paths, I will always be grateful for that.

Espen Rødland Mikkelsen

Longyearbyen, June 19, 2009



# Abstract

One of the great technical challenges of our century is how to reduce the emission of CO<sub>2</sub>. Part of the solution to this problem can be Carbon Capture and Storage (CSS). To store captured CO<sub>2</sub> in geological formations, is called sequestration, and a pilot study is currently being performed to assess the possibility of CO<sub>2</sub> sequestration in Svalbard.

A vitally important issue with any CSS, is to ensure that the injected CO<sub>2</sub> actually stay in the geological formation for any foreseeable future. This means that monitoring is vital. Time-lapse seismic has successfully been used to monitor CO<sub>2</sub> as it migrates through the underground, and this is considered the best monitoring object for the Longyearbyen CO<sub>2</sub> Lab.

The target sandstone of this project is expected to be of poor quality, with low porosities(5-15%) and permeabilities(approximately 1mD). Therefore, it is not certain that the sequestration will lead to time-lapse signals that are above detectability limits.

This thesis is a first assessment of the feasibility of monitoring by time-lapse seismic. The problem is approached by asking four questions:

- Will time-lapse seismic be able to monitor CO<sub>2</sub> migrating in the reservoir?
- Will time-lapse seismic be able to separate pressure and saturation effects?
- Will time-lapse seismic be able to quantify pressure states, and volumes of CO<sub>2</sub> in the reservoir?
- Will time-lapse seismic be able to detect small CO<sub>2</sub> accumulations leaked into the overburden?

The answers to these questions are sought by using a combined rock physical and seismic model. The sandstone is modeled by Differential Effective Medium theory, and the effect of increasing pressure is modeled by its effects on pore geometries. The seismic model is based on interpretation of a seismic line crossing the area of the planned injection well. Four sandstone units are defined in the reservoir interval.

The seismic modeling is performed by the SIMPLi algorithm. Five cases are investigated, simulating monitor surveys for six months, one year, five years and 10 years after injection start. In addition a case for leakage into the overburden is modeled.

The results from the modelling show that  $V_P$  is most influenced by variations in saturation, with a maximum relative change of -7%. Changes in  $V_S$  are dominated by pressure variations, with a maximum change of -3%. Maximum change in amplitudes for pressure increase is about 50%, for saturation increase the maximum change is about 200%. Maximum time shifts are found to be -2.65ms.

Areas with saturations of CO<sub>2</sub> show strong amplitude anomalies in the synthetic seismic, and it is possible to observe the migration of the CO<sub>2</sub>. Strong tuning effects are evident at all reservoir units. The addition of noise masks the time-lapse signal from areas of small saturation/pressure changes. By combining relative changes in amplitude, time shifts and qualitative AVO-observations, the possible range of saturation/pressure states causing a time-lapse anomaly, could be narrowed down to a relatively small range.

From the results, it is concluded that monitoring of migration is feasible given CO<sub>2</sub> saturations above 10%. Quantification and separation of pressure and saturation levels, are not considered

feasible, this is in part due to strong tuning effects. Leaks in the order of 1000 tonnes will be detectable in the deep overburden, while leaks of a few hundreds of tonnes will be detectable above 500m.

# Contents

<b>List of Figures</b>	<b>vi</b>
<b>List of Tables</b>	<b>viii</b>
<b>1 Introduction</b>	<b>1</b>
1.1 The Longyearbyen CO <sub>2</sub> Lab . . . . .	1
1.1.1 Geological setting of project . . . . .	2
1.1.2 Monitoring . . . . .	4
1.2 Scope and outline . . . . .	6
<b>2 Theories of rock physics and seismic modeling</b>	<b>7</b>
2.1 The effective Medium . . . . .	7
2.1.1 Inclusion based models . . . . .	8
2.1.2 The effects of porefluids . . . . .	11
2.1.3 The effects of pressure . . . . .	12
2.2 The SIMPLi Seismic modeling algorithm . . . . .	14
2.3 Time-lapse seismic attributes and metrics . . . . .	15
2.3.1 Time-lapse attributes . . . . .	15
2.3.2 Repeatability and detectability . . . . .	17
<b>3 A rock physical model of the reservoir sandstone</b>	<b>19</b>
3.1 Data sources . . . . .	19
3.2 The dry rock . . . . .	20
3.2.1 The mineral matrix . . . . .	20
3.2.2 Adding pore space . . . . .	21
3.3 The effects of CO <sub>2</sub> saturation and pore pressure increase . . . . .	22
<b>4 A seismic model of the reservoir</b>	<b>25</b>
4.1 Data sources . . . . .	25
4.2 Seismic interpretation . . . . .	25
4.3 From interpretation to seismic model . . . . .	28
<b>5 Integrating the two models and performing seismic modeling</b>	<b>30</b>
5.1 Integrating the two models . . . . .	30
5.2 Seismic modeling . . . . .	31
5.2.1 Modeling time-lapse signal of CO <sub>2</sub> migrating in the reservoir . . . . .	31
5.2.2 Modeling time-lapse signal of CO <sub>2</sub> leaking into the overburden . . . . .	32
<b>6 Modeling results and analysis</b>	<b>35</b>
6.1 Results from the rock physical modeling . . . . .	35
6.1.1 Velocity changes . . . . .	35
6.1.2 Amplitude changes . . . . .	37
6.1.3 Time shifts . . . . .	38

6.1.4	AVO-signature . . . . .	38
6.2	Synthetic seismic . . . . .	38
6.2.1	Qualitative observations . . . . .	40
6.2.2	Quantification of changes . . . . .	42
6.3	Leakage detection . . . . .	48
<b>7</b>	<b>Discussion</b>	<b>51</b>
7.1	Feasibility of seismic monitoring . . . . .	51
7.1.1	Monitoring migration of CO <sub>2</sub> in the reservoir . . . . .	52
7.1.2	Separating pressure and saturation effects and quantification of changes . .	53
7.1.3	Detecting Leakage . . . . .	54
7.2	On the validity of the results . . . . .	54
<b>8</b>	<b>Summary and conclusions</b>	<b>57</b>
8.1	Summary and conclusions . . . . .	57
8.2	Future work . . . . .	58
	<b>References</b>	<b>59</b>
<b>A</b>	<b>Lithological logs from drill cores in Dh2</b>	<b>65</b>
<b>B</b>	<b>Electrical logs from Dh2</b>	<b>71</b>

# List of Figures

1.1	Stratigraphic column for the Adventdalen area [modified from Braathen et al., 2009]	2
1.2	Picture showing a De Geerdalen sandstone outcropping at Edgeøya. The sandstone unit is indicated with red arrows. Sandstones form cliffs in mountain sides, while shales often are covered with scree. (Foto: Atle Mørk)	4
1.3	Map showing the area of the Longyearbyen CO <sub>2</sub> lab. The red lines indicate positions of the cross sections in the lower part of the figure. The yellow polygons are the locations of the drilled and planned wells (Dh1+2 to the west, Dh3+4 to the east). In the crosssection, the red layer is the De geerdalen Formation, while the blue layer is the Permian Kapp Starostin Formation. The cross section shows how the strata dip gently upwards to the NE. The De Geerdalen Formation outcrops in De Geerdalen, 15km from the injection site. [modified from Mørk, 2008]	5
2.1	Illustration of first order scattering theory. a) Incident wave in a homogeneous background medium with inclusions. b) Scattered waves are drawn as dotted lines, except in direction of propagation. c) First order scatter contributions. d) Effective wave, observed from a distance » wavelength.	8
2.2	Illustration of Kuster-Toksöz theory. An effective wave can be described by: a) Sum of incident wave and scatter from each inclusion, or by: c) Sum of incident wave and a scattered wave from an effective inclusion, calculated from b)	9
2.3	The aspect ratio, $\alpha$ is defined as the ratio of the short and long half axis of an ellipse.	10
2.4	Illustration of the illumination vector $\mathbf{k}_s$ as the difference between two slowness vectors $\mathbf{k}_s$ , and $\mathbf{k}_r$ . [from Lecomte et al., 2003]	14
2.5	Illustration of offset dependent time shifts. The dark grey area represent an area with velocity change. The red ray will travel longer through the area of changed velocity, thus will it experience more time shift.	16
3.1	Thin-section of a sandstone in the De Geerdalen Formation [modified from Knarud, 1980]. The red arrows show low aspect ratio pores/cracks between Quartz grains, while the blue arrow shows an oblong shaped Muscovite mineral. The scale of this image is 1mm x 1mm	20
3.2	Properties of CO <sub>2</sub> as function of pressure, temperature, and depth.	23
4.1	Line 1. The depth migrated seismic line that crosses the injection site in Adventdalen.	26
4.2	A coarse illustration of the key seismic horizons in Line 1. The predicted stratigraphic column, with depths of the different geological formations are given in the left of the figure. Colors of horizons correspond to the formation with the same color in the column. The black line indicates the location of the planned injection well, while the dotted line indicates the reservoir interval	27
4.3	Picture showing a dolerite intrusion in Svalbard. The intrusion can be seen as a dark diagonal across the mountain side. [from Andresen, 2007]	28
4.4	The 2D reservoir model. Colors indicate P-velocity. The sandstone units in the reservoir zone can be seen as three layers with vertical separators. The red line indicates the location of the planned injection well.	29

5.1	The 2.5D reservoir model. The model properties varies in the x-and z-directions, but not in the y-direction. The figure is scaled in the z-direction for display purposes.	30
5.2	Flow chart of the process from gathering of data to generating synthetic seismic data.	31
5.3	Modeled saturation and pressure distributions in the reservoir over 10 years . . . .	32
5.4	2D model built to explore the effects of leakage in the overburden. The high angled lines represents fault zones, while the wedge shaped blocks represent CO <sub>2</sub> accumulation is aquifers. The aquifers are located at approximately 450m, and 600m, respectively above and below the critical point for CO <sub>2</sub> . . . . .	33
6.1	Predicted relative changes in $V_P$ , $V_S$ , density, and $V_P/V_S$ as a function of pressure changes and saturation. . . . .	36
6.2	Predicted relative changes in AI and amplitude as a function of pore pressure increase and saturation of CO <sub>2</sub> . . . . .	37
6.3	Predicted time shifts as a function of pore pressure increase and saturation of CO <sub>2</sub> .	38
6.4	Predicted AVO signature for the upper reservoir sandstone. . . . .	39
6.5	The baseline synthetic seismic. The upper reservoir sandstone is located at the reflector at 900m. The 5m sandstone is located in the interval of smeared reflections at 950-1000m. The 15m sandstone is located at the reflector at 1000m, while the basal 20m sandstone is located at the 1100m reflector. . . . .	40
6.6	Synthetic monitor surveys and difference sections six months, one year, five years, and 10 years after injection start . . . . .	41
6.7	Comparison of difference sections with and without noise. . . . .	42
6.8	Predicted and picked relative changes in amplitude. . . . .	43
6.9	Possible values of saturation and pressure increase for the relative amplitude change for the uppermost sandstone at trace 70. The pressure range is 0-50bar, and saturations of 0.45 to 0.55. . . . .	44
6.10	Possible values of saturation and pressure increase for the combined time shift, and relative amplitude change, for the uppermost sandstone at trace 70. The pressure range is now 0-35bar, and saturations of 0.45 to 0.55.s . . . . .	45
6.11	Intercept-Gradient crossplot for the reservoir zones; 0.5, 1, 5, and 10 years after injection start. Points marked with red represent the six month data. Zone 3 deviates strongly, suggesting a non existent pressure drop after 10 years. . . . .	46
6.12	Synthetic seismic of overburden . . . . .	49
6.13	Synthetic seismic of overburden . . . . .	50
7.1	Velocity versus porosity for the sandstone modelled with DEM, Critical Porosity Model, and KT-model. Velocity drops steeply for the KT and DEM models due to presence of low aspect ratio pores. . . . .	55
A.1	Carolinefjellet Formation . . . . .	66
A.2	Helvetiafjellet Formation . . . . .	67
A.3	Rurikfjellet Formation . . . . .	68
A.4	Agardfjellet Formation . . . . .	69
A.5	Agardfjellet Formation, Willhelmøya subgroup, and Isfjorden Member . . . . .	70



# List of Tables

3.1	Mineral composition of modelled sandstone. Elastic moduli and densities are taken from Mavko et al. [1998], volume fractions are based on mean values from 45 samples in Knarud [1980], and aspect ratios are interpreted from images of thin sections in the same study. . . . .	21
3.2	Calculated elastic moduli and density of mineral matrix. Calculations are done using the KT-model based on the properties listed in Table 3.1 . . . . .	21
3.3	Properties measured in the Reindalpasset well. . . . .	22
6.1	Interpretation help for the $\Delta R_0/\Delta G$ -plot. The signs indicate polarity and magnitude of the changes. . . . .	45



# Chapter 1

## Introduction

In recent years, the battle against global warming and climate change has received enormous attention throughout the world. Few people now deny the possibility that global warming is man made, and the main culprit is emission of  $\text{CO}_2$ . About 44% of  $\text{CO}_2$  emissions in Norway come from stationary sources [SSB, 2008], while in Europe, about 27% come from electricity and heat production [EEA, 2008]. The potential reduction in emissions if these sources could be minimized, are enormous. This is the reason Carbon Capture and Storage (CCS) have gained much attention as a part of the solution to the  $\text{CO}_2$  problem. In one sentence CCS can be described as follows:  $\text{CO}_2$  is captured at some industrial process, then compressed and transported to a storage site, and injected underground where it is stored in a geological formation.

Many CCS storage sites exist around the world, the two most common storage types are in deep saline aquifers, and depleted hydrocarbon reservoirs. Examples of the latter are the McElroy Field in Texas, the Weyburn Field in Canada, and the Nagaoka field in Japan [Wang et al., 1998; Li, 2003; Onishi et al., 2007]. Examples of saline aquifer projects are the Sleipner field in the North Sea [Eiken et al., 2000; Arts et al., 2004], the In Salah field in Algeria [Ebrom et al., 2006], and the  $\text{CO}_2$ SINK project in Germany [Schilling et al., 2009].

In vanAlphen et al. [2007], the societal acceptance of CCS projects is analyzed, one of the conclusions in this analysis is that the main concern in the public opinion of CCS, is the long term safety. Indeed, the most vital success criteria for  $\text{CO}_2$  sequestration, is that the  $\text{CO}_2$  actually stays in the formation for any foreseeable future. To ensure this, effective monitoring techniques are essential. Luckily, decades of geophysical research in the hydrocarbon industry have provided many monitoring tools directly applicable to  $\text{CO}_2$  sequestration. This thesis will only focus on seismic monitoring methods, and especially surface seismic.

Norway has been a vanguard nation in CCS research, with the Sleipner project as the world's first on an industrial scale. Continued effort and research is necessary to develop technology and knowledge about CCS, this is the motivation behind the Longyearbyen  $\text{CO}_2$  Lab.

### 1.1 The Longyearbyen $\text{CO}_2$ Lab

Longyearbyen is the largest settlement in the Svalbard archipelago, and is one of the world's northernmost towns. The town developed as a mining community with several coal mines nearby. Today, tourism, education and research play as important roles as mining. The University Center in Svalbard (UNIS) was opened in 1993, and is a cooperation between all the Norwegian universities.

Longyearbyen represents a closed energy system: It has coal mines, a coal fueled power plant, and geological structures suited for  $\text{CO}_2$  sequestration, thus allowing for a demonstration of the entire  $\text{CO}_2$  value chain. The Longyearbyen  $\text{CO}_2$  Lab is a UNIS initiative, aimed at turning Longyearbyen into a CCS research, testing and demonstration site.

The first stage of the project is to identify a saline aquifer suitable for sequestration. This work started in 2007 with the drilling of two test wells, and continued with seismic acquisition and a third well in 2008. This work have verified a 400m thick, sealing package of shales, and an impermeable near-surface layer of permafrost. The presence of sandstones below the cap rock have also been verified, but the depth of the most promising geological formation has yet to be reached. A fourth well will be drilled in the summer of 2009 with the aim to verify the reservoir.

The planned next stages will start when the fourth well has been drilled. Pilot-scale injection tests will be performed both in the reservoir, and on drill cores. This will establish important parameters such as porosity and permeability. If the reservoir quality is satisfactory, the next stages of the project will include CO<sub>2</sub> capture at the local coal power plant, followed by injection. When the lab is fully operational, an injection rate of 80.000t/year is planned.

### 1.1.1 Geological setting of project

The planned location for the CO<sub>2</sub> injection is situated in Adventdalen close to Logyearbyen. The target formation is the Triassic De Geerdalen Formation, overlain by about 1000m of Jurassic and Cretaceous strata. This section will give a brief description of the sediments that make up the cap rock and the reservoir, as well as a description of the relevant structural geology. A simplified stratigraphic column of the Adventdalen area can be seen in Figure 1.1.

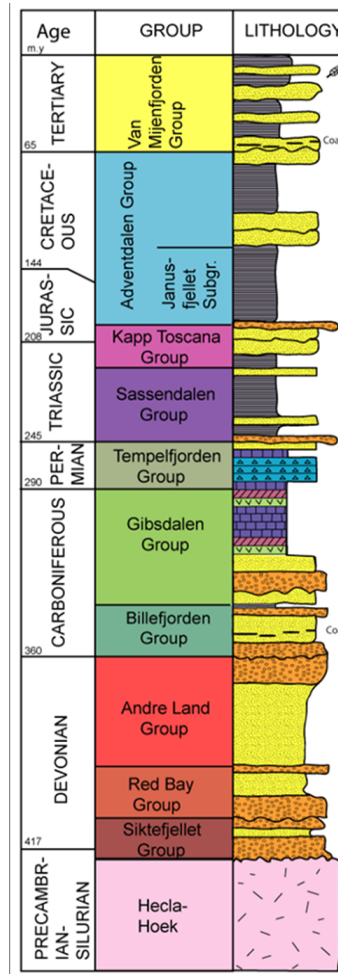


Figure 1.1: Stratigraphic column for the Adventdalen area [modified from Braathen et al., 2009]

### Stratigraphy, Cretaceous-Triassic

This description is based on drillcores from the three drillholes, lithological logs from these can be found in Appendix A. The description will be done from the surface down with depth intervals indicated for each formation. Depth intervals with question marks can not be absolutely determined from drill cores, and are therefore a prognosis.

- (0-65m) The Quarternary cover: About 65m thick layer of morrain blocks and scree
- Adventdalen Group (Cretaceous):
  - (65-120m) Carolinefjellet Formation: Deposited in a prodelta to distal marine shelf environment, the Carolinefjellet Formation. is dominated by alternating shale-sandstone of one to 10m scale [Dallmann et al., 2001].
  - (120-180m) Helvetiafjellet Formation: Characterized by a range of facies, from fully fluvial to marginal marine. This formation is dominated by sandstones, with subordinate shales [Mørk et al., 1999].
  - (180-405m) Rurikfjellet Formation: Deposited in a regressive marine environment, dominated by dark shale, often with siderite concretions. The formation coarsens upwards to siltstones. At the boundary between Rurikfjellet and Agardfjellet, the Myklegardfjellet bed is found. This is a plastic clay, and may be a major dislocation zone, which is indicated by heavily faulted shales in the drillcores [Braathen et al., 2009].
- Adventdalen Group (Jurassic):
  - (405-700?) Agardhfjellet Formation: Sandstone and intraformational mudrich conglomerates. The formation fines upwards from mud rich sandstones, trough siltstones, to a thick package of organic rich shale [Mørk et al., 1999]. This formation will be the primary caprock for the CO<sub>2</sub> sequestration.
- Kapp Toscana Group (Jurassic-Triassic):
  - (700-725?) Willhelmøya Subgroup: Conglomerates at top and base are good regional markers, in between the conglomerates are alternating claystones and thin sandstones.
  - (725-820?) De Geerdalen Formation, Isfjorden Member: The deepest point reached by drilling is within the Isfjorden Member, comprised of alternating claystone and sandstone beds, deposited in shallow marine shelf environments [Mørk et al., 1999]. Drillcores from this member show sandstones with low porosity and permeability, but these sandstones are known to be better cemented than those further below [Braathen et al., 2009].
  - (820-1025?) De Geerdalen Formation: This is the target formation. It is expected to be a 300m thick, repeated coarsening upwards successions from shale to sandstone, deposited in a shallow marine to deltaic environment. The sandstones are compositionally immature, and is expected to be well cemented. The sandstones are known to be up to 30m thick.

The De Geerdalen Formation outcrops at several locations in Svalbard, the closest outcrop to Adventdalen is located in De Geerdalen, 15km NE of the injection site. In outcrops, sandstones form cliffs in the mountain side, while shales are often covered by scree, this is the reason for the characteristic stair case-pattern seen in mountainsides all over Svalbard. Figure 1.2, shows a massive sandstone in the De Geerdalen Formation in an outcrop at Edgeøya.



Figure 1.2: Picture showing a De Geerdalen sandstone outcropping at Edgeøya. The sandstone unit is indicated with red arrows. Sandstones form cliffs in mountain sides, while shales often are covered with scree. (Foto: Atle Mørk)

### Structure and tectonics

The Adventdalen area is situated on the north-eastern flank of the Spitsbergen Central Tertiary Basin (CTB). The CTB is a foreland basin that was formed during the Early Tertiary opening of the Fram Strait. During this period, Svalbard was forced around the NE corner of Greenland, causing a transpressional regime. This resulted in an orogenic belt to the west, and a foreland basin to the east, the CTB [Andresen, 2007].

The strata in Adventdalen have a general dip to the southwest, and in the middle of Adventdalen the dip angle changes, as seen in Figure 1.3, the steepest dipping part has an angle of about  $3^\circ$ . In the figure, the blue layer is the Permian Kapp Starostin Formation, and the red layer is the De Geerdalen Formation, while the black lines are detachment zones. A system of detachment faults, so-called decollement faults, is found at two stratigraphic depths; Middle Triassic (Botneheia Fm.) and Middle/Upper Jurassic (Agardfjellet/Rurikfjellet Fm.). These faults originate from the western fold-thrust belt, caused by the above mentioned Tertiary transpressional regime. The faults are found in shales which act as lubricants for the movements, and are mainly oriented parallel to bedding [Dallmann et al., 2001]. Strata above these detachments have been thrust several kilometers in the ENE-direction. Ramps are also known to occur in relation to the decollement faults. One of these ramps are found at Grumantbyen, near Adventdalen, this ramp has an angle of  $30^\circ$  and reaches the surface.

The faulted zone encountered in the drilling in the Myklagarden bed, is thought to be the upper decollement zone. Drilling problems due to instabilities in this zone, are the main reason the drillholes have not reached the target depth.

#### 1.1.2 Monitoring

CCS projects require a range of monitoring techniques to ensure that  $\text{CO}_2$  in fact stays in the underground. The planned monitoring techniques for the Longyearbyen  $\text{CO}_2$  lab include surface seismic and observation wells. However, the portfolio of techniques is likely to increase as the project goes along. Other methods may include micro seismic, gravimetry, and surface leakage detectors.

Time-lapse cross-well seismic have been used at Nagaoka [Onishi et al., 2007], VSP and surface seismic at the McElroy field [Wang et al., 1998], and time-lapse seismic at the Sleipner field [Eiken et al., 2000; Arts et al., 2004] and the Weyburn field [Li, 2003]. The scale of these projects vary from 10.000 tonnes injected at Nagaoka, to approximately 20 million tonnes injected at Sleipner.

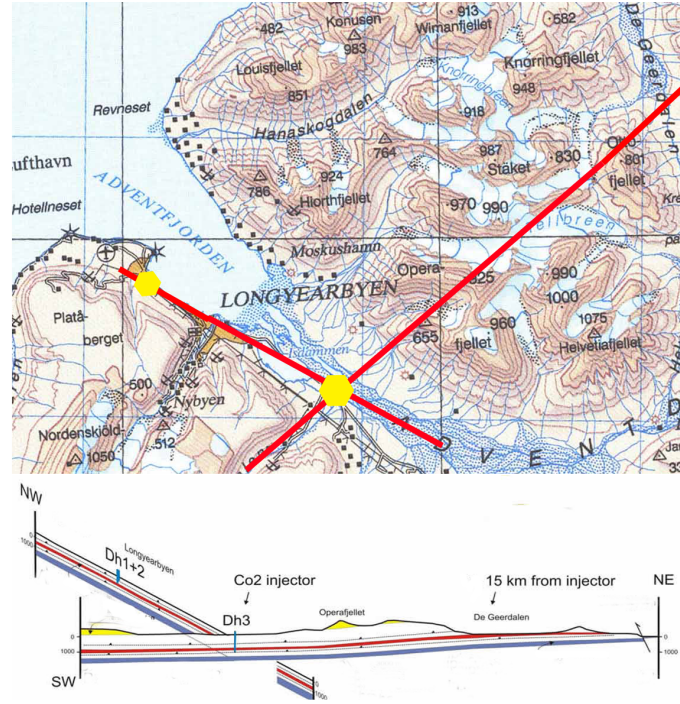


Figure 1.3: Map showing the area of the Longyearbyen CO<sub>2</sub> lab. The red lines indicate positions of the cross sections in the lower part of the figure. The yellow polygons are the locations of the drilled and planned wells (Dh1+2 to the west, Dh3+4 to the east). In the crosssection, the red layer is the De geerdalen Formation, while the blue layer is the Permian Kapp Starostin Formation. The cross section shows how the strata dip gently upwards to the NE. The De Geerdalen Formation outcrops in De Geerdalen, 15km from the injection site. [modified from Mørk, 2008]

By applying methods of combined rock physics and seismic measurements, all these projects have been successful in monitoring the migration of the CO<sub>2</sub> plume. To date, none of the projects have reported any leakage.

The preferred land seismic acquisition technique in Svalbard have been snowstreamer surveys [Eiken, 1985]. The operation of this is much like a marine acquisition; A belt wagon tows a 1.5km streamer, stopping for each shot, dynamite is used as source, and is laid out in front of the belt wagon, or behind the streamer for each shot. The streamer has 60 channels, each with 8 geophones. This method has the advantage of being efficient and flexible compared to conventional surface seismic. However, this equipment is quite old, and is fully analogue. Also, the equipment is limited to 2D acquisition, with possibilities for pseudo-3D.

As this project is still in the planning and verification stage, a monitoring plan has not been decided upon yet. The possibilities of using vibroseis, and permanently installed surface geophone arrays, are being explored. The option of producing a digital snowstreamer, is also being considered.

Regardless of seismic method, the objectives are the same; Monitor extent of CO<sub>2</sub> plume, identify CO<sub>2</sub> accumulations outside the De Geerdalen Formation, and detect leakage. The reservoir sandstone is expected to have very low permeability, and so pressure build-ups can be expected close to the injection well and at sealing structures. Pressure build-up at the caprock can also be expected, and it is important that this pressure does not exceed values where hydrologic fracturing can occur. Therefore, the monitoring should also be able to identify areas of high pressure build-up. Surface seismic can in many cases qualitatively identify pressure and saturation changes, but may prove difficult in use of quantification of the same properties.

## 1.2 Scope and outline

The Longyearbyen CO<sub>2</sub> Lab is special in the sense that the target reservoir is expected to be of relatively poor quality. Low permeabilities and porosities pose a problem both for injection, and the subsequent monitoring. Despite all the advances in time-lapse seismic the last two decades, it is not given that the injection into a De Geerdalen sandstone, will give a time-lapse signal that is detectable.

This study is a first assessment of the feasibility of monitoring by time-lapse seismic. The limits in the available data at this early stage, pose a challenge and calls for a thorough research of the available information of the reservoir sandstone. Although much literature exist on time-lapse seismic in general, and monitoring of CO<sub>2</sub> especially, little literature exist on time-lapse monitoring of production or sequestration in low porosity sandstones.

The assessment of feasibility give rise to four question that are central in this study:

- Will time-lapse seismic be able to monitor CO<sub>2</sub> migrating in the reservoir?
- Will time-lapse seismic be able to separate pressure and saturation effects?
- Will time-lapse seismic be able to quantify pressure states, and volumes of CO<sub>2</sub> in the reservoir?
- Will time-lapse seismic be able to detect small CO<sub>2</sub> accumulations leaked into the overburden?

All the work done in this study revolve around these four questions. The answers have been sought by applying a interdisciplinary method of seismic interpretation, rock physical modeling, seismic modeling and quantitative seismic analysis.

The thesis is structured as follows: Chapter 2, introduces theories for rock physical models, seismic modeling and time-lapse seismic. The theories of rock physical modeling is implemented to build a rock physical model of the reservoir sandstone in Chapter 3. The effects of CO<sub>2</sub> saturation and pore pressure changes on the seismic parameters of the sandstone, are modeled in this chapter.

The building of a 2D seismic model from interpreted seismic in the Adventdalen area is described in Chapter 4, while the rock physical and seismic model are integrated in Chapter 5. In this chapter, the seismic modeling process is also described. Also, a set of cases is developed to investigate the four questions raised above.

An overview and analysis of the results from the rock physical and seismic modeling are presented in Chapter 6, before the results are discussed in Chapter 7. The discussion will focus on the four questions, and will highlight some of the assumptions made, and the impact these may have on the validity of the results.

Finally, in Chapter 8 a summary and conclusions are presented, along with suggestions for continuance of this work.



## Chapter 2

# Theories of rock physics and seismic modeling

In this chapter, theories for rock physical modeling are described with emphasis on theories implemented in this study. Chapter 2.1 gives a general description of effective medium theories, before going into details on three specific models in the subsequent chapters. Theory for the effects of pressure on seismic parameters are described in Chapter 2.1.3. Finally, Chapter 2.2, give a short introduction to the theory of the method used to produce synthetic seismic.

### 2.1 The effective Medium

Rock physical models describe how macroscopic observations such as seismic, relate to a rock's microscopic structure. Seismic measurements provide information about velocities and densities, which in turn give information about elastic parameters such as bulk and shear moduli. A rock physical model must describe how these parameters are influenced by mineral composition, grain contacts, pore geometry, porosity, and porefluids. This is generally done by combining properties of a rock's constituents into an effective medium.

In reflection seismic, the two most important properties of the rock are the velocities and densities, since the product of these, the acoustic impedance (AI), is what dictates the reflectivity. The pressure- and shear-wave velocities,  $V_P$  and  $V_S$ , can be found by:

$$V_P = \sqrt{\frac{K + \frac{4}{3}\mu}{\rho}} \quad (2.1)$$

$$V_S = \sqrt{\frac{\mu}{\rho}} \quad (2.2)$$

Where  $K$ , is the bulk modulus;  $\mu$ , the shear modulus; and  $\rho$ , the effective density of the porous rock. In essence, these quantities, and how rock physical parameters affect them, are what the next sections will explore.

Numerous attempts have been made to develop theoretical models for porous rocks, ranging from simple averaging methods, to scattering models, and granular media models. Hill [1952] showed that the Reuss and Voigt averages are upper and lower bounds for elastic moduli of an aggregate of minerals. Hashin and Shtrikman [1963] formulated bounds with a narrower range, and are thus more accurate than the Voigt and Reuss bounds. The Hill average can be used to give an estimate of the elastic moduli as the arithmetic mean of the upper and lower bounds. These theories can be applied without any knowledge of the geometry of the mineral aggregate and pore space, and therefore serve as easily implemented, but often inaccurate models for effective elastic properties. A more detailed description of these theories can be found in Mikkelsen [2008].

In grain contact theory, rocks are modeled as a packing of identical spheres, used as idealized shapes for pores and mineral grains. One of the most widely used contact theories is the Hertz-Mindlin model [Mindlin, 1949] which models the normal and tangential contact stiffness between two identical spherical grains as a function of Poisson's ratio, porosity, pressure and average number of contact points between the grains. Several extensions to the Hertz-Mindlin model exists. Dvorkin and Nur [1996] developed a model for cemented and uncemented sandstones, where cement are deposited *at* grain contacts and *away* from grain contacts respectively, thus allowing contact models to include effects of cementation. The grain contact models can be used to predict elastic behavior of high porosity granular rocks [Mavko et al., 1998].

Low porosity sandstones are often modeled using inclusion theory, this approach will be described in the next section.

### 2.1.1 Inclusion based models

The inclusion based models are described by Johansen and Gelius [2008], and apply scattering theory to model an effective medium. The effective medium in inclusion models are approximated by a homogeneous medium with elastic parameters  $K_m$  and  $\mu_m$ , to which inclusions with elastic parameters  $K_i$  and  $\mu_i$  are added. A P-wave propagating through this medium will be scattered by the inclusions. The nature of the scattering will be dependent on the boundary conditions between the homogeneous medium and the inclusions. Boundary conditions will in turn be dependent on both medias elastic properties. The scattered waves will propagate radially away from the inclusions, interacting with other scattered waves, being scattered from other inclusions, and form a complex wavefield of P- and S-waves. The inclusion models seek to describe this scatter pattern as one effective wave, by summing the incoming and scattered waves.

The most widely used inclusion models are first order approximations, and only consider scattered energy in the direction of propagation of the original P-wave, the cartoon in Figure 2.1 illustrates this approximation. The incident wave in a) interact with the colored inclusions. In b) the scattered waves from the inclusions are drawn as dotted lines, the scattered waves in the direction of propagation are drawn with solid lines. Ignoring scatter-scatter interactions, the contributions from the first-order scatters are drawn in c). Assuming the wavelength  $\lambda$ , to be much larger than the inclusions, the composite wavefield observed at a distance  $r \gg \lambda$ , can be assumed to be moving in phase, and be observed as one wave in d).

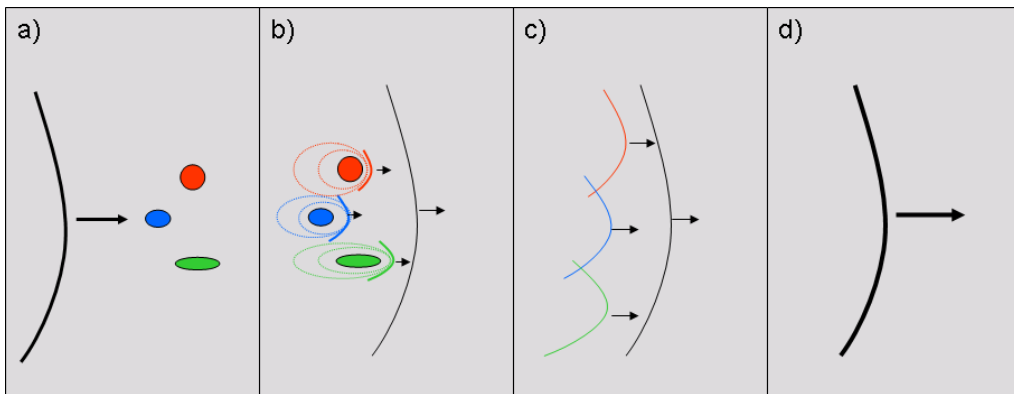


Figure 2.1: Illustration of first order scattering theory. a) Incident wave in a homogeneous background medium with inclusions. b) Scattered waves are drawn as dotted lines, except in direction of propagation. c) First order scatter contributions. d) Effective wave, observed from a distance  $\gg$  wavelength.

A consequence of the first order approximation is that no inclusions can interact, as the scatter from one inclusion then would affect other nearby scatters. This means that the inclusions are

not connected, and in the case of inclusions as pore space, this means the rock is strictly non-permeable.

### The Kuster-Toksöz Model

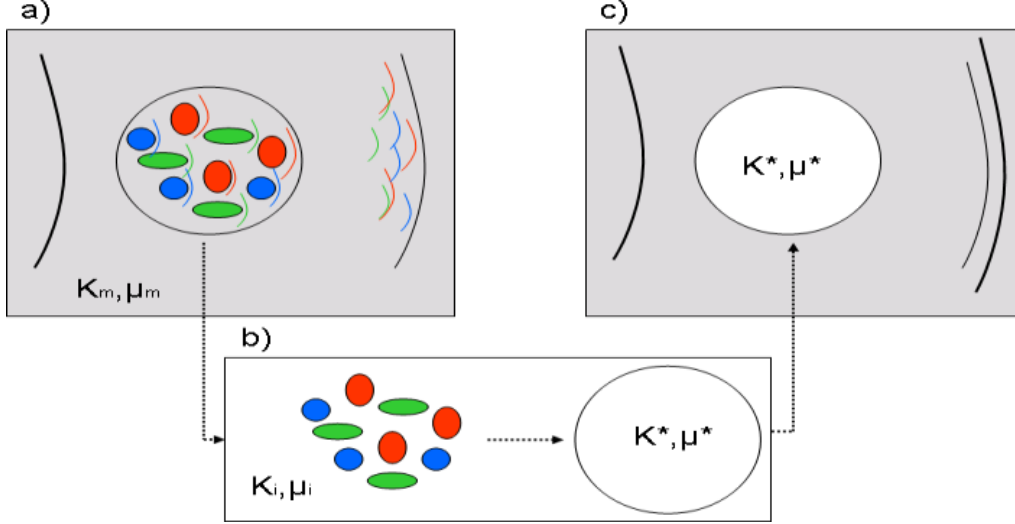


Figure 2.2: Illustration of Kuster-Toksöz theory. An effective wave can be described by: a) Sum of incident wave and scatter from each inclusion, or by: c) Sum of incident wave and a scattered wave from an effective inclusion, calculated from b)

Kuster and Toksöz [1976] derived an effective medium model by using first order scattering theory. The effective medium is now modeled as a homogeneous medium with properties  $K_m$  and  $\mu_m$  in which  $N$  inclusions with properties  $K_i$  and  $\mu_i$ , are introduced. The homogeneous medium will henceforth be called the background medium, while the inclusions will, unless otherwise stated, be pores. This situation is illustrated in Figure 2.2. A wave travelling through this medium can be described either by:

- The sum of the incident wave and the scattered waves from  $N$  inclusions, as illustrated by a) in Figure 2.2.

Or, by:

- The sum of the incident wave, and a scattered wave from an effective spherical inclusion with properties  $K^*$  and  $\mu^*$ , calculated from the  $N$  inclusions. This is illustrated by b), and c) in Figure 2.2.

This yields two equations with two unknowns,  $K_{KT}^*$  and  $\mu_{KT}^*$ . In a medium with multiple inclusions with  $N$  different inclusion geometries, these equations can be written:

$$\frac{(K_m - K_{KT}^*)(K_m + \frac{4}{3}\mu_m)}{K_{KT}^* + \frac{4}{3}\mu_m} = \phi \sum_{i=1}^N c_i (K_m - K_i) P^{mi}, \quad (2.3)$$

$$\frac{(\mu_m - \mu_{KT}^*)(\mu_m + \zeta_m)}{\mu_{KT}^* + \zeta_m} = \phi \sum_{i=1}^N c_i (\mu_m - \mu_i) Q^{mi}, \quad (2.4)$$

where  $\phi$  is the porosity, and  $c_i$  the concentration of pores with aspect ratio  $\alpha_i$ .  $P^{mi}$  and  $Q^{mi}$  are coefficients describing the effects of pore geometry and elastic properties; an overview for different geometries can be found in Mavko et al. [1998].  $\zeta$  is an elastic coefficient defined as  $\zeta = \frac{\mu}{6} \frac{9K+8\mu}{K+2\mu}$ .

The pore aspect ratio  $\alpha$  is defined as the ratio of the short and long half-axis of the pore, this is illustrated in Figure 2.3. A spherical pore will have an aspect ratio of one, while pores with elliptical shapes will have aspect ratios less than one. In general, a rock will contain pores with an infinite range of aspect ratios, but a finite number of discrete aspect ratios can be used as an approximate. The range of aspect ratios are described by an aspect ratio spectrum defined by  $\mathbf{c}(\alpha)$ , containing the concentration  $c_i$  of pores with aspect ratio  $\alpha_i$ . Low aspect ratio pores will be more compressible than high aspect ratio ones, thus a rock with a high concentration of low aspect ratio pores will be more compressible, and will have lower velocities. The Pore aspect ratio can be as important as porosity in controlling the velocity of a rock [Eastwood and Castagna, 1983].

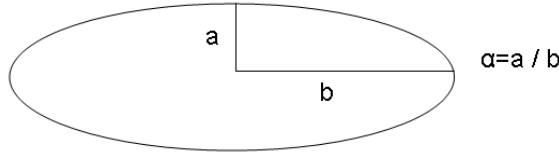


Figure 2.3: The aspect ratio,  $\alpha$  is defined as the ratio of the short and long half axis of an ellipse.

As mentioned, the first-order approximation requires no interaction between pores, this means that no pore fluid can flow from one pore to the next. As a consequence, this model is only valid for low porosity rocks. This requirement imposes the following constraint on the pore geometry:

$$\sum_{i=1}^N \frac{c(\alpha_i)}{\alpha_i} < 1 \quad (2.5)$$

The constraint in 2.5 shows that KT can model higher porosity rocks if the pores are spherical. This is because pores with high aspect ratio can make up a large porosity without overlapping, while low aspect ratio pores reduces maximum porosity before overlapping occurs [Johansen and Gelius, 2008]. Since the pores in the inclusion models do not interact, the inclusion models simulate high frequency behavior. This means that fluid-filled pores should be modelled with dry pores ( $K_i = \mu_i = 0$ ), with subsequent saturation using Gassmann's relations [Mavko et al., 1998].

It should also be noted that the KT-model assumes random orientation of the inclusions, in effect the medium will be isotropic.

### The Differential Effective Medium Model (DEM)

Berge et al. [1992] introduced a model to account for pore interactions in the KT model, building on the principle of porosity growth suggested by Cheng [1978]. The basic concept behind this is to model a composite medium by incrementally adding dilute concentrations of pores to the background medium. The modeling procedure can be described like this [Johansen and Gelius, 2008]:

- Introduce a dilute concentration of pores to the background medium. Use KT-model to calculate effective properties.
- Let the calculated effective properties represent the background medium, introduce a new dilute concentration of pores. Use KT-model to calculate new effective properties.
- Repeat until set porosity is reached.

The effective properties  $K_{DEM}^*$  and  $\mu_{DEM}^*$  are found by adding a dilute porosity  $\phi_n$  in  $L$  steps by:

$$\frac{(K_{n-1} - K_n)(K_{n-1} + \frac{4}{2}\mu_{n-1})}{K_n + \frac{4}{3}\mu_{n-1}} = \phi_n \sum_{i=1}^N c_i (K_{n-1} - K_i) P^{(n-1)i}, \quad (2.6)$$

$$\frac{(\mu_{n-1} - \mu_n)(\mu_{n-1} + \zeta_{n-1})}{\mu_n + \zeta_{n-1}} = \phi_n \sum_{i=1}^N c_i (\mu_{n-1} - \mu_i) Q^{(n-1)i}, \quad (2.7)$$

where  $\phi_n = \frac{\phi}{L - (n-1)\phi}$ ,  $K_1 = K_m$  and  $\mu_1 = \mu_m$ . The effective properties will be  $K_{DEM}^* = K_L$  and  $\mu_{DEM}^* = \mu_L$ . The number of steps is found by increasing  $L$  until  $K_{DEM}^*$  and  $\mu_{DEM}^*$  converges.

Like the KT-model, DEM assumes random orientation of inclusions, and therefore isotropic media.

### 2.1.2 The effects of porefluids

When the fluid composition in a porous rock changes, the rock's elastic properties will change with it. Gassmann [1951] formulated the relation between the saturating fluids and a rock's elastic properties. His formulation are still the most used method of fluid substitution in isotropic medium. The Gassmann equation can be written:

$$\frac{K}{K_s - K} = \frac{K_{fr}}{K_s - K_{fr}} + \frac{K_f}{\phi(K_s - K_f)}, \quad (2.8)$$

where  $K$ ,  $K_{dry}$ ,  $K_s$ , and  $K_f$ , are the bulk modulus of the saturated rock, dry frame, mineral matrix, and pore fluid, respectively, and  $\phi$  is the porosity. Some important assumptions of the Gassmann theory are:

- Homogeneous and isotropic rock
- Completely connected pores
- All grains have the same properties
- Homogeneous pore fluid saturation
- Wavelength is much larger than the pores and grains

If a highly compressible fluid like  $\text{CO}_2$  is introduced to a brine saturated rock, the overall compressibility of the rock will decrease, and the P-velocity will drop. The bulk density of the rock will also decrease, acting upon the velocity in the opposite direction. However, the changes in compressibility tend to dominate the velocity change. There are exceptions to this though; when gaseous  $\text{CO}_2$  replaces brine, the P-velocity decreases dramatically for very small fractions  $\text{CO}_2$  saturations, but as the  $\text{CO}_2$  continues to replace brine, the effect on the compressibility decreases. This can actually cause the P-velocity to increase for high  $\text{CO}_2$  saturations, since the bulk density of the rock continues to decrease linearly.

According to the Gassmann relation, the shear moduli is not affected by the pore fluid, and thus the only change in S-velocity as an effect of fluid change, is due to changes in bulk density. This means that the S-velocity increases slightly as  $\text{CO}_2$  replaces brine. This effect is small for supercritical  $\text{CO}_2$ , due to the low density contrast between supercritical  $\text{CO}_2$  and brine. Gaseous  $\text{CO}_2$  however, has a larger density contrast to brine, and thus the S-velocity increase will be more noticeable. For low porosity sandstones, the change in S-velocity due to fluid changes, is in any case small, since bulk density will be less influenced by density changes of the fluid.

The properties of fluids and gases can vary significantly with varying temperatures and pressures. Brine is relatively insensitive to pressures and temperatures,  $\text{CO}_2$  however, are highly sensitive to them. Within a relatively narrow range,  $\text{CO}_2$  can be in the gaseous, fluid or supercritical phase, with strongly varying compressibility and density.

### 2.1.3 The effects of pressure

Pressure influence a rock's mechanical properties such as porosity, crack density and grain contacts [Dvorkin et al., 1996]. In general, an increase in pore pressure will decrease the seismic velocity of a rock; as the pore pressure increases, closed low aspect ratio pores will begin to open, and the average aspect ratio of the rock will decrease. As mentioned, a rock with a large fraction of low aspect ratio pores, will be more compressible than one with mostly spherical pores, thus will the velocities decrease. Several authors have also shown that S-velocities are more susceptible to pressure changes than P-velocities [Christensen and Wang, 1985; Xu et al., 2006; Hoffman et al., 2005].

To which extent a rock is sensitive to pressure changes, relies on many factors. Low porosity, highly consolidated sandstones will be less sensitive than high porosity weak sandstones. However, micro cracks and low aspect ratio pores will increase pressure sensitivity, and can cause even low porosity sandstones to become highly pressure sensitive [Xu et al., 2006].

Rocks in the subsurface are subjected to two pressures, the outer confining pressure,  $P_c$ , and the inner pore pressure,  $P_p$ . This section will describe some concepts that will enable modeling of a rock's properties as function of pressure.

#### Effective pressure

If the confining pressure is equal to the lithostatic pressure, it is only dependent on the weight of the overburden and can be expressed as:

$$P_c(z) = g \int_0^z \rho(z) dz, \quad (2.9)$$

where  $P_0$  is the pressure at the surface,  $\rho(z)$  is the effective rock density at depth  $z$ , and  $g$  is the gravitational acceleration.

The pore pressure is often assumed to be hydrostatic, in which case the pressure will be equal to the pressure exerted by a column of water with height equal to burial depth. The hydrostatic pressure can be calculated using equation 2.9 with  $\rho(z)$  equal to the density of the porefluid.

How pressure affects seismic velocities have been thoroughly discussed in the literature, yet the effects are not completely understood. There is however, a general agreement that the effective pressure governs seismic velocities [Hoffman et al., 2005; Todd and Simmons, 1972; Christensen and Wang, 1985; Xu et al., 2006]. The effective pressure of a rock was defined by Biot and Willis [1957] to be:

$$P_e = P_c - nP_p, \quad (2.10)$$

where  $n$  is a coefficient describing internal deformation, called the effective pressure coefficient.  $n$  is introduced to account for cases where changes in confining pressure are not completely cancelled by an equal change in pore pressure, or vice versa. For rocks with high porosity, this constant is close to unity. However, low porosity rocks are more sensitive to changes in confining pressure than pore pressure, thus  $n < 1$ . Biot and Willis defined  $n$  as:

$$n = 1 - \frac{K_{dry}}{K_m}, \quad (2.11)$$

this definition of  $n$  is called the Biot-Willis coefficient. Many other definitions for  $n$  exist. Nur et al. [1995] proposed an upper bound based on critical porosity:

$$n = \frac{\phi}{\phi_{critical}}. \quad (2.12)$$

Todd and Simmons [1972] derived an equation that allowed  $n$  to be determined from empirical measurements:

$$n = 1 - \frac{\left(\frac{\partial V_p}{\partial P_p}\right) \Delta P}{\left(\frac{\partial V_p}{\partial (\Delta P)}\right)_{P_p}} \quad (2.13)$$

which describes the ratio of change in P-wave velocity  $\partial V_p$  as an effect of change in pore pressure  $\partial P_p$  at the constant differential pressure  $\Delta P = P_c - P_p$ , over the change at constant pore pressure  $P_d$ .

Equation 2.13 can be used to compute the effective pressure coefficient if relevant experimental data on the rock in question, exist. If no such data are available, the Biot-Willis coefficient can be used as a first order approximation [Xu et al., 2006].

### Effects of pressure on porosity and pore geometry

One method to model the effects of pressure on seismic parameters, is to calculate changes in porosity and pore geometry, and calculate new seismic properties with the changes included. This method assumes that the change in porosity and pore geometry are the most influential properties in terms of pressure dependency. Many other methods for modeling of pressure dependency exist, a compilation of some of these can be found in Dræge [2001].

When the effective pressure increases, pores will close, and at a certain pressure all pores of aspect ratio  $\alpha_c$  will be closed [Zimmerman, 1991]:

$$\alpha_c = 2P_e \frac{1 - \nu_m}{\pi \mu_m}, \quad (2.14)$$

where  $\nu_m$  is the Poisson's ratio of the rock's mineral. Spherical pores does not change shape, but the volume decreases when effective pressure increases, thus will the average aspect ratio of a rock increase with increasing effective pressure [Dræge, 2001].

Consider a rock with an initial aspect ratio spectrum with  $N$  different pores at an initial pressure  $P_e$ :

$$c[\alpha(P_e)] = \{c[\alpha_1(P_e)], c[\alpha_2(P_e)], \dots, c[\alpha_N(P_e)]\}. \quad (2.15)$$

For a small change in pressure  $\Delta P_e$ , the properties of the rock frame can be assumed invariant, the corresponding change in aspect ratio  $\alpha_i$  can then be described as [Dræge, 2001]:

$$\alpha_i(P_e + \Delta P_e) = \alpha_i + \Delta \alpha_i, \quad (2.16)$$

Johansen [1990] showed that  $\Delta \alpha_i$ , can be written:

$$\Delta \alpha_i = H(P_e) \Delta P_d. \quad (2.17)$$

$H(P_e)$  can for dry penny shaped cracks be expressed as:

$$H(\Delta P_e) = -\frac{4}{3} \frac{1 - \nu^2(P_e)}{K(P_e)(1 - 2\nu(P_e))}. \quad (2.18)$$

Toksöz et al. [1976] showed that the fractional change in aspect ratio is equal to the fractional change in porespace, so that the change in concentration of pores with aspect ratio  $\alpha_i$  can be expressed:

$$\Delta c[\alpha_i(P_e)] = \frac{\Delta \alpha_i(P_e) c[\alpha_i(P_e)]}{\alpha_i(P_e)}. \quad (2.19)$$

And finally, the change in porosity  $\Delta \phi$ , can be expressed as [Johansen, 1990]:

$$\Delta \phi = \sum_{i=1}^N \phi(P_e) \Delta c[\alpha_i(P_e)], \quad (2.20)$$

where  $\phi(P_e)$  is the porosity at the initial effective pressure,  $P_e$ .

By using the above relations, it is now possible to model the elastic parameters' pressure dependency. The new aspect ratio spectrum and porosity can be implemented in an effective medium model, like one of those described in 2.1.

## 2.2 The SIMPLi Seismic modeling algorithm

This section will describe the specific modeling method chosen for this thesis, a short description of other modeling methods can be found in Mikkelsen [2008].

Methods for modeling of synthetic seismic are many, and vary in complexity and precision, the simplest of all being the 1D convolution. If other methods than the 1D convolution are chosen, it is in general necessary to first create synthetic seismic and then process this seismic, to enable interpretation.

Simulated Prestack Local Imaging (SIMPLI) is a proprietary method to create prestack seismic images. The method is implemented in the Norsar software, SeisRox. SimPLI is a convolution technique that as an oppose to simple 1D convolution, allows effects of survey geometry, illumination and resolution, to be predicted [Lecomte et al., 2003].

The necessary input to this method is a background model, and a reservoir model. The background model is a smooth velocity field, while the reservoir model is a more detailed, rather local area. The reservoir model is defined as horizons with seismic parameters defined below and above each horizon. The SIMPLI-method makes use of a property called illumination vector,

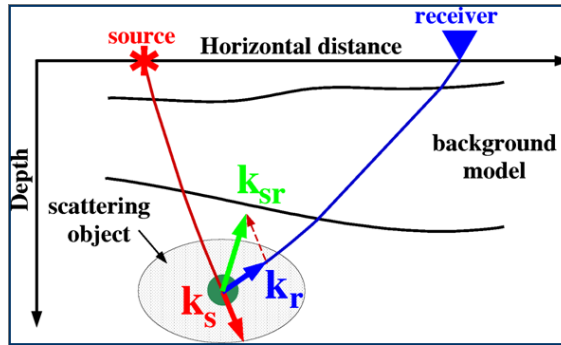


Figure 2.4: Illustration of the illumination vector  $\mathbf{k}_s$  as the difference between two slowness vectors  $\mathbf{k}_s$ , and  $\mathbf{k}_r$ . [from Lecomte et al., 2003]

defined as the difference between source and receiver slowness vectors,  $\mathbf{k}_s$  and  $\mathbf{k}_r$ , at a reference point  $r_o$ :

$$\mathbf{k}_{sr}(r_o, \omega, r_s, r_r) = \mathbf{k}_r(r_o, \omega, r_s, r_r) - \mathbf{k}_s(r_o, \omega, r_s, r_r), \quad (2.21)$$

where  $\omega$  is the angular frequency, and  $r$  is the source and receiver positions. This is illustrated by Figure 2.4. The slowness vectors for a shot-receiver pair are obtained from ray-tracing in the background velocity model, down to the depth of a scattering object at  $r_o$ .  $\mathbf{k}_{sr}$  is a function of local velocity, frequency and incident angle, and give information about illumination of the scattering object. The information from all shot-receiver pairs are combined with a source pulse into a filter, called a K-filter. This filter now represents the total illumination and resolution for  $r_o$ , and describes the total effect of the wave propagation down to this point. If any reflector is oriented perpendicular to an illumination vector, in the vicinity of  $r_o$  this reflector will be imaged with the current survey geometry. A Fourier transform from the wavenumber domain to the space domain, gives a spatial resolution function, or point spread function.

A reflectivity grid is calculated from the reservoir model, this grid is Fourier transformed and convolved with the point spread function. The result is inverse Fourier transformed, yielding a



simulated prestack depth migrated image. This process is equivalent to a spatial 2D convolution [Lecomte et al., 2003].

## 2.3 Time-lapse seismic attributes and metrics

Time-lapse seismic, 4D seismic and repeated seismic, are equivalent terms for the method of using seismic to monitor changes in the sub surface. A time-lapse survey is performed by shooting the same line(s) of seismic at two different times in order to detect changes in the underground caused by production or injection. Simply put, if acquisitional parameters are kept identical between surveys, the only cause for changes in the seismic signal must be due to changes in the earth.

In this section, some common time-lapse interpretation tools are described, along with metrics used to assess the feasibility of time-lapse monitoring.

### 2.3.1 Time-lapse attributes

The three most used measures of change in a time-lapse study are amplitude changes, time shifts, and changes in AVO signature. These methods are used both separately and in combination to interpret time-lapse signals.

#### Amplitude changes

Seismic amplitudes are affected by many factors such as fluid changes, pressure changes, and production or injection related changes in the reservoir and overburden. Due to the many potential causes of amplitude change, it can not uniquely tell which effect has produced differences in timelapse signals [Vernik and Hamman, 2009]. Regardless, analysis of amplitude changes are the most common analysis and interpretation method in time-lapse seismic [Ghaderi and Landrø, 2009].

Changes in pore fluids have successfully been tracked in many oil producing reservoirs, and have had a significant economical impact in the oil industry [Koster et al., 2000]. Amplitude changes have also been used to map CO<sub>2</sub> migration at the Weyburn Field [Li, 2003], and the Sleipner project [Eiken et al., 2000; Arts et al., 2004].

#### Time shifts

When velocities in the subsurface change, the observed seismic travel times will change with it. The amount of change in travelttime for a seismic event between two surveys, is called the time shift. In the case of CO<sub>2</sub> injection, where velocities will decrease both because of saturation and pressure changes, the travelttime will increase. This can often be observed as so called push downs in the seismic. Time shifts will in general be dependent on two factors; the change in velocity, and the thickness of the area with velocity change [Ghaderi and Landrø, 2009].

Time shifts can be determined both by manually comparing the arrival time for a certain event, or by using a cross correlation window between two surveys [Ghaderi and Landrø, 2009]. The most useful information from time shifts, is obtained in areas with high velocity changes, or in areas with thick zones of velocity changes. In thin reservoirs, the timeshifts might be too small to be reliably detected [Coeslan, 2007].

Time shifts are offset dependent, and if the lateral extent of the area in question is smaller than the largest offset in the survey, this effect will be substantial. In the case of a CO<sub>2</sub> plume, long offset traces might undershoot the plume completely, thus experiencing no time shift. The amount of timeshift will then increase with decreasing offset, this can be illustrated by the drawing in Figure 2.5. The drawing illustrates a CMP gather, the grey area represents a CO<sub>2</sub> plume, and the colored line represents rays of seismic waves. The long offset rays will either undershoot the plume completely, resulting in no time shift, or only travel through a small part of the plume, resulting in small time shifts. Small offset rays will travel through a bigger part of the plume, thus experiencing longer time shifts. The problem of offset dependent timeshifts can be solved with

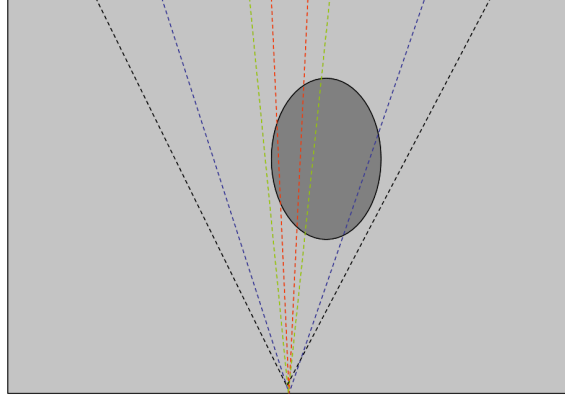


Figure 2.5: Illustration of offset dependent time shifts. The dark grey area represent an area with velocity change. The red ray will travel longer through the area of changed velocity, thus will it experience more time shift.

accurate velocity analysis of the time-lapse data [Ghaderi and Landrø, 2009], but in this study time shifts have only been explored for small offsets.

### AVO-analysis

Since S-velocities are relatively insensitive to saturation changes, but sensitive to pressure increase, it can act as a pressure/fluid indicator [Landrø, 2001]. If an area display large changes in  $V_P$ , but little change in  $V_S$ , it is likely that  $\text{CO}_2$  has migrated to this area without a large increase in pore pressure. Opposite, if both  $V_p$  and  $V_S$  have decreased, it is likely that the  $\text{CO}_2$  is accompanied with a pressure build-up.

If only P-wave data is available, AVO is the only way to get information of changes in S-velocity. Reflection coefficients are angle dependent due to mode conversions at an interface at non-normal incidence. The mode conversions are among other factors, dependent on the S-velocity contrast at the interface, thus will the angle dependent reflection coefficient provide information about  $V_S$ .

The basis of angle dependent reflection coefficients are the work by Zoeppritz [1919], but his equations are much to complex for most practical cases, and so simplifications are most often used. A widely used approximation is the Aki and Richards approximation for P- to P-wave reflections:

$$R_{PP}(\theta) = \frac{1}{2} \left( \frac{\Delta V_P}{V_P} + \frac{\Delta \rho}{\rho} \right) + \left[ \frac{1}{2} \frac{\Delta V_P}{V_P} - 2 \frac{V_S^2}{V_P^2} \left( \frac{\Delta \rho}{\rho} + 2 \frac{\Delta V_S}{V_S} \right) \right] \sin^2 \theta + \frac{1}{2} \frac{\Delta V_P}{V_P} [\tan^2 \theta - \sin^2 \theta] \quad (2.22)$$

where  $\Delta M = M_2 - M_1$  and  $N = (N_2 + N_1)/2$ ,  $M$  and  $N$  denotes either one of  $\rho$ ,  $V_p$ , or  $V_s$ . This equation is often written on the form:

$$R_{PP}(\theta) = R_{P0} + B \sin^2 \theta + C [\tan^2 \theta - \sin^2 \theta] \quad (2.23)$$

where  $R_{P0}$  is the normal incidence angle, often called intercept,  $B$  is called the gradient and describes the slope of the AVO curve at intermediate offsets, while  $C$  is the slope at far offsets, close to the critical angle.

As can be seen from Equation 2.22, the gradient is dependent on contrast in  $V_S$ , and  $V_P/V_S$ -ratio. Landrø [2001] used this to show that the gradient can in some cases be used to distinguish between pressure and saturation time-lapse effects.

The intercept and gradient can be hard to obtain from real seismic, but can be approximated by near and far stacks [Landrø, 2001].

### 2.3.2 Repeatability and detectability

#### Repeatability

One method to visualize the changes in a reservoir is to calculate the difference section between two surveys. Ideally this would only show the actual changes in the underground, but of course no seismic survey can be repeated perfectly, giving rise to noise. The level of this noise relative to the signal strength, is a critical parameter to the success of a time-lapse survey, and is called the repeatability. The repeatability is the ability to replicate seismic data at different times.

To achieve good repeatability, properties such as survey geometry, source signature, receiver coupling, and surface conditions, must be replicated to a high degree of accuracy. Even small changes in position of shots and receivers can cause the repeatability to drop dramatically [Landrø, 1999]. Other important factors such as random environmental noise, are more difficult to controll.

In marine seismic one of the key challenges with regards to repeatability is the positioning. In land seismic, accurate positioning can be achieved using GPS, and therefore does not influence the repeatability to such an extent. The thickness of the weathering layer, difference in source signature and coupling are considered to be more influential in land seismic. Urosevic et al. [2007] found that the state of the weathering layer is by far the most influential property. By shooting the same survey at wet and dry surface conditions, with two different sources, they found that the weathering layer effects are far larger than effects of the source signature.

Several approaches exist to quantify the repeatability, Kragh and Christie [2002] discuss two of these measures, one of which is the normalized RMS, defined as; RMS amplitude of the difference between surveys, normalized by the average RMS amplitude of the two surveys, calculated away from the production/injection zones:

$$NRMS = \frac{200xRMS(a_t - b_t)}{RMS(a_t) + RMS(b_t)}, \quad (2.24)$$

where  $a_t$  and  $b_t$  are two traces within the timewindow  $t_1 - t_2$ , and the RMS operator is defined as:

$$RMS(x_t) = \sqrt{\frac{\sum_{t_1}^{t_2} x_t^2}{N}}, \quad (2.25)$$

where  $N$  is the number of samples in the timewindow, and  $x_t$  is the actual samples. NRMS range from 0% for identical traces, to 200% for traces that anti correlate to each other.

#### Detectability

In order to detect leakage, seismic must be able to resolve small accumulations of  $CO_2$ . The smallest amount of  $CO_2$  that can be detected will be refered to as the detection threshold. The time-lapse signal of a leakage must be large enough not to be masked by noise in a difference section, and is thus dependent on the repeatability of the seismic data. Further, the lateral extent of the leakage must be large enough to be detected. Lateral resolution is governed by the first Fresnel zone:

$$R \approx \sqrt{\frac{Z\lambda}{2}}, \quad (2.26)$$

where  $R$  is the radius of the Fresnel zone,  $Z$  is the depth of the interface, and  $\lambda$  is the wavelength. This means that the detection threshold also is dependent on frequency content, velocities, and depth. The depth dependence is especially important, as the elastic properties of  $CO_2$  will vary strongly with depth. As the  $CO_2$  migrates upwards, it will reach a critical point where it goes from the supercritical to the gaseous phase. Above this point, the accumulation will expand significantly in volume, and become much more compressible, thus making it easier to detect.

Note that the First Fresnell Zone is the lower *resolving* limit. This means that reflecting objects smaller than this can be detected, but the reflection will be subjected to tuning effects, and the extent of the object can not be determined [Sheriff and Geldart, 1995].

At the Sleipner Field, the detection threshold is expected to be about 2000 tonnes of CO<sub>2</sub> at reservoir depth, and less than 600 tonnes 500 m higher in the overburden [Chadwick et al., 2006b]. Hoversten et al. [2006] modeled seismic responses to accumulations of 1000 tonnes of CO<sub>2</sub> at different depths. They found that high signal to noise ratios were necessary to identify the accumulations at depths of more than 1000 m, but that accumulations as small as 100 tonnes, were detectable at 500 m. The detection threshold is of course site specific, and so these results can not be directly applied to other cases, but they serve as good indications that seismic is capable to detect leakages of CO<sub>2</sub>.

## Chapter 3

# A rock physical model of the reservoir sandstone

This chapter will describe the methods chosen to model the sandstone. First the sources of data are described, then the modeling of the dry rock is described in Chapter 3.2, before the effects of saturation and pressure changes are implemented in Chapter 3.3.

### 3.1 Data sources

The amount of data available on sandstones in De Geerdalen Formation, is somewhat scarce, and no data from the actual reservoir is available. A series of test wells have been targeted on identifying the reservoir, however, drilling problems have forced them to stop before reaching reservoir depth. A typical data acquisition for building rock physical models used in seismic monitoring, is as follows:

- Perform electrical well logging to acquire data on velocities, densities and lithology.
- Perform VSP seismic to calibrate surface seismic and well logs.
- Study thin-sections from drill cores to get information about mineralogy, and pore geometry.
- Perform laboratory measurements on drill cores to get information on pressure sensitivity of the reservoir.

As this list shows, most data necessary to model a reservoir, comes from drill cores and well logs. Since these are not available for the injection site, other sources of data was utilized.

Three drill holes have been drilled in the Longyearbyen CO<sub>2</sub> Lab project, Dh1, Dh2, and Dh3, reaching 518, 860 and 403 meters respectively. Drill cores from all three holes are available, the lithological log from these can be found in Appendix A, and the electrical logs from Dh1 and Dh2 can be found in Appendix B. The electrical logs was mainly used to obtain temperature gradients. This is important, as the reservoir temperature will significantly influence the properties of the injected CO<sub>2</sub>.

A study of the drill cores in the Dh-wells aimed to identify cracks, was performed during spring 2009. This study shows that sandstones immediately above reservoir depth, have crack densities above the background level of the well, indicating that the reservoir sandstone might be fractured.

An old exploration well, 7816/12-1, drilled by Hydro in 1991 in Reindalspasset, goes through the De Geerdalen Formation. By permission from StatoilHydro, data from the electrical log of this well was used. The permission granted was for data in the depth interval of the De Geerdalen Formation. At this location, the De Geerdalen Formation is found at 617-684m TVD [Eide et al., 1991]. This is about 200m thinner than the expected thickness in the Adventdalen area. The reason for the difference in thickness is not known, but could be due to tectonics. Regardless,

this difference, in combination with structural differences, yields this location unsuited for a direct comparison on a macroscopic scale. However, electrical log data, provide useful information about the sandstones within the formation. The P-wave velocities and densities used as a basis for modeling, was extracted from this log.

A study of particular interest, was performed by Knarud [1980], where the diagenetic processes in the sandstones of De Geerdalen Formation are interpreted. Information about mineralogy and pore geometry was extracted from this study.

Due to the limitations in the data, some basic assumptions was made:

- The properties of the reservoir sandstone are constant throughout the reservoir.
- The P-wave velocity and density from the Reindalspasset log is representative for the reservoir sandstone.
- The mineral composition from Knarud [1980] is representative for the reservoir sandstone.

These assumptions form the basis of the modeling as all other properties are derived from this data.

## 3.2 The dry rock

The dry rock was modeled in two steps. The mineral matrix was modeled by the KT-model. This was then defined as the background medium for a DEM-model.

### 3.2.1 The mineral matrix

Rocks are formed when sediments are compacted due to gravity and overlying sedimentation. Compaction is governed by the overburden stress, and can lead to ductile deformation and crushing of mineral grains. This deformation and crushing will reduce the porosity of the rock. Mineralogical immature rocks, like those in the De Geerdalen Formation, will be highly subjectable to these effects. The term mineralogical immature means that grains are poorly rounded and sorted, and often occur when sedimentation has been rapid [Knarud, 1980].

All rocks are subject to diagenesis, which is a chemical, physical or biological reaction where minerals attempt to establish equilibrium in the rock. Chemical diagenesis will in general reduce the porosity of the rock through chemical compaction and cementation [Dræge, 2006]. In addition to the porosity reduction, diagenesis affects the elastic properties of rocks by introducing new minerals with new elastic properties.

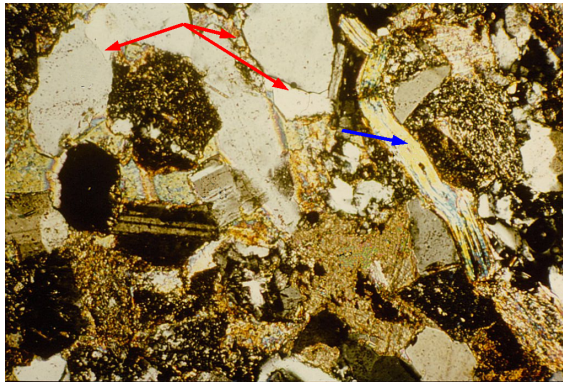


Figure 3.1: Thin-section of a sandstone in the De Geerdalen Formation [modified from Knarud, 1980]. The red arrows show low aspect ratio pores/cracks between Quartz grains, while the blue arrow shows an oblong shaped Muscovite mineral. The scale of this image is 1mm x 1mm

The composition of minerals used in modeling of the mineral matrix, is based on mean values from 45 samples in Knarud [1980]. The mechanical compaction of grains result in oblong shaped primary grains as can be seen in Figure 3.1. The cement also has irregular and oblong shapes. To account for this, minerals are given aspects ratios  $\alpha_m < 1$ . The values for fractional volume, elastic moduli, density, and assigned aspect ratio for each of the minerals are given in Table 3.1.

Table 3.1: Mineral composition of modelled sandstone. Elastic moduli and densities are taken from Mavko et al. [1998], volume fractions are based on mean values from 45 samples in Knarud [1980], and aspect ratios are interpreted from images of thin sections in the same study.

Mineral	Volume fraction	Bulk modulus	Shear modulus	Density	Aspect ratio
-	[%]	[GPa]	[GPa]	[g/cc]	-
Quartz	53	37	44	2.65	1
Clay minerals	16	25	9	2.6	0.1
Dolomite	16	69.4	51.6	2.88	0.9
Feldspar(Albite)	10	75.6	25.6	2.63	0.5
Muscovite	5	61.5	41.1	2.79	0.1

The effective mineral matrix was modelled using KT-theory, as described in Chapter 2.1.1. Quartz is defined as the background medium, while the other minerals are added as inclusions. The resulting elastic properties can be seen in Table 3.2.

Table 3.2: Calculated elastic moduli and density of mineral matrix. Calculations are done using the KT-model based on the properties listed in Table 3.1

$K_m$	$\mu_m$	$\rho_m$
[GPa]	[GPa]	[g/cc]
40.45	34.15	2.792

### 3.2.2 Adding pore space

Knarud [1980] analyzed samples of the De Geerdalen sandstones at a wide range of localities where the formation outcrops. His study shows that the porosity is generally low and close to zero in some samples. Primary porosity have been reduced both from mechanical compaction and from cementation. Microscope analysis of thin-sections showed many samples with virtually no porosity, but injection tests of the same samples showed generally higher porosities. The difference in observed porosity was quite significant, injection tests showed porosities of up to 6.7% in samples where thin-sections showed values below 1%. The fact that much of the porespace can not be observed visually, can be an indication that a significant part of the pores have very low aspect ratio. Evidence of low aspect ratio pores can also be seen in the thin-section in Figure 3.1.

The process of calculating the different model properties can be summarized as follows:

1. Calculate effective mineral matrix properties as described in Chapter 3.2.1:  $K_m$ ,  $\mu_m$ , and  $\rho_m$ . Define this as the background medium.
2. Calculate porosity  $\phi$ , from difference in the density  $\rho_m$ , calculated in step 1, and the measured density in the Reindalspasset well.
3. Use inclusion model to invert for pore geometry  $c(\alpha_i)$ , and  $\alpha_i$ , so that modelled velocity  $V_P^*$  is equal to measured velocity in Reindalspasset, at porosity  $\phi$ , calculated in step 2.

The use of the KT-model is limited to low porosity and none interacting pores, and while the sandstone *does* have low porosity, even small concentrations of low aspect ratio pores could lead to violation of the restriction in Equation 2.5. Indeed, the inversion of pore geometry showed

an aspect ratio spectrum that violates the KT-model's assumptions, thus the DEM-model was chosen.

Table 3.3: Properties measured in the Reindalspasset well.

$V_{Pshale}$	$V_{Psandstone}$	$\rho_{shale}$	$\rho_{sandstone}$
[km/s]	[km/s]	[g/cc]	[g/cc]
4.30	4.27	2.66	2.65

The properties measured in the Reindalspasset well are given in Table 3.3. Assuming the properties of the mineral matrix in Table 3.2 holds true for this location, and that pores are completely saturated with brine, the porosity of the sandstone can be calculated as follows:

$$\phi = \frac{\rho_m - \rho_{measured}}{\rho_m - \rho_{brine}} \quad (3.1)$$

This give a porosity of approximately 8%. Step 3 in the process listed above, was performed with the calculated background medium from step 1, the porosity from step 2, and the velocity from Table 3.3. One possible aspect ratio spectrum from this calculation is:

$$\alpha_i = [1, 0.1, 0.01, 0.001], \quad (3.2)$$

and

$$c(\alpha_i) = [1, 0.1, 0.01, 0.001]. \quad (3.3)$$

If it was necessary to model the sandstone at higher porosities, the KT- and DEM-models would become invalid. Other models would have to be applied for these porosity ranges, for example the contact cementation model. Draege et al. [2006] shows a method to use different effective medium theories for varying porosity ranges of the same rock. For this study however, it is sufficient to model the rock at a narrow porosity range.

### 3.3 The effects of CO<sub>2</sub> saturation and pore pressure increase

The elastic properties of CO<sub>2</sub> will vary dramatically with varying temperature and pressure, and it is important to account for this in the modeling process. The expected temperature and pressure at reservoir depth, will cause CO<sub>2</sub> to be in the supercritical phase, exhibiting gaseous-like compressibilities and liquid-like densities. The properties of brine and CO<sub>2</sub> was calculated by an equation of state by Span and Wagner [1996], using the software CO2Therm, developed by Erik Lindeberg at Sintef. The initial pore pressure at reservoir depth is expected to be approximately 100 bar, and the injection pump is capable of operating at approximately 50bar of overpressure. This means that the expected pressure range CO<sub>2</sub> might be subjected to is 100-150bar. The temperature gradients from the different wells in Elvebakk [2008] and Eide et al. [1991] yield an expected temperature range of 30-34°C. The bulk modulus and density of CO<sub>2</sub> and Brine for these intervals can be seen in Figure 3.2.

Figure 3.2c shows how density and bulk modulus of CO<sub>2</sub> are expected to vary with depth. The dramatic change at 500m below the surface, represent the transition from gaseous to supercritical phase. Below this depth, the density is more than four times larger than above, while the change in bulk modulus is two orders of magnitude. This is of course important with respect to monitoring, but also in terms of storage capacity. Below this line, it is possible to store four times the amount of CO<sub>2</sub> in the same rock volume.

The effects of saturation changes was modelled using Gassmann's equation, with the fluid properties for the respective pressures. Gassmann's equation is defined by Equation 2.8. To reduce the number of variables in the fluid substitution, the following assumptions was made:

- The temperature is 30°C in the entire reservoir.



### 3.3. THE EFFECTS OF CO<sub>2</sub> SATURATION AND PORE PRESSURE INCREASE

- The saturation of CO<sub>2</sub> is patchy.

The effects of increasing pore pressure in the sandstone was modelled by changes in porosity and pore geometry, as described in Chapter 2.1.3. This method can be summarized by the following pseudo-code:

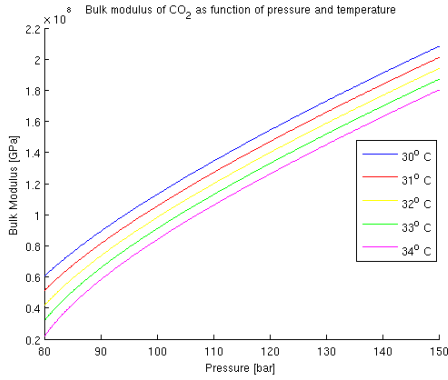
for each pore pressure increase:

```
calculate effective pressure using Biot-Willis coefficient
calculate change in aspect ratio spectrum
calculate resulting change in porosity
```

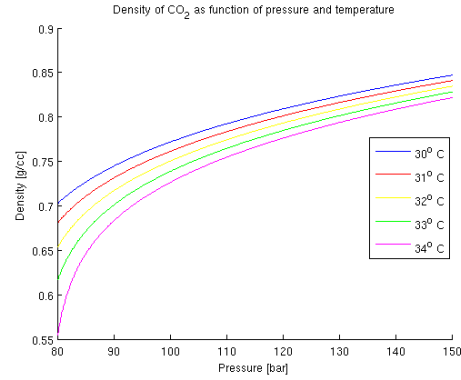
```
if effective pressure < closing pressure for aspect ratio alpha_c
```

```
    add dilute concentration of pores with aspect ratio alpha_c
```

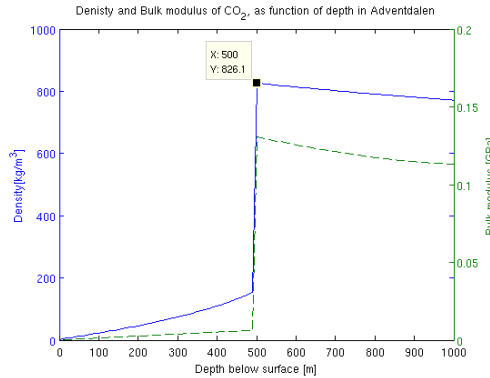
```
end
```



(a) Bulk modulus of CO<sub>2</sub> as a function of pressure for temperatures of 30, 31, 32, 33, and 34°C. In this range, the bulk modulus varies linearly with temperature, while the variation with pressure is slightly nonlinear.



(b) Density of CO<sub>2</sub> as a function of pressure for temperatures of 30, 31, 32, 33, and 34°C. The density varies nonlinearly with both temperature and pressure.



(c) Density and Bulk modulus of CO<sub>2</sub>, as function of depth below surface in Adventdalen. The transition from the supercritical phase happens at around 500m. The calculations are based on a temperature gradient of 30°C/km and hydrostatic pressure.

Figure 3.2: Properties of CO<sub>2</sub> as function of pressure, temperature, and depth.

```
calculate effective elastic properties using DEM
saturate with fluid mixture with fluid properties for current pore pressure.

end
```

To enable modeling of the effect of opening pores, some assumptions was made. It was assumed that the rock contains a set of very low aspect ratio pores that initially are closed. As the pore pressure increases and the critical pressure for each aspect ratio is reached, a dilute concentration of pores with this aspect ratio is added.

## Chapter 4

# A seismic model of the reservoir

A seismic model has two basic components; the geometry and the seismic properties. The geometry describe the depth, thickness and shape of the geological formations. The geological formations form layers that are bounded either by the outer boundaries of the model, or by geological features such as faults and pinch outs. The layers and their bounds form model blocks, and each of these blocks are assigned seismic velocities and densities. This chapter will describe the process of building a 2D seismic model of the subsurface at the injection site.

### 4.1 Data sources

The most important data for the model, is seismic. Three 2D seismic lines were acquired during the course AG-335, at UNIS in spring 2008. The acquisition was done using a 1500m snowstreamer with 60 channels. Detonating cord was used as the source, and the shot interval was 50m. Line 1, crosses the area where the planned injection well will be located, in a NW-SE direction. The location of this line is indicated on the map in Figure 1.3, and the depth migrated section is shown in Figure 4.1. The geometry of the model is based on the interpretation of this seismic line. The interpretation of the overburden was aided by the drill core logs. The log from Dh2 reaches down to 857m, lithological changes in this log was related to reflectors in the seismic section. Below the depth of Dh2, the interpretation was aided by logs from outcrop studies, these can among other places be found in Mørk et al. [1999], and Knarud [1980].

Data about velocities and densities are harder to find. The electrical logs in Elvebakk [2008] give information about velocities down to about 450m. These logs only have a qualitative density log, showing the relative changes, but no actual density values. The qualitative density log does however give some useful information; the relative density of different lithologies, and the absence of a clear depth trend. The sandstones in the overburden have lower densities than mudstones, claystones, and shales.

The data from the Reindalspasset well, gives information about P-velocity and density for sandstones and shales in the De Geerdalen Formation.

### 4.2 Seismic interpretation

The necessary level of detail in the seismic model varies with depth. The seismic modeling only focus on the reservoir and the immediate surroundings, in effect 800m to about 1200m. A low detailed, smooth background model of the overburden is needed to enable modeling of the effects of wave propagation. At reservoir depth, a more detailed geometry is needed. The varying requirements for details, are reflected in the seismic interpretation, where only a few reflectors are interpreted in the overburden, while a more thorough interpretation is performed at reservoir depth.

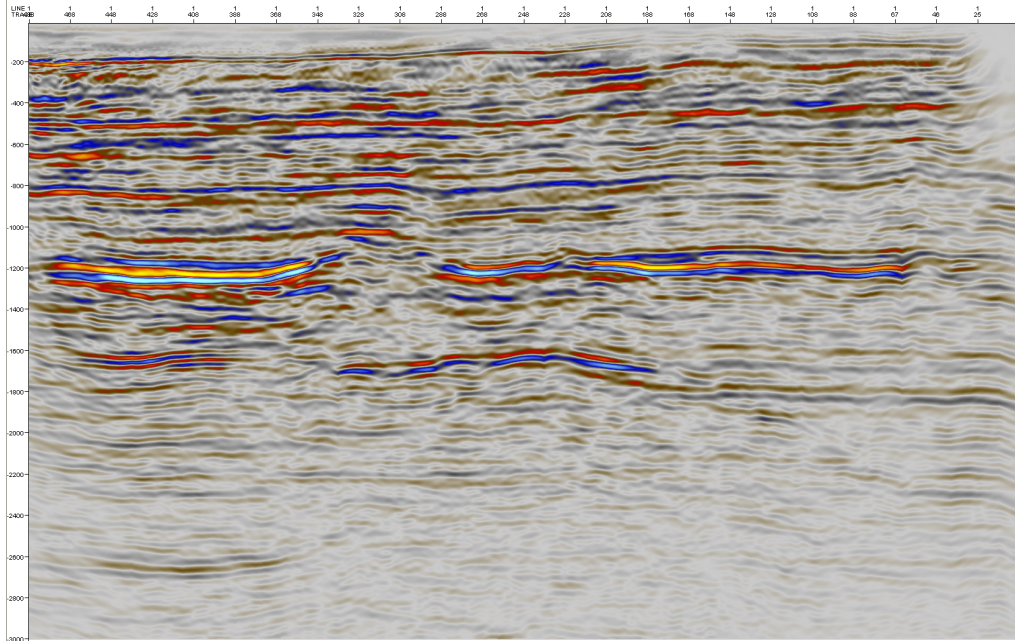


Figure 4.1: Line 1. The depth migrated seismic line that crosses the injection site in Adventdalen.

Very little interpretation of seismic data in Adventdalen is available, surfaces for top Triassic, and top Permian have been interpreted on time migrated sections, but these are incomplete. The depth migrated section in Figure 4.1 was processed by Bernt Ole Ruud at the University of Bergen, and was not available until March 2009.

Interpretation of prominent reflectors down to the depth of Dh2, was relatively straightforward. Drill core logs show major lithological changes at depths that fit well with strong and continuous reflectors in the seismic section. Figure 4.2 illustrates the interpretation of the key seismic horizons in Line 1. The stratigraphic column shows a depth prognosis of the different geological formations. This prognosis is the same as described in Chapter 1.1.1, and is based on the drill core logs. The dotted lines in the column indicate that there are considerable uncertainties in the depth prognosis, as boundaries have not been identified in drill cores, or have not been reached by drilling. In the following, the interpretation will be described in sequence from top to bottom.

The uppermost horizon in Figure 4.2 is interpreted as Top Rurikfjellet Formation. At this horizon the lithology changes from the sandstone dominated Helvetiafjellet Formation, to the shales of Rurikfjellet Formation.

The next reflector is interpreted as the base of the faulted zone in Agardfjellet Formation. This zone contains plastic clays, and has high fracture density [Braathen et al., 2009]. The thickness of the area with increased fracture densities is reported to be up to 180m. The upper reflection from this zone is strong, but chaotic and not continuous, the lower positive reflection however, is both strong and continuous.

The immature sandstones in the De Geerdalen Formation have relatively low velocities. The log from Reindalspasset shows that the velocity is lower than the overlying shales. Based on this, the negative reflector at around 800m, is interpreted as the Isfjorden member of the De Geerdalen Formation. The next strong negative reflection is interpreted as the top of the first prominent sandstone within this formation.

The depth interval of 800-1100m has several chaotic reflectors, where amplitudes appear to be smeared vertically. This is interpreted as tuning effects from thin layers with gradually increasing or decreasing acoustic impedances. The De Geerdalen Formation consists of repeated coarsening upwards successions. However, in many of the outcrop logs, it can be seen that these units combined, make up patterns of increasing and decreasing values of net/gross on a scale of tens

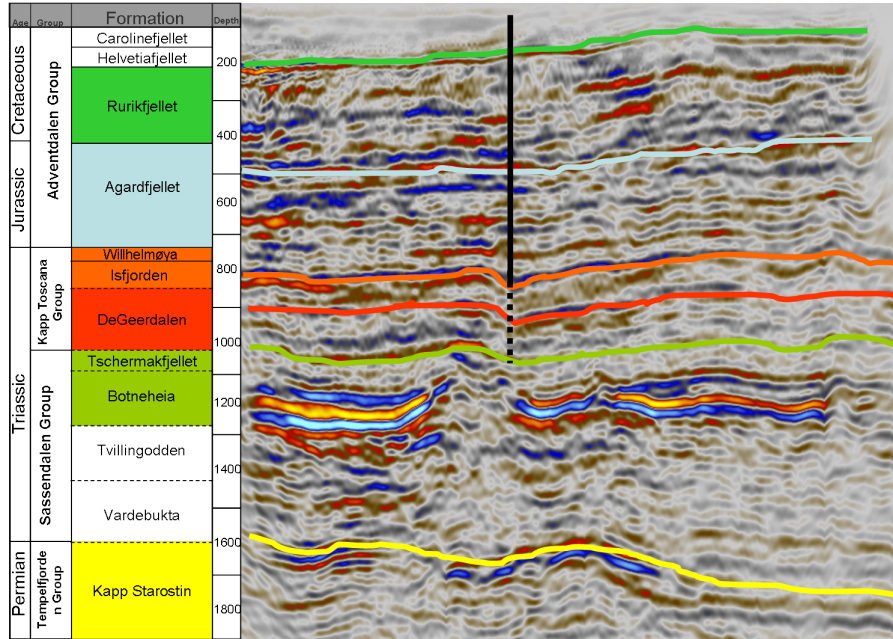


Figure 4.2: A coarse illustration of the key seismic horizons in Line 1. The predicted stratigraphic column, with depths of the different geological formations are given in the left of the figure. Colors of horizons correspond to the formation with the same color in the column. The black line indicates the location of the planned injection well, while the dotted line indicates the reservoir interval

of meters. This observation can explain the gradually increasing and decreasing AI, and thus supports the interpretation of the smeared reflections.

The strong positive reflector at 1100m, is interpreted as Top Botneheia Formation. This is a shale dominated succession, where the upper parts are strongly calcite and dolomite cemented [Dallmann et al., 2001; Mørk et al., 1999]. The high concentration of carbonate cementation, gives it a high velocity, accounting for the strong positive reflection.

Several prominent features are found in the 1100-1300m interval. The anomalous strong reflectors at 1200m have earlier been interpreted as the Permian Kapp Starostin Formation, known to have velocities of over 5  $km/s$  [Eiken, 1985]. However, the depth migrated seismic section reveals that this reflector is too shallow to be the Kapp Starostin Formation, expected at a depth of more than 1500m at this location [Mørk, 2008]. No other known formations contain lithologies that would cause such strong reflections. The only suggestion is that it is caused by a dolerite intrusion. These intrusive volcanic rocks can have velocities of 5-6  $km/s$ , and densities of up to 3  $g/cc$ . Dolerite intrusions are known to exist at several locations in Svalbard, ranging in thickness from a few meters to a few tens of meters [Dallmann et al., 2001]. An example of such an intrusion, or sill as it also is called, can be seen as the diagonal dark rock that breaches the layering, in the picture in Figure 4.3.

Skola et al. [1980] reported a 42m thick dolerite intrusion in the Braivsberget Formation, found in a drill hole at the Russian settlement in Grumantbyen, close to Adventdalen. At Svalbard, these intrusions are known to be laterally continuous for up to for 20 km [Eiken, 1985]. Dallmann et al. [2001] also states that sills with NW-SE trends are common in the Adventdalen area, this is the same orientation as Line 1. Intrusions can also be seen in the area around Diabasodden, close to Adventdalen [Dallman, 1993]. These facts support the interpretation that this is indeed a dolerite intrusion.

The second feature is the anticlinal shape at 1100m-1300m. This feature was hard to interpret. The reflections are chaotic and highly discontinuous, the strong reflections from the sill disappears, and the reflections below are blurred. Many scenarios was suggested to explain this, ranging from



Figure 4.3: Picture showing a dolerite intrusion in Svalbard. The intrusion can be seen as a dark diagonal across the mountain side. [from Andresen, 2007]

gas chimney, to mud volcano, and carbonate buildup. The resemblance to the carbonate buildups described by Elvebakk et al. [2002] is striking, but these buildups are not consistent with the depositional environment of Svalbard's early Triassic [Nakrem, 2002].

A more likely interpretation is the termination of a minor thrust ramp, or a swelling linked to the Tertiary transpressional regime. The Botneheia Formation is a known detachment zone, and can act as a lubricant for thrust faults. Anticlinal swellings with dips of up  $6^\circ$  are also known to exist in this formation [Dallmann et al., 2001].

The lowest horizon at around 1600m, is interpreted to be the Permian Kapp Starostin Formation. This formation contain cherts with known velocities of  $5\text{-}6\text{ km/s}$ , and is a strong regional reflector. The reflection strength at this location seem to have been dimmed by the strong reflection at 1200m.

This interpretation gives a total thickness of the De Geerdalen Formation of about 230m, which is in accordance with observations at outcrops close to Adventdalen [Mørk et al., 1999; Dallmann et al., 2001; Knarud, 1980].

### 4.3 From interpretation to seismic model

The interpretation described above, was done in the Petrel software. In addition to the horizons already described, several weaker and discontinuous reflectors were interpreted. The interpretation exists as a series of horizons, the coordinates for these can be exported as text files. These text files can be imported to the Norsar2D modeling software, where the seismic model is implemented.

The basic geometry of the model is now defined by the horizons imported from Petrel. Even though the details of the reservoir zone can not be inferred from seismic data, and no well data exists, efforts was made to apply all available data to build a model that is representative of how the reservoir zone might look.

The following assumptions was made:

- The first reservoir sandstone is the reflector at around 900m. Base reservoir is the reflector at around 1100.
- The smeared reflections are caused by tuning effects from thin layers with gradually decreasing or increasing acoustic impedance.
- The net/gross value is 0.4. This value is calculated as the average of net/gross values at 14 outcrop locations [Braathen et al., 2009]. The sandstones are collected in four units, with thicknesses of 15m, 5m, 10m, and 20m, listed from top to base.
- The seismic properties of the sandstones are identical.

No internal reflectors are distinguishable in the reservoir zone, therefore the depth and thickness of the sandstone units are based on the stratotype for the De Geerdalen Formation, located at Storfjellet, east of Adventdalen [Mørk et al., 1999]. This shows two prominent sandstones at top



and base, with a series of smaller sandstones in between. For simplicity, four sandstones was defined in the model; 15m and 20m thick at top and base, and two smaller of 5m and 15m in the middle. To enable modeling of laterally varying saturation and pressure states within the individual sandstones, they were divided into nine zones. The zones are numbered one to nine from right to left. The division is clearly seen as vertical lines in the light blue sandstone units in Figure 4.4.

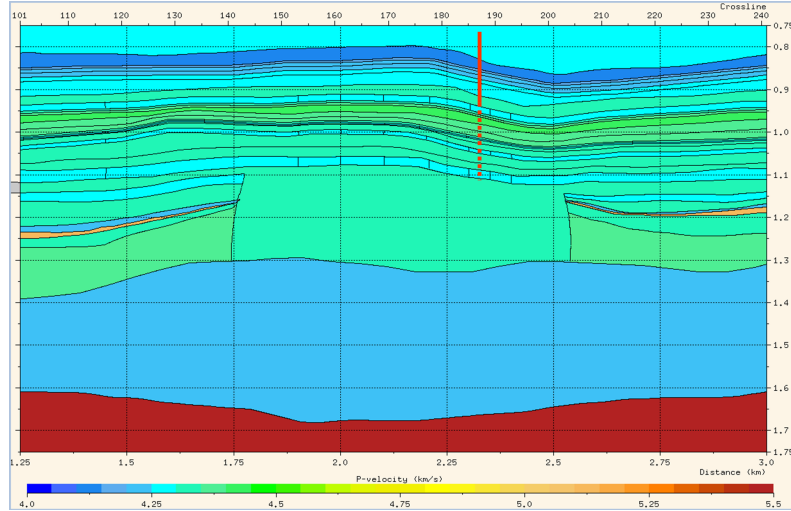


Figure 4.4: The 2D reservoir model. Colors indicate P-velocity. The sandstone units in the reservoir zone can be seen as three layers with vertical separators. The red line indicates the location of the planned injection well.

The smeared reflections, was recreated by creating a series of thin layers with gradually increasing and decreasing acoustic impedance. The first succession of such layers starts from the base of the upper light blue sandstone unit. The blocks for these layers was assigned seismic properties based on the information of shales in the Reindalspasset well.

The strong reflections at 1200m is as mentioned, interpreted as a dolerite intrusion. However, there are several strong negative and positive amplitudes in this area. If the amplitude shapes originates from a single layer, the data cannot have been properly zero-phased. Assuming the latter is not the case, the amplitude pattern must originate from tuning effects between several layers. Intrusions are often found in soft clays, where the force needed to penetrate is the lowest. Such a soft rock will in general have lower velocities than the surroundings, thus the first negative reflection can be interpreted as such a rock. The following strong positive and negative amplitude, can then be interpreted as the intrusion.

The intrusion is implemented as the orange high velocity/density layer, pinching out towards the anticlinal feature. The modeled intrusion is located inside a layer with velocities lower than the surroundings.

The anticlinal structure posed problems during the interpretation, as well as the model building. Since a good interpretation proved difficult, and due to the fact that the feature is located *beneath* reservoir depth, the modeling of this feature was not prioritized. A few attempts were made to reproduce the feature with synthetic seismic, but none was successful. Therefore, this area was simply assigned homogeneous seismic properties.

Finally, The Permian Kapp Starostin Formation, is the red layer in the bottom of Figure 4.4.

## Chapter 5

# Integrating the two models and performing seismic modeling

### 5.1 Integrating the two models

The two models described in Chapter 3, and 4, now exist in two different softwares, the sandstone model is implemented in Matlab, and the seismic model in Norsar2D. The process of integrating them is a matter of assigning the seismic properties for the sandstone, to the respective blocks in the reservoir model. This task is solved by writing the properties  $[V_P(s, p), V_S(s, p), \rho(s, p)]$  at a certain saturation and pressure state  $(s, p)$ , to a rock-properties fileformat which is readable by Norsar2D. This file can now be assigned to the blocks for the nine reservoir zones in the model, and can be updated for new saturation-pressure states.

The integrated model is now implemented in 2D. However, the seismic modeling software requires a 3D model. This problem is solved by creating a 2.5D model. This can be done by replicating the 2D model in Figure 4.4 y-direction. This will give a 3D model that varies in the x- and z-directions, but not in the y-direction. This operation can be done in the Norsar3D software. The model from Norsar2D is imported to Norsar3D as blocks with geometry and seismic properties. A 2.5D model is generated, and exported ready for seismic modeling. The resulting 2.5D model is shown in Figure 5.1. Note that the figure is scaled in the z-direction for display purposes.

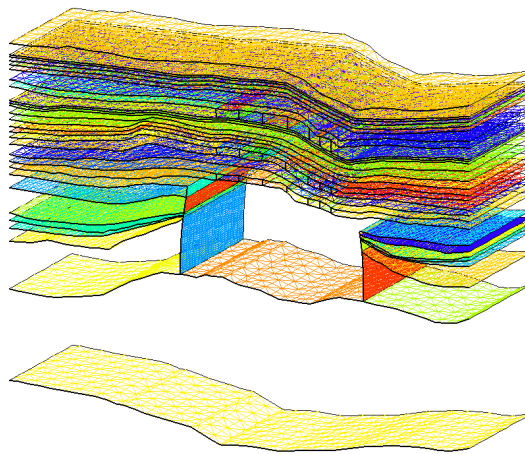


Figure 5.1: The 2.5D reservoir model. The model properties varies in the x-and z-directions, but not in the y-direction. The figure is scaled in the z-direction for display purposes.



## 5.2 Seismic modeling

The SeisRox software was chosen for the seismic modeling because of the SIMPLi method's relatively simple demands for input and processing. One alternative considered was to use conventional ray tracing modeling. This would require the same input, but processing of the synthetic seismic data would be necessary.

The data from SeisRox is in the depth domain, and therefore does not allow for investigation of time shifts. Time has not allowed a complete time shift study as this would involve an additional modeling scheme, as well as a processing scheme for ray tracing modeling. Timeshifts was therefore calculated for normal incidence in Matlab. In addition, two single shot gathers was produced with ray tracing; one for the base case, and one after five years of injection. Timeshifts was manually picked from small offsets in these shot gathers, to verify the calculated values.

SeisRox does not allow noise to be added to the data. To explore how noise can affect the monitoring, Gaussian noise was added to the synthetic seismic data in Matlab. It should be noted that adding noise on a migrated section, is not descriptive of how noise in seismic data occurs, but can act as an illustration of how random noise can affect detectability and monitoring results.

The seismic modeling is the final step in the long process described in the preceding chapters. For clarity, the complete workflow, from gathering of data, to seismic modeling, is illustrated in the flowchart in Figure 5.2.

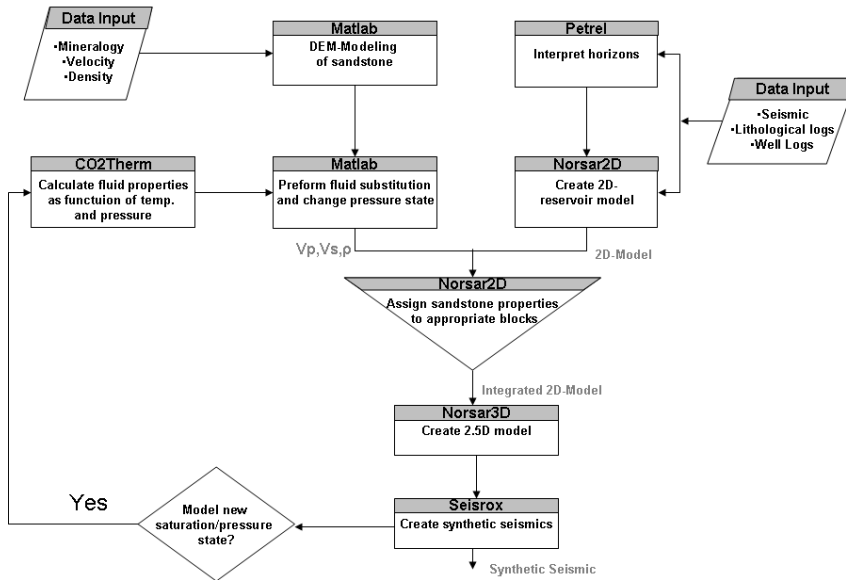


Figure 5.2: Flow chart of the process from gathering of data to generating synthetic seismic data.

The next section will describe the different cases that was modeled to answer the questions raised in Chapter 1.2.

### 5.2.1 Modeling time-lapse signal of CO<sub>2</sub> migrating in the reservoir

The seismic modeling was set up as a case study, where the effects of the injection was monitored at six months, one year, five years, and 10 years after start-up. In order to limit the amount of test cases, some assumptions was made about the saturation and pressure states in the reservoir :

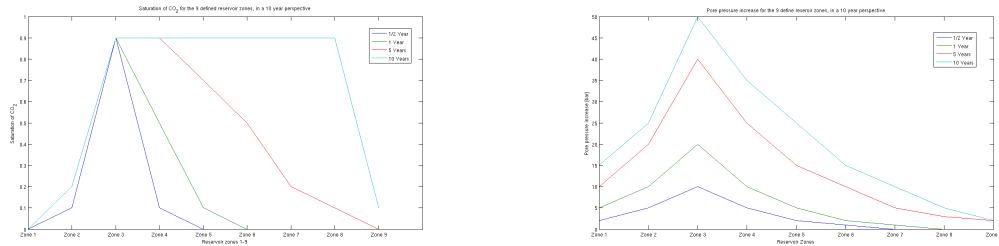
- Patchy saturation of CO<sub>2</sub>.

- Same lateral saturation and pressure distribution in all the sandstone units.
- The sandstone units have individual seals, preventing upwards migration between units. The CO<sub>2</sub> is distributed in the entire thickness of each sandstone.
- Constant injection rate that will lead to a pressure build up over time.

The changes in seismic properties caused by CO<sub>2</sub> fluid substitution by the patchy and homogeneous saturation scheme, can be regarded as lower and upper bounds. The actual saturation pattern will therefore be in between the two. The assumption of patchy saturation will result in a linear velocity change as CO<sub>2</sub> saturation increase, instead of the highly unlinear velocity change caused by homogeneous saturation.

How the CO<sub>2</sub> will migrate in the reservoir is impossible to predict without performing reservoir simulations. This requires reservoir geometries, and permeability and porosity distributions to be established. Some simple guidelines might be applied though. The buoyancy of CO<sub>2</sub> will lead the migration in an up-dip direction. For the cross sectional model in Figure 4.4, this would mean that the migration direction would be to the left and into the plane, corresponding to a NW and N direction respectively. Following this simple scheme, the lateral extent of the plume can be estimated.

With the assumption that the lateral extent is equal in all sandstone units, the injection rate, porosity, and volume of reservoir rock, can be used to estimate the progression of the plume front. If the injection rate is constant, the pore pressure can be expected to build up over time. This build up will be largest close to the well, but will also propagate through the entire reservoir [Rutqvist and Tsang, 2002]. The pressure and saturation distributions, and their development



(a) Saturation distribution for the 9 reservoir zones for the modelled cases. Each line represents the saturation for the given monitor survey. The CO<sub>2</sub> plume migrates from Zone 3 in the up-dip direction, and reaches zone 9 after 10 years.

(b) Pressure distribution for the 9 reservoir zones for the modelled cases. Each line represents the change in pore pressure for the given monitor survey. The pressure gradually increase in the entire reservoir. The pressure increase is largest close to the well in Zone 3, and drops off to both directions.

Figure 5.3: Modeled saturation and pressure distributions in the reservoir over 10 years

over time, can be seen in Figure 5.3a and b. The reservoir zones are numbered from right to left in the sandstone units in Figure 4.4. As the Figure shows, the CO<sub>2</sub> front was modeled to migrate in the up-dip direction of the model. The front of the plume was modeled to have low saturation of CO<sub>2</sub>, while the zones close to the well was almost fully saturated. The fully saturated area, grow in pace with the propagation of the plume front.

The pore pressure was modeled to increase most around the well, and drop off in the lateral directions. The pore pressure increased in the whole of the reservoir as the injection continued, and reached a maximum at 50 bar after 10 years. The shape of the pressure drop-off curve was modeled to be in accordance with the results of Rutqvist and Tsang [2002].

### 5.2.2 Modeling time-lapse signal of CO<sub>2</sub> leaking into the overburden

Leakage from geological storage of CO<sub>2</sub> can occur in several ways, and while it is beyond the scope of this study to assess the risks of leakage, a key success criteria for monitoring is the ability

to detect it. It is therefore useful to describe some potential leakage pathways from the storage formation to the overburden.

The storage formation in the Longyearbyen CO<sub>2</sub> lab does not have any pronounced structural traps, and so the footprint of the injected CO<sub>2</sub> can be expected to be large, meaning that the areal extent of the storage is large. A disadvantage in this type of storage formation, is that the CO<sub>2</sub> is exposed to a large area of the caprock and is thus vulnerable to heterogeneities in the caprock [Chadwick et al., 2006a]. If a fault or other area with slightly higher permeability is present at any location where the CO<sub>2</sub> migrates, leakage might occur. If CO<sub>2</sub> starts to migrate into a fault area, pressure within the area will rise, and a self reinforcing loop of increasing permeabilities and pressures can be initiated. This can lead to the fault being completely penetrated by the CO<sub>2</sub>, and in the case that the fault goes through the entire cap rock, CO<sub>2</sub> might spill into a higher aquifer [Tsang et al., 2008; Rutqvist and Tsang, 2002].

Wells also represent a potential leakage pathway. Defects in casing or cement, deterioration of cement plugs, corrosion damages, and formation damages during drilling, can all create potential leakage pathways [Arts and Winterhaegen, 2005].

These two scenarios can lead to similar leakage patterns, where CO<sub>2</sub> migrates near vertically, and spills out to an aquifer in the overburden. To explore the detectability of such a leakage, the model in Figure 5.4 was created.

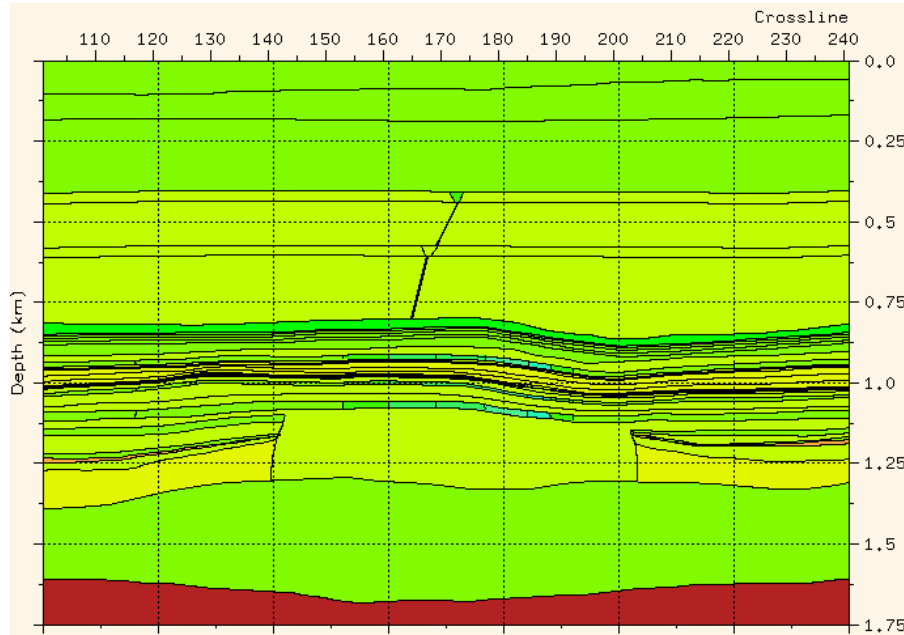


Figure 5.4: 2D model built to explore the effects of leakage in the overburden. The high angled lines represents fault zones, while the wedge shaped blocks represent CO<sub>2</sub> accumulation in aquifers. The aquifers are located at approximately 450m, and 600m, respectively above and below the critical point for CO<sub>2</sub>.

The high angled lines in the overburden of Figure 5.4 represents fault zones. The lower fault zone goes into the primary caprock of shales in the Agardfjellet Formation. The lower triangular shaped block represents an accumulation of CO<sub>2</sub> migrated from the first fault, into a permeable aquifer in the Agardfjellet Formation. The depth of this accumulation is below the critical point of 500m, where CO<sub>2</sub> goes from the supercritical to the gaseous phase. The next CO<sub>2</sub> accumulation is located above this point, in the Rurikfjellet Formation. This model therefore allows the detectability of three different leakage scenarios to be assessed; CO<sub>2</sub> migrating along faults, small accumulations of CO<sub>2</sub> in the deep overburden, and small accumulations of CO<sub>2</sub> in the shallow overburden. This modeling approach was inspired by works of Tsang et al. [2008], Hoversten et al.

[2006] and Rutqvist and Tsang [2002].

The velocity effects of the leakages was calculated using Gassmann's equation. The accumulations of CO<sub>2</sub> in the overburden is assumed to be located in aquifers with porosity of 10%, a value that is representable for many of the aquifers in the overburden [Mørk and Braathen, 2008]. The initial velocities and densities are the same as those assigned for the respective blocks in the initial model. The properties of CO<sub>2</sub> are calculated by CO2Therm, for the pressure and temperature expected at the depth of the respective accumulations.

The geometry of the accumulations are modeled as downwards pointing cones, the volume of accumulated CO<sub>2</sub> in tonnes can then be calculated as:

$$V_{CO_2} = \frac{1}{3}r^2\pi h\phi\rho_{CO_2}S_{CO_2}, \quad (5.1)$$

where;  $r$  is the radius of the cone base in meters,  $h$  is the height of the cone in meters,  $\phi$  is the fractional porosity,  $S_{CO_2}$  is the fractional saturation of CO<sub>2</sub>, and  $\rho$  is the density in  $[kg/m^3]$ .

## Chapter 6

# Modeling results and analysis

This chapter will describe the results obtained by the modeling described in Chapter 3 to Chapter 5. First the results from the rock physical modeling are presented. Next, results from the synthetic seismic modeling are presented in a qualitative manner, before the results from the rock physical modeling are applied to quantify observed changes in the synthetic seismic data. Finally, the results from the leakage modeling are presented.

### 6.1 Results from the rock physical modeling

Since all modeled properties to some extent are dependent on both pore pressure and saturation of CO<sub>2</sub>, the results from the rock physical modeling will be presented as contour plots. This allows data of two variables to be represented as colored contours. Unless otherwise stated, the color scale in the plots represents relative change in percentage.

Data derived from seismic are in general more robust when treated as relative numbers instead of absolute numbers. Throughout the rest of the report, methods and results will be represented as relative numbers, in the following defined as

$$\Delta M = \left| 1 - \frac{M_2}{M_1} \right| \cdot 100\% \quad (6.1)$$

where  $M$  is an arbitrary parameter at times 1 and 2.

In the following, pore pressure will be referred to simply as pressure, while maximum operating pressure of the injection pump (50 bar) will be referred to as maximum pressure.

#### 6.1.1 Velocity changes

Figure 6.1 shows the modeled changes in velocities for the reservoir sandstone as pore pressure and saturation increase. Relative changes in  $V_P$  shown in Figure 6.1a is most influenced by variations in saturation, with a maximum change of about -7% for saturation increase. Pressure increase, gives a maximal change of about -2%, while combined pressure and saturation effects, give a maximum change of about -10%. One might expect that the changes caused by saturation and pressure effects could be summed to give a total change of -9%. However, both density and bulk modulus of CO<sub>2</sub> increase with pressure (see Figure 3.2c ); for high saturations, the effect of the density increase is greater than the effect of bulk moduli increase, thus will the drop in velocity due to pressure increase be larger at higher saturations. This effect is also recognizable in the plots for AI, amplitude change and time shifts, as these all depend on the change in  $V_P$ .

For pressure variations below about 18 bar,  $V_P$  is nearly exclusively dependent on saturation. The reason for this is that few closed pores are opened before the pressure increase is above 18 bar. For pressure variations above this level, the velocity is highly pressure dependent.

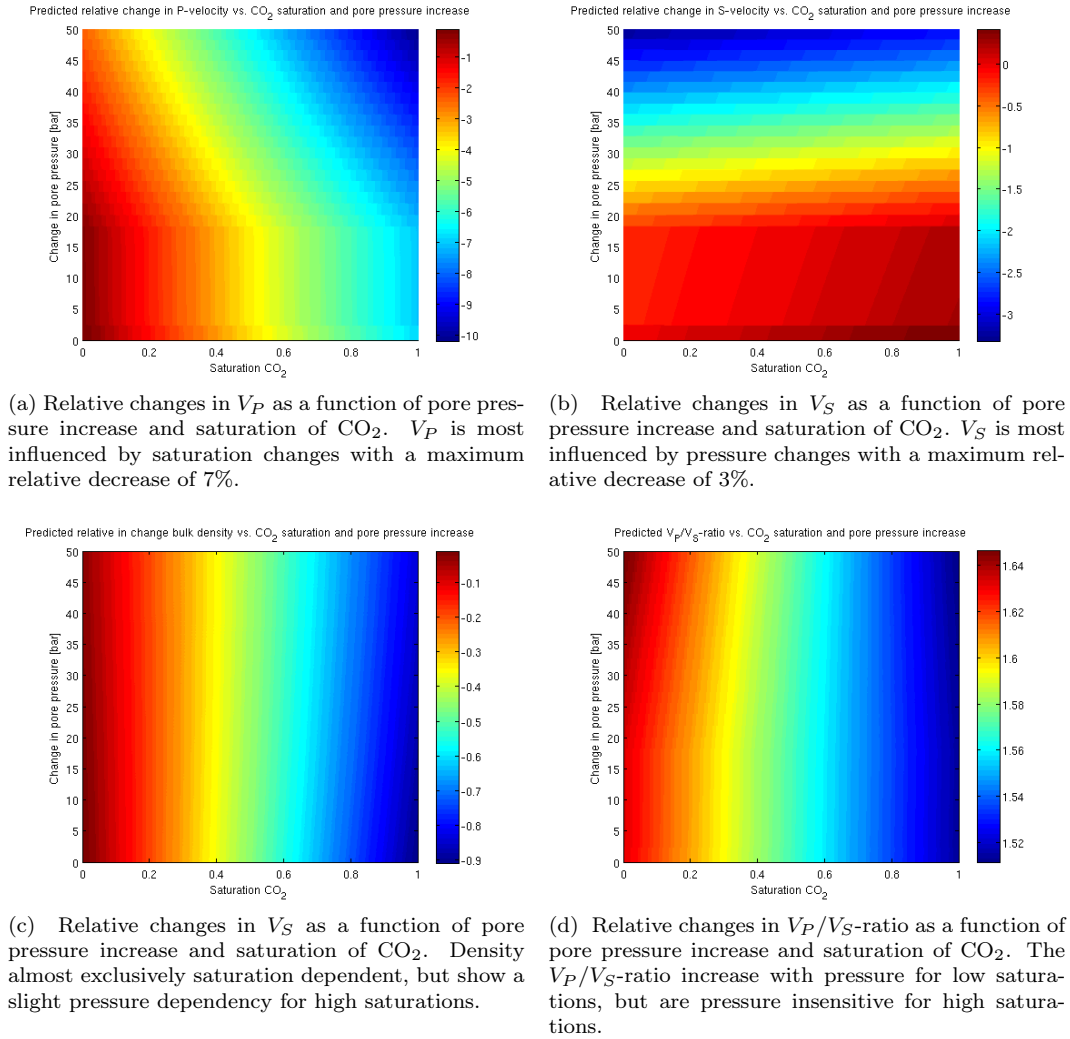


Figure 6.1: Predicted relative changes in  $V_P$ ,  $V_S$ , density, and  $V_P/V_S$  as a function of pressure changes and saturation.

Relative changes in S-velocity are much smaller than that of  $V_P$ . The changes are dominated by pressure variations, with a maximum change of -3% , and a maximum of +0.5% for saturation increase.  $V_S$  is in general only affected by saturation due to the decrease in bulk density. This effect is seen in Figure 6.1b; if  $V_S$  were only pressure dependent, the contours would be horizontal, but the density decrease slows down the rate of change caused by the pressure increase. For pressure variations below 18 bar the changes in  $V_S$  are positive, but as the pressure increases, pores start to open, velocity drops, and the change becomes negative.

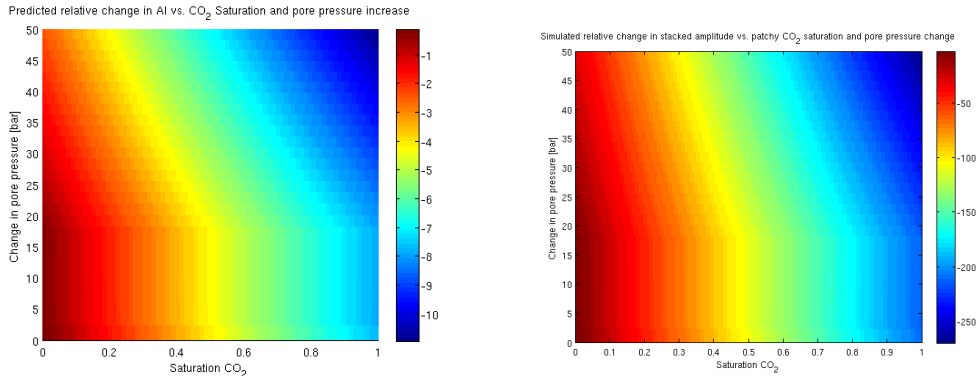
The bulk density of rocks are in general not pressure sensitive. This is because the variation in porosity due to pressure variations are insignificant. However, for high saturations of CO<sub>2</sub>, the bulk density becomes pressure sensitive. For constant pressure, the bulk density will decrease linearly with increasing saturation of CO<sub>2</sub>. However, when pressure increases, so does the density of CO<sub>2</sub>. The pressure sensitivity of CO<sub>2</sub> will have an increasing effect on the bulk density of the rock as saturation increases, thus will the bulk density become increasingly pressure sensitive with increasing saturation. This effect is recognizable in Figure 6.1c. For low saturations, the density is nearly exclusively dependent on saturation, with vertical contours, but as saturation increases, the density start to increase with increasing pore pressure, visible as tilted contours.

The  $V_P/V_S$ -ratio in Figure 6.1d is dominated by variations in saturation. If  $\text{CO}_2$  is injected without pressure build-up,  $V_P$  will drop, while  $V_S$  will increase slightly, leading to a decrease in  $V_P/V_S$ -ratio. For constant saturation, increasing pressure will cause both  $V_P$  and  $V_S$  to drop, but the relative decrease will be highest for  $V_S$ , resulting in an increase in  $V_P/V_S$ .

From Figure 6.1d it is also evident that the effect of pressure on  $V_P/V_S$  is most pronounced at low saturations. This can be explained by the pressure sensitivity of the bulk density; for high saturations, bulk density will increase with pressure. This will cause a reduction in both  $V_P$  and  $V_S$ , but for low saturations the density effect on  $V_P$  will be partly offset by the increase in  $\text{CO}_2$  bulk moduli. As saturation increases, this offset will be less influential, and  $V_P$  will decrease faster with increasing pressure, thus will the relative reduction in  $V_S$  not be higher than that of  $V_P$ , and the  $V_P/V_S$ -ratio will not increase.

### 6.1.2 Amplitude changes

Figure 6.2a shows the relative change in AI for variations in saturation and pressure. As can be expected, the plot for relative changes in AI, are nearly identical to that of  $V_P$ . The changes in AI are systematically higher than  $V_P$  though, with a maximum difference at full saturation without pressure increase. For As AI is the product of P-velocity and density, the difference between changes in AI and  $V_P$ , is proportional with the changes in density. The maximum change in AI for pressure increase is about 2%, for saturation increase the maximum change is about 7.5%, while combined pressure and saturation effects, give a maximum change of about -11%.

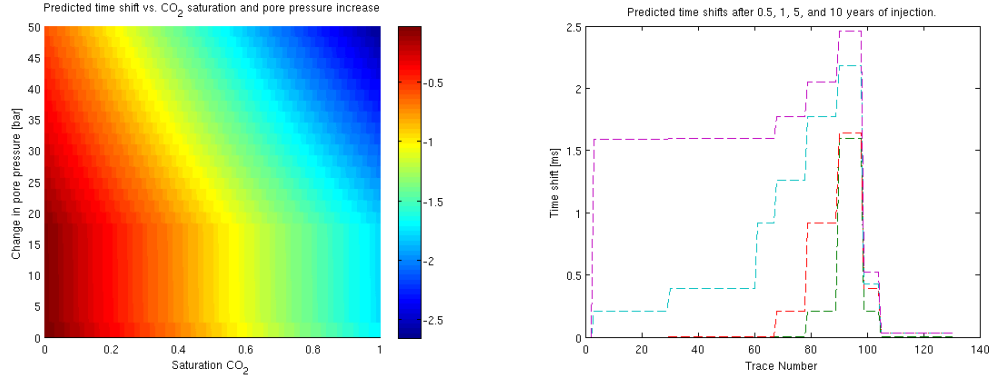


(a) Relative changes in AI as a function of pore pressure increase and saturation of  $\text{CO}_2$ . AI is most influenced by changes in saturation, with a maximum change of 7.5%

(b) Relative changes in stacked amplitude as a function of pore pressure increase and saturation of  $\text{CO}_2$ . The amplitude is most influenced by changes in saturation, with a maximum increase of 200%.

Figure 6.2: Predicted relative changes in AI and amplitude as a function of pore pressure increase and saturation of  $\text{CO}_2$ .

The relative change in reflected amplitude from the interface between the uppermost sandstone and the shale above, is shown in Figure 6.2b. At normal incidence, the relative change in amplitude is as much as 600% for full saturation and 50 bar of pressure increase. This extreme change in amplitude can not be seen in the stacked seismic sections. The reason for this, is that the reflection coefficient is offset dependent, and during stacking, the amplitude of each trace is summed, and the sum is divided by the number of traces. Normal incident amplitude changes will therefore tell little of the actual amplitude changes observed by seismic data. The offset corrected relative changes in amplitude in Figure 6.2b, represent stacked amplitudes for offsets up to 1500m. The maximum change for pressure increase is about 50%, for saturation increase the maximum change is about 200%, and for maximum saturation and pressure increase the change is 270%.



(a) Timeshifts as a function of pore pressure increase and saturation of CO<sub>2</sub>. Time shifts are most influenced by saturation changes, with a maximum shift of -1.7ms.

(b) Predicted relative changes in amplitude 0.5, 1, 5, and 10 years after injection start, plotted against the trace numbers of the synthetic seismic data. The time shifts increase as the CO<sub>2</sub> migrates in the up-dip direction.

Figure 6.3: Predicted time shifts as a function of pore pressure increase and saturation of CO<sub>2</sub>.

### 6.1.3 Time shifts

The predicted time shifts are shown in Figure 6.3a, the color scale is in milliseconds. As for the AI and amplitude changes, the plot for time shifts is nearly identical to that of  $V_P$ . This is to be expected as an assumption in the modeling is that the thickness of the CO<sub>2</sub> plume is constant, thus is  $V_P$  is the only variable in the time shifts. The maximum time shift for increase in pressure is -0.55ms, for saturation increase the maximum time shift is -1.7ms, and for full saturation and pressure increase the time shift is -2.65ms. The predicted time shifts after six months, one year, five years, and 10 years of injection are shown in Figure 6.3b.

### 6.1.4 AVO-signature

Figure 6.4 shows the predicted AVO signature for the interface between the upper reservoir sandstone, and the shale above it. The unbroken blue line represents the AVO signature for the base case, while the stippled blue line represents a 50 bar pressure increase. The dotted line represents a 100% CO<sub>2</sub> saturation, and the unbroken red line represents full CO<sub>2</sub> saturation and pressure increase.

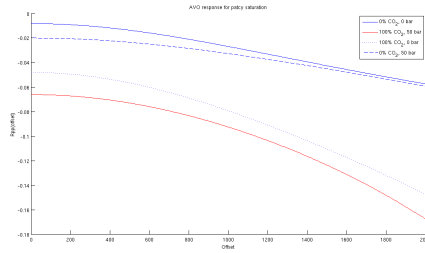
From this graph it is evident that a pressure increase will lead to small negative changes in intercept, and more pronounced positive changes in gradient. Saturation increase will give strong negative changes in both intercept and gradient, while maximum changes in both saturation and pressure, will give a strong negative change in intercept and an almost unaltered gradient.

These observations are supported by the plots in Figure 6.4b, and c. The intercept is by definition equal to that of the normal incident amplitude, and is only dependent on contrast in  $V_P$  and density across the interface. The gradient however, shows a clear correlation to the plot for S-velocity in Figure 6.1b. Pressure and saturation variations affect the gradient in opposite directions; pressure increases cause positive changes, and saturation increases cause negative changes. Along the diagonal from no change, to full saturation and pressure change, the two effects nearly cancel each other out.

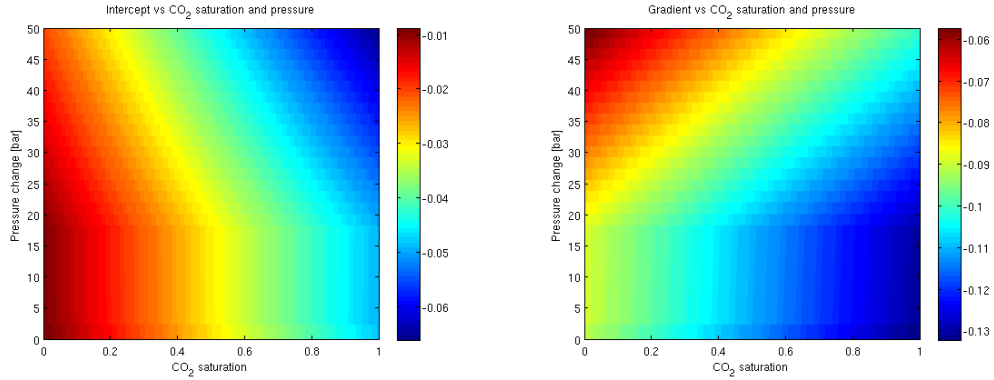
## 6.2 Synthetic seismic

Figure 6.5 shows the baseline synthetic seismic data. The synthetic data does not match the actual seismic data in an exact manner. It was not the aim to recreate the original data, therefore no





(a) Predicted AVO signature for different saturation and pressure states. The blue line represents no change, the stippled line represents a 50 bar pressure increase, while the dotted line represents full saturation, and the red line represent full saturation and pressure increase. Pressure changes give negative changes in intercept and positive changes in gradient. Saturation changes give negative change in both intercept and gradient.



(b) Predicted intercept as function of CO<sub>2</sub> saturation and pressure change. The intercept is most influenced by saturation changes. Both pressure and saturation increase lead to a negative change in intercept.

(c) Predicted gradient as function of CO<sub>2</sub> saturation and pressure change. The gradient is most influenced by pressure changes. Saturation and pressure changes have opposite effects on the gradient.

Figure 6.4: Predicted AVO signature for the upper reservoir sandstone.

quantitative comparison between the original and synthetic seismic was performed. However, some comments about the results are warranted. The major reflectors occur at the same depth intervals, and the relative amplitudes between the reflectors are within reasonable ranges. The pattern of smeared reflections described in the original seismic show strong similarities with the synthetic seismic. The reflection patterns from the intrusions also shows a high degree of similarities with the original seismic.

The reflection at 800m originate from Top Willhelmøya Subgroup/Isfjorden Member, while the reflection at 900m is the first reservoir sandstone. It is not possible to detect the thin 5m sandstone in the baseline survey. The next strong reflector, at 1000m is the third, 10m reservoir sandstone, and the strong reflector at 1100m is the basal, 20m sandstone. The two strong reflectors at 1200m are the intrusion. As described in Chapter 4.3, the anticlinal feature in Figure 4.2 was not modeled, hence the area of no reflections between the intrusions.

From the synthetic seismic the thickness of the upper sandstone is found to be 20m, while in the model it is 15m. This is because the tuning thickness at this reflector is about 22m, therefore thickness cannot be reliably resolved. As mentioned, the 5m sandstone is not detectable, and while the 10m sandstone *is*, the thickness can not be resolved. The basal sandstone shows a thickness of 20m, which is correct.

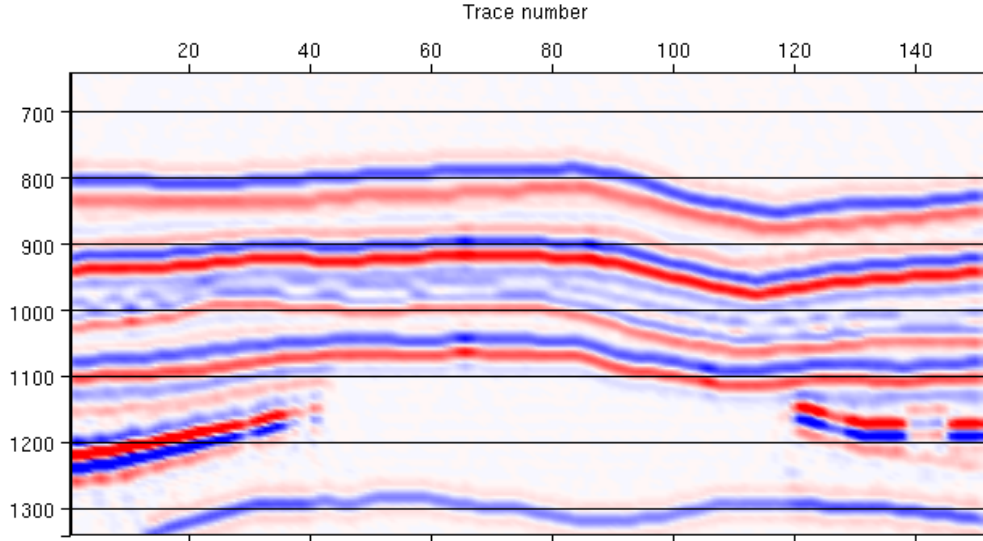


Figure 6.5: The baseline synthetic seismic. The upper reservoir sandstone is located at the reflector at 900m. The 5m sandstone is located in the interval of smeared reflections at 950-1000m. The 15m sandstone is located at the reflector at 1000m, while the basal 20m sandstone is located at the 1100m reflector.

The synthetic seismic shows diagonal streaks at several places, these are especially visible in difference sections. These are artifacts from the modeling, and seem to originate from the vertical separators in the reservoir sandstones.

### 6.2.1 Qualitative observations

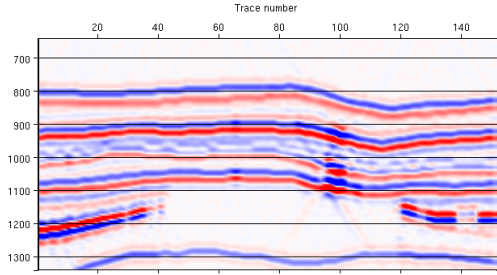
Synthetic seismic for the monitor surveys after six months, one year, five years, and 10 years of injection are shown in Figure 6.6 a,c,e and g. The difference sections between the baseline survey and the monitor surveys are shown to the right of it's respective monitor survey in Figure 6.6 b, d, f, and h.

The six months monitor survey is shown in Figure 6.6a. Here, the changes are evident as a series of strong amplitude anomalies at different depth levels around trace 100, where the well is located. These anomalies represent the CO<sub>2</sub> plume. It is possible to distinguish three separate layers with amplitude anomalies at approximately 920m, 1020m, and 1060m. There are also some amplitude changes in the interval between the uppermost and middle anomaly, but these are not clearly defined.

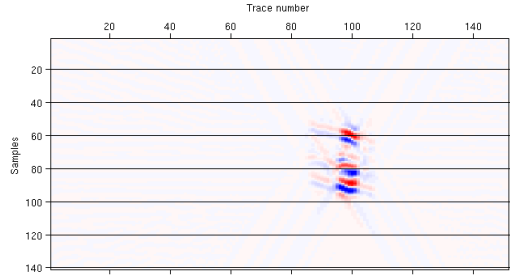
There is evidence of tuning effects at all three depth levels, but these are most pronounced at the lower two. Here the reflecting layer appears to have grown in thickness in comparison to the baseline, which is a common effect of tuning [Sheriff and Geldart, 1995]. The three distinguishable anomalies come from the three thickest sandstone units. The thin sandstone unit of 5m thickness, is below resolution and can therefore not be resolved.

The difference section in Figure 6.6b reveals some details not easily observed in the monitor section. In addition to the strong anomalies around the well, there are weak amplitude differences in both lateral directions, indicating small changes in saturation or pressure. From the difference section, the extent of the CO<sub>2</sub> plume is approximated to be 220m.

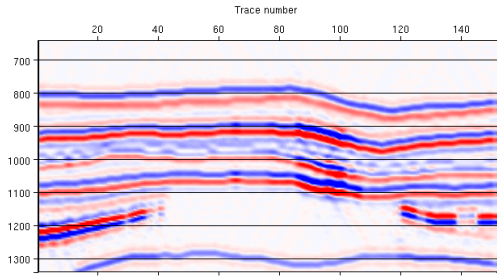
After a year, Figure 6.6c shows that the CO<sub>2</sub> has migrated to the left in the up-dip direction. The difference section in Figure 6.6d shows that the amplitude is strongest near the well, and



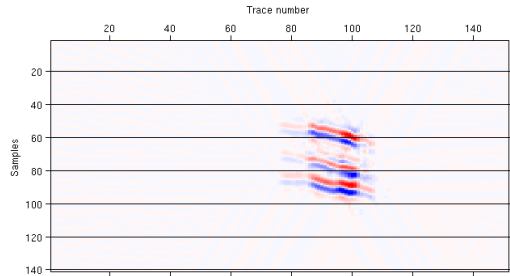
(a) Synthetic seismic six months after injection start. Amplitude anomaly is visible around trace 100. Tuning effects can be seen between the two lower sandstones.



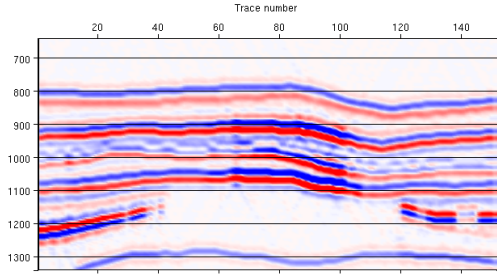
(b) Difference section six months after injection start. Strong amplitude anomalies around trace 100, weaker anomalies at both sides of this. The extent of the plume is approximately 220m.



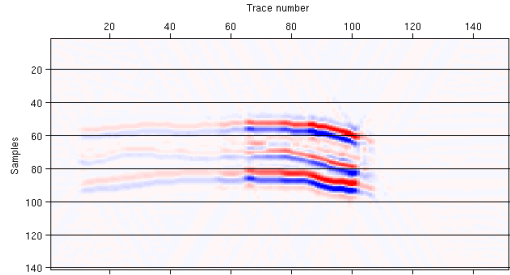
(c) Synthetic seismic one year after injection start. The 5m sandstone is detectable as an increased negative reflection in the 950-1000m interval.



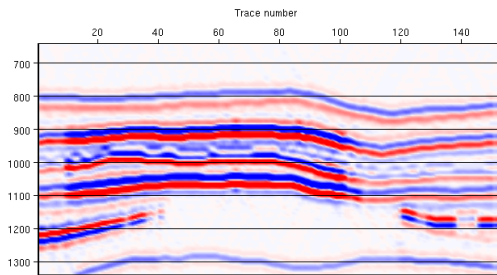
(d) Difference section one year after injection start. The amplitude anomalies have migrated 100m in the up-dip direction, giving a plume extent of 320m



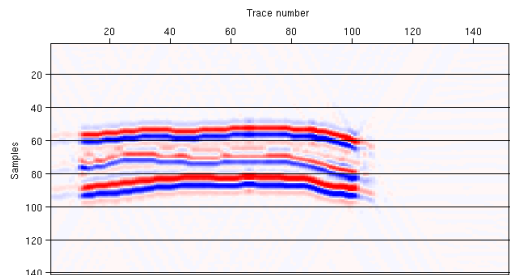
(e) Synthetic seismic five years after injection start. Several tuning effects are visible between the two middle sandstones in the 950-1000m interval.



(f) Difference section five years after injection start. Weak anomalies can be seen to the left of trace 60, indicating the presence of small saturations of CO<sub>2</sub>



(g) Synthetic seismic 10 years after injection start. The Amplitude anomaly now covers almost the entire length of the reflectors.



(h) Difference section 10 years after injection start. The plume now has an extent of about 1100m.

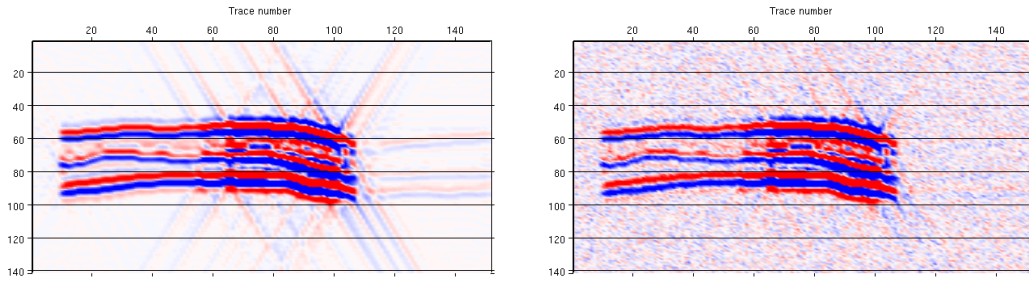
Figure 6.6: Synthetic monitor surveys and difference sections six months, one year, five years, and 10 years after injection start

becomes increasingly weaker in both directions. This indicates that the saturation of  $\text{CO}_2$  is highest near the well, and gradually decreases further out in the plume. The  $\text{CO}_2$  plume has migrated approximately another 100m since the last survey, and now has a lateral extent of approximately 320m.

The migration of the plume continues in Figure 6.6e. As the saturation of  $\text{CO}_2$  increase throughout the reservoir, several tuning phenomenon can be seen. The apparent thickness change of the basal sandstone follows the migration of the  $\text{CO}_2$ . Also, strong tuning effects can be observed at 900-1000m, between the two middle sandstones to the left of trace 60.

Finally, in Figure 6.6g, the  $\text{CO}_2$  has caused changes along the entire seismic section. The lateral extent of the  $\text{CO}_2$  is now approximated to be 1100m.

The scaling of the difference sections in Figure 6.6 does not allow for weak changes to be observed. As an example of how the scaling can affect the level of detail, a re-scaled version of the five year difference section is shown in Figure 6.7a. With this scaling, the details in the strong amplitude anomalies will disappear, while the weaker anomalies are enhanced. From this section it is evident that there also have been pressure or saturation changes to the right of the well. Figure 6.7b shows the same difference section with noise added. For  $\text{SNR}=2$ , the weak amplitude anomalies are no longer detectable in the difference section.



(a) Difference section after five years of injection for noise free data. Scaled to enhance weaker anomalies. Artifacts from modeling are visible as strong diagonal lines. It is evident that there also has been changes to the far right of the section. A weak amplitude anomaly was hidden by the previous scaling.

(b) Difference section after five years of injection for data with  $\text{SNR}=2$ . The weak anomalies are masked by the noise.

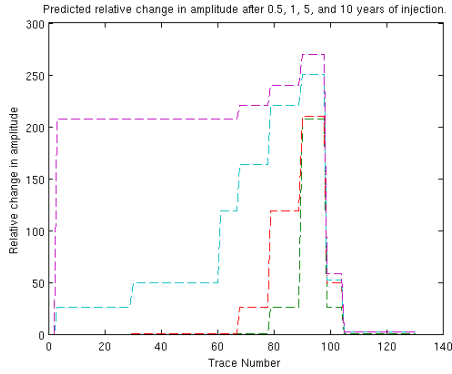
Figure 6.7: Comparison of difference sections with and without noise.

## 6.2.2 Quantification of changes

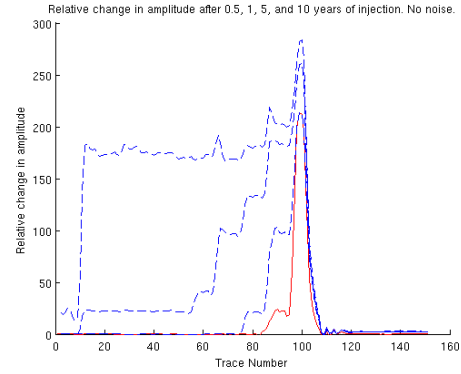
### Amplitude changes

The rock physical modeling predicts relative changes in amplitude for the monitor surveys as seen in Figure 6.8a. In this figure, the predicted differences in stacked amplitudes for six months, one year, five years, and 10 years, are plotted against the trace numbers of the synthetic seismic. The migration pattern from Figure 5.3 is easily recognizable, as  $\text{CO}_2$  migrates to the left, the amplitude changes accordingly. The staircase pattern is due to the way the model is built, there will be abrupt saturation and pressure changes across the vertical separators in the reservoir sandstones.

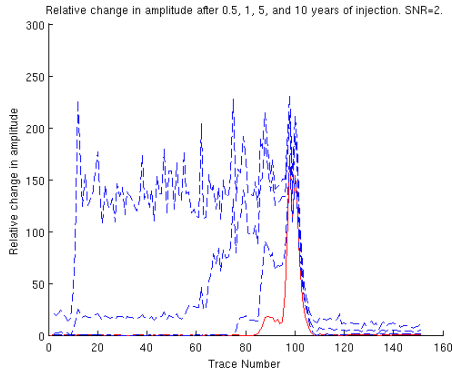
Figure 6.8b shows the relative changes in RMS amplitude for each synthetic seismic survey. These RMS-amplitudes was calculated in a time window across the reflection from the upper reservoir sandstone. The relative changes are calculated by the difference between the baseline survey and each of the monitor surveys. The pattern from Figure 6.8a is easily identified from the synthetic seismic data. However, the amplitude is systematically lower for the seismic data. The reason for this is in part that the amplitudes in the seismic are windowed RMS values, a better



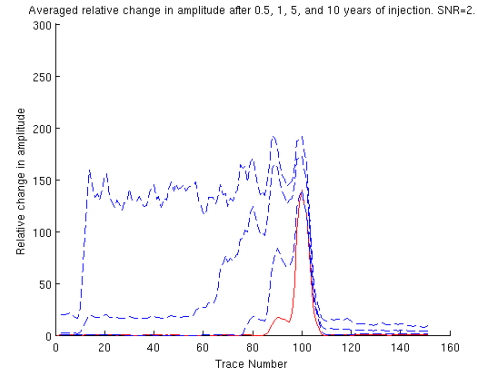
(a) Predicted relative changes in Amplitude after 0.5, 1, 5, and 10 years after injection start.



(b) Relative changes in Amplitude after 0.5, 1, 5, and 10 years after injection start. The values are calculated as RMS values windowed across the reflector for the upper sandstone. The amplitude show a high degree of correlation to the predicted values.



(c) Relative changes in Amplitude after 0.5, 1, 5, and 10 years after injection start with SNR=2. The masks the details of the amplitude changes, and the correlation to the predicted values drops. However, it is still possible to recognize the migration pattern.



(d) Relative changes in Amplitude after 0.5, 1, 5, and 10 years after injection start. The values have been calculated as the mean of three adjacent traces with SNR=2. This shows improvements compared (c)

Figure 6.8: Predicted and picked relative changes in amplitude.

fit would be achieved if the highest value within each window was picked. This however, would be very sensitive to noise in the data.

Figure 6.8c shows the amplitude change for SNR=2. Here it is still possible to see the general trend with increasing amplitudes as CO<sub>2</sub> migrates, but the details of the amplitude levels are obscured by the noise. Some improvement is gained by using an average of RMS values from three adjacent traces as shown in Figure 6.8d.

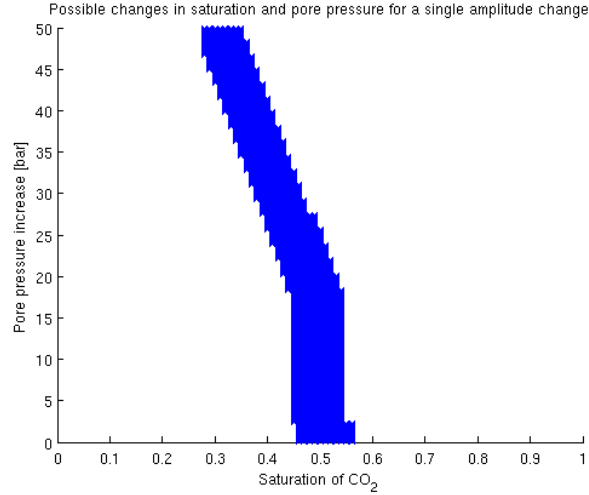


Figure 6.9: Possible values of saturation and pressure increase for the relative amplitude change for the uppermost sandstone at trace 70. The pressure range is 0-50bar, and saturations of 0.45 to 0.55.

The changes in amplitude in the noise free data, show a high degree of correlation to the predicted changes. However, it is not straightforward to invert these changes to obtain the pressure and saturation states that caused them. Figure 6.9 illustrates this point. Trace 70 after 5 years of injection have been chosen as an example. The figure shows all possible pressure and saturation states that could have caused an amplitude change that is within a range of 10% of the calculated RMS amplitude change. It is clear that the solution is highly non unique, with saturation values ranging from about 0.35 to 0.55, and pore pressure changes ranging from 0 to 50 bar. However, this non uniqueness can be reduced if other, independent measurements, such as AVO-analysis exist. Time shifts may provide additional information to narrow down the range of possible solutions. However, as timeshifts are directly dependent on  $V_P$  as well, this is not an independent measurement. In addition, reservoir simulations often act to narrow the range of solutions, so does down-hole well measurements.

### Time shifts

As mentioned, a complete time shift study was not performed. However, in order to further explore the example of trace 70 after 5 years of injection, two shot gathers were produced by ray tracing modeling in Norsar2D; one for the baseline survey, and one for the 5 year monitor. The traveltimes for the Top Permian reflector was picked for a low offset ray, yielding a timeshift of -1ms. Figure 6.10 shows the result of applying the 1ms timeshift to narrow down the possible solutions for the saturation and pressure state. The reduction in non uniqueness is considerable, narrowing down the possible saturations to about 0.35-0.55, and the pressure range to about 0-35 bar. Regardless of the reduction, the problem of non uniqueness persists. This illustrates the fact that information about P-waves alone can not separate between pressure and saturation effects.

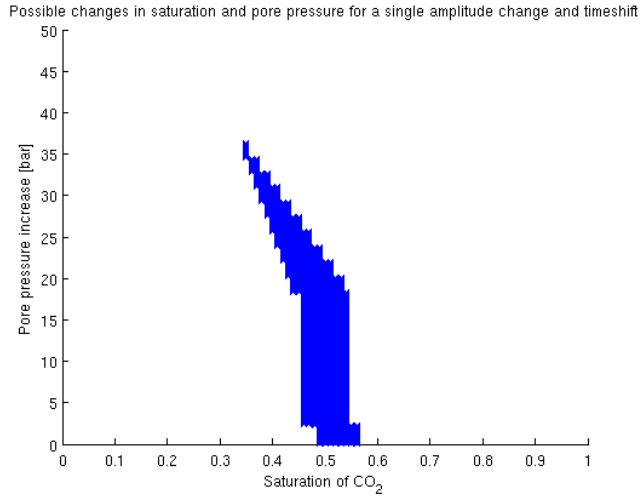


Figure 6.10: Possible values of saturation and pressure increase for the combined time shift, and relative amplitude change, for the uppermost sandstone at trace 70. The pressure range is now 0-35bar, and saturations of 0.45 to 0.55.

### AVO-analysis

Intercept and gradient for the synthetic seismic was approximated by scaled near and far stacks. The near stack was regarded as the intercept, while the difference between near and far stacks approximated the gradient. The approximated gradient was scaled to give an intercept/gradient-ratio as close to the predicted as possible, this scaling method is discussed by Landrø [2001]

To visualize the development of the intercept and gradient over time, the plot in Figure 6.11 shows the relative changes between each survey and the baseline for each reservoir zone. The horizontal axis represents the relative change in intercept  $\Delta R_0$ , while the vertical axis represent the relative change in gradient,  $\Delta G$ . The interpretation of this  $\Delta R_0/\Delta G$ -plot is best explained in table form; the + and - signs, indicate magnitude and polarity of change:

Table 6.1: Interpretation help for the  $\Delta R_0/\Delta G$ -plot. The signs indicate polarity and magnitude of the changes.

$\Delta R_0$	$\Delta G$	Dominating effect
++	-	Fluid effects
++	+	Fluid and pressure effects
++	++	Fluid and Pressure effects
+	-	Fluid effects
+	+	Pressure effects / Weak saturation and strong pressure effect
+	++	Pressure effects

Following the interpretation scheme in Table 6.1, the qualitative results for the AVO analysis can be summarized by the following list:

- Zone 1:
  - Six months: No change
  - One year: Small increase in gradient
  - Five years: Small increase in gradient
  - 10 years: Small increase in gradient

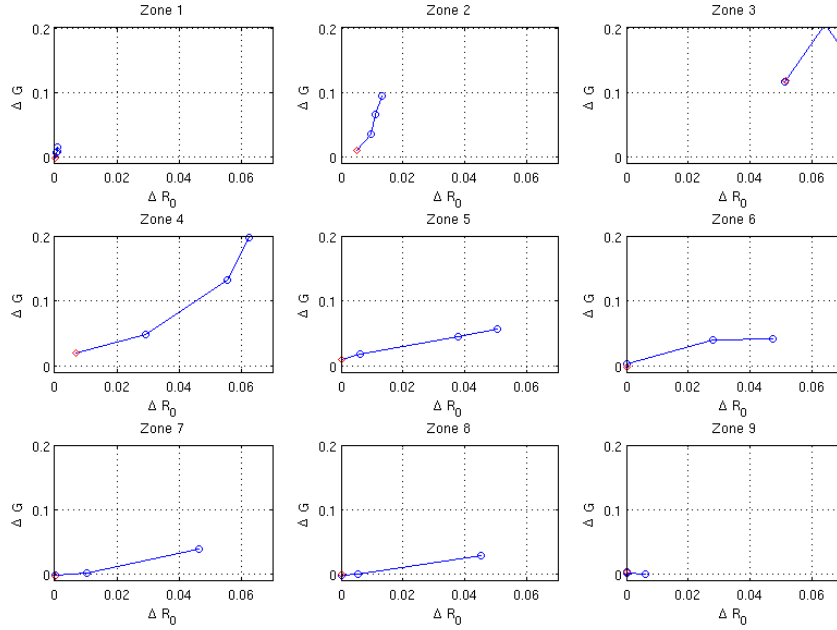


Figure 6.11: Intercept-Gradient crossplot for the reservoir zones; 0.5, 1, 5, and 10 years after injection start. Points marked with red represent the six month data. Zone 3 deviates strongly, suggesting a non existent pressure drop after 10 years.

Indicates no change for the first six months, and small pressure increase for subsequent surveys.

- Zone 2:
  - Six months: Increase in intercept
  - One year: Increase in intercept
  - Five years: Increase in gradient
  - 10 years: Increase in gradient

Indicates saturation changes the first year, and small pressure increase for subsequent surveys.

- Zone 3:
  - Six months: Large increase in intercept and gradient
  - One year: No change
  - Five years: Large increase in gradient
  - 10 years: Slight decrease in gradient

Indicates a large saturation increase after six months, pressure increase for the one year and five year survey, before a slight decrease in pressure in the 10 year survey.

- Zone 4:
  - Six months: Increase in intercept and gradient
  - One year: Increase in intercept and gradient



- Five years: Increase in intercept and gradient
- 10 years: Increase in gradient

Indicates saturation and pressure increase the first five years and pressure increase after 10 years.

- Zone 5:

- Six months: Increase in gradient
- One year: Small increase in intercept and gradient
- Five years: Large increase in intercept
- 10 years: Small increase in intercept and gradient

Indicates a small pressure increase the first six months, before a small saturation and pressure increase after one year, large saturation and small pressure increase after five years, and a small pressure and saturation increase after 10 years.

- Zone 6:

- Six months: No change
- One year: Slight increase in gradient
- Five years: Large increase in intercept and small increase in gradient
- 10 years: Large increase in intercept

Indicates a pressure increase between six months and one year, large saturation and small pressure increase after five and 10 years.

- Zone 7:

- Six months: No change
- One year: No change
- Five years: Small increase in intercept and gradient
- 10 years: Large increase in intercept and small increase in gradient

Indicates small increase in saturation after five years, large increase in saturation, and small increase in pressure after 10 years.

- Zone 8:

- Six months: No change
- One year: No change
- Five years: Slight increase in intercept
- 10 years: Large increase in intercept and small increase in gradient

Indicates small saturation increase after five years, large increase in saturation and small increase in pressure after 10 years.

- Zone 9:

- Six months: No change
- One year: No change
- Five years: No change
- 10 years: Small increase in intercept

Indicates a small saturation increase after 10 years.

The observations from the  $\Delta R_0/\Delta G$ -plot show a large degree of correlation to the expected behavior. Zone 3 stands out as a clear deviation, showing a decrease in pressure after 10 years, while the pressure actually increases in this time interval.

Although the general AVO-trend fit to the expected behavior for the modeled cases, the actual numerical values does not. Different scaling techniques was applied to calibrate the intercept and gradient to the predicted values, without success. As the calibration of the intercept and gradient did not succeed, the AVO-analysis can not be used directly to quantify time-lapse changes. However, the qualitative observations in the list above provide some useful information for the quantification example in Figure 6.9 and 6.10. Trace 70 is located at reservoir Zone 6. The  $\Delta R_0/\Delta G$  interpretation from this zone indicates a small pressure increase and large saturation increase after five years. From Figure 6.10, it is now possible to draw the conclusion that the time-lapse signal in trace 70 is caused by a CO<sub>2</sub> saturation of 0.45 to 0.55, and a pressure increase of 2-18 bar. The actual values are a CO<sub>2</sub> saturation of 0.5 and a pressure increase of 10 bar.

### 6.3 Leakage detection

Figure 6.12a shows the baseline survey of the overburden. The reflections at around 400m and 600m represent two aquifers in the Agardfjellet Formation and RurikFjellet Formation. For simplicity, no other layering is included in the overburden. In Figure 6.12c, two accumulations of CO<sub>2</sub> have migrated along fault zones as described in Chapter 5.2.2. The two accumulations are modeled to contain 100 tonnes of CO<sub>2</sub> each. This corresponds to a CO<sub>2</sub> saturation of 80% for the upper aquifer, and 10% for the lower. This gives a decrease in AI of approximately 5.5% and 2.5% for the upper and lower aquifer respectively.

The seismic data shows a clear anomaly in the upper reflector. Around trace 64, the reflector changes polarity. A windowed RMS across the reflector shows a relative change in amplitude of -120% at this anomaly. The apparent lateral extent of the anomaly is 110m. The lower accumulation is visible as a dim-spot around trace 60. This anomaly shows a relative amplitude change of -60%, and a lateral extent of 100m. The apparent lateral extents are much larger than the actual size of the CO<sub>2</sub> accumulations. This can be explained by lateral tuning effects, as the first Fresnel Zone for these reflectors are about 150m. Areas of change that are smaller than this, can not be resolved.

The difference section in Figure 6.12c clearly shows the two accumulations. Weaker amplitude anomalies are also apparent in the uppermost fault zone. These anomalies are one order of magnitude weaker than the anomalies for the accumulations. The difference section in Figure 6.12d shows the effect of adding Gaussian noise so that SNR=2. Here, the upper accumulation is still clearly visible, while the lower is hard to distinguish. The anomalies from the fault zone are not distinguishable.

How the geometry of the CO<sub>2</sub> accumulations affect its detectability can be seen in Figure 6.13. As described in Chapter 5.2.2, the accumulations are modeled as downwards pointing cones. Two cases are considered, one with a base diameter of 30m, and one with 100m. The results illustrate that laterally small and concentrated accumulations are more detectable than CO<sub>2</sub> distributed over a large but thin area. A 5% change in AI normally gives good time-lapse signals [Mikkelsen, 2008]. For the 30m diameter accumulation, this is achieved for accumulations as small as 25 tonnes for the upper aquifer, while the lower aquifer reaches full saturation before reaching a 5% change in AI. For full saturation, the accumulation in the lower aquifer will contain approximately 600 tonnes of CO<sub>2</sub>, and show a relative change in AI of approximately 4.5%.

For the 100m diameter accumulation in the upper aquifer, approximately 350 tonnes of CO<sub>2</sub> are needed for a 5% change in AI. Again, the accumulation in the lower aquifer reaches full saturation before a 5% change in AI. In this case the lower accumulation will contain approximately 6300 tonnes of CO<sub>2</sub> and show a relative change in AI of approximately 4.5%.

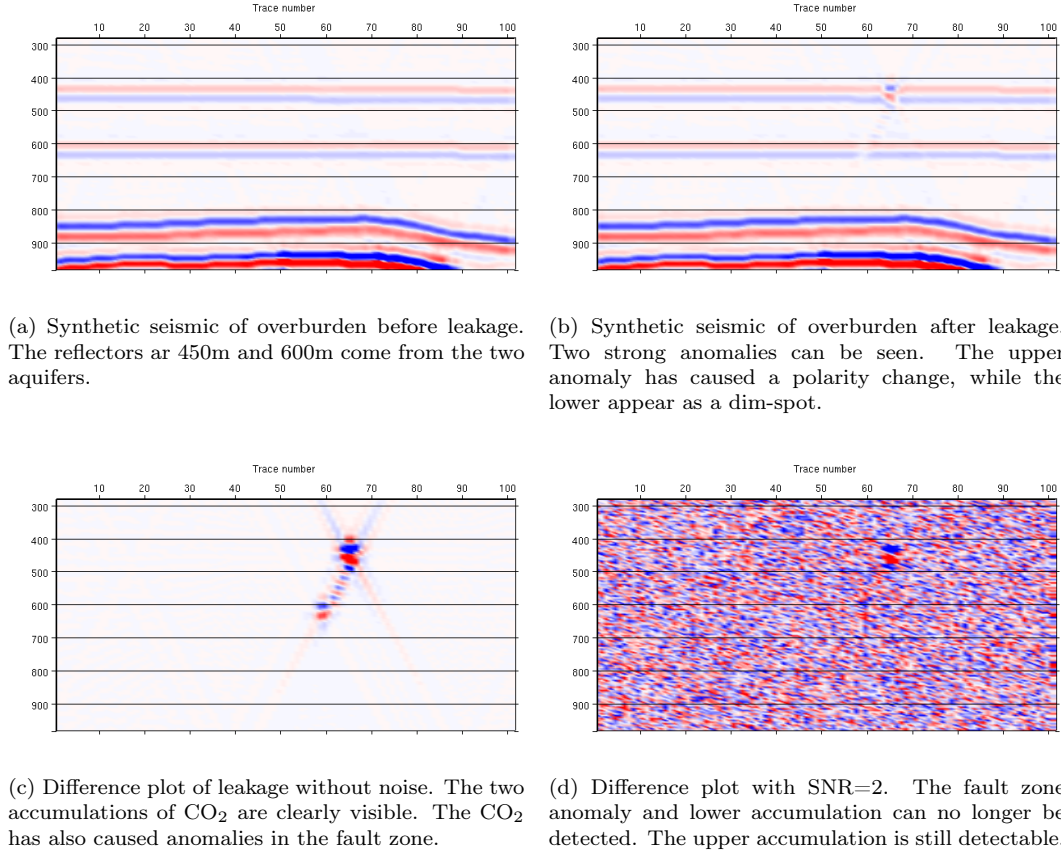


Figure 6.12: Synthetic seismic of overburden

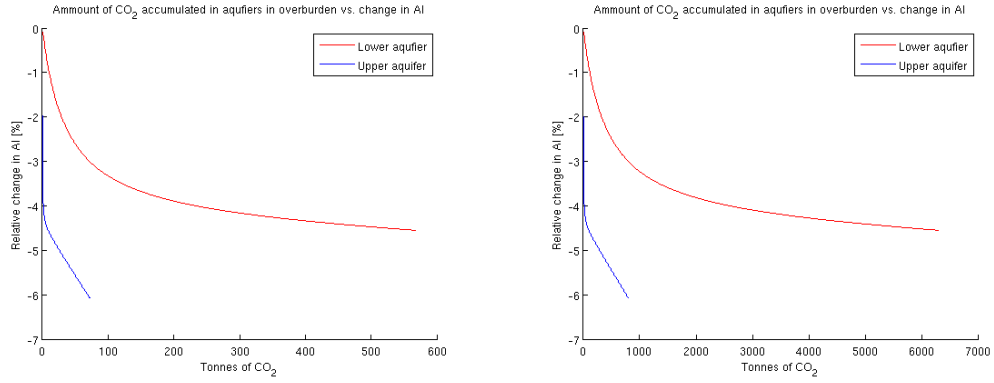
From these results it is possible to derive equations that approximate the volume of CO<sub>2</sub>,  $V_{CO_2}$ , that will give a 5% change in AI, as a function of the accumulation's radius  $r$ :

$$V_{CO_2}^{Upper} = 0.113r^2, \quad (6.2)$$

for the upper aquifer, and:

$$V_{CO_2}^{Lower} = 2.51r^2. \quad (6.3)$$

for the lower aquifer. If the radius is given in meters, the volume will be in tonnes.



(a) Relative change in AI as a function of volume of CO<sub>2</sub> for a 30x30m cone shaped accumulation. The relative change in AI for the upper aquifer, drops steeply to 5% for about 25 tonnes of CO<sub>2</sub>. The upper aquifer reaches full saturation at 600 tonnes, without reaching a 5% decrease in AI.

(b) Relative change in AI as a function of amount of CO<sub>2</sub> for a 100x100m cone shaped accumulation. The upper aquifer now can hold about 300 tonnes of CO<sub>2</sub> before reaching a 5% decrease in AI, while the lower holds about 6000 tonnes.

Figure 6.13: Synthetic seismic of overburden

# Chapter 7

## Discussion

Given the limitations in the data, it has been necessary to make a series of assumptions in this study. Some of these assumptions might limit the validity of the results in general, and some might limit the applicability to the Longyearbyen CO<sub>2</sub> Lab. Therefore, it is necessary to discuss the results from two different perspectives:

- Assuming that the seismic model and the rock physical model are representative: What is the feasibility of time-lapse seismic monitoring, given the obtained results?
- How does the assumptions made, affect the assesment of feasibility?

### 7.1 Feasibility of seismic monitoring

The feasibility of seismic monitoring will to a large extent depend on the repeatability of the seismic. Depending on which of the methods described in Chapter 1.1.2 are chosen, the repeatability will vary. A permanent array of receivers will give no uncertainty in positions, but suffer from a lack of flexibility. The reservoir can not be expected to contain any laterally sealing structures, therefore CO<sub>2</sub> might migrate over a large area. A permanently installed array will therefore have to cover a large area to ensure sufficient coverage of the migration, without being restricted to long offset surveys.

A more flexible method is the use of snow streamers. The repeatability of this method is not known. Efforts were made to obtain a repeated survey of snow streamer seismic during a seismic campaign at UNIS, spring 2009. This was not a priority of the campaign however, and so time did not allow for a repeated line.

Regardless of method, conditions in Svalbard are favorable for time-lapse seismic. The permafrost minimizes the need for weathering layer corrections, and attenuation is relatively low due to a high degree of consolidation [Eiken, 1985]. Johansen et al. [2003] showed that the thickness and amount of permafrost strongly affect the seismic quality. The upper one meter of the ground thaws in summer, but are frozen during the winter months [Christiansen, 2008], thus as long as surveys are performed in the winter, changes related to the weathering layer are not expected.

Misaghi et al. [2007] showed that the complexity of the overburden affects the repeatability. The strata in Adventdalen is close to horizontally layered, without strong heterogenities. The faulted zone encountered in the drill holes is heavily fractured, and might therefore have anisotropic velocities. Except from this, the overburden can not be described as complex.

The above discussion leads to the conclusion that the repeatability will to a large extent only be dependent on survey and equipment related issues. If source signature, positioning, and noise control are good, the repeatability will most likely be sufficient for monitoring.

### 7.1.1 Monitoring migration of CO<sub>2</sub> in the reservoir

All published results from seismic monitoring of CO<sub>2</sub> sequestration show strong amplitude anomalies in connection to the injected CO<sub>2</sub>. Among other projects, the amplitude anomalies have allowed the extent of the CO<sub>2</sub> plumes to be monitored at the Sleipner Field [Eiken et al., 2000; Arts et al., 2004], the Mc Elroy Field [Wang et al., 1998], and the Weyburn Field [Li, 2003]. The uncertainty of the feasibility of seismic monitoring in the Longyearbyen CO<sub>2</sub> Lab lies in the fact that the reservoir sandstone is expected to be of low quality. Low porosities are expected, and it has been speculated that the sandstone might have too high velocities and therefore be too stiff, to allow changes caused by CO<sub>2</sub> injection to be detectable. The results in this study contradict such claims.

The noise-free synthetic seismic presented in Chapter 6.2 show strong amplitude anomalies in areas where CO<sub>2</sub> has migrated. The front of the CO<sub>2</sub> plume can be tracked with a high degree of accuracy, and 5, and a pressure increase of 2-18 separate CO<sub>2</sub> accumulations of thickness down to 10m, can be distinguished.

The large relative changes in amplitude are in part due to the fact that the initial amplitudes are weak. This means that even though the relative change in amplitude is large, it still might not be detectable. A more robust measure of the detectability of an amplitude change, is the relative change in AI as this is independent of the contrast across the layer interface. For values below the contour line between 10% saturation and 30% pressure increase in Figure 6.2a, the change in AI is less than 1%. Experience from marine time-lapse seismic, show that changes in AI below 1%, are not detectable [Mikkelsen, 2008]. This means that areas where saturation is below 10% can not be detected.

By resampling seismic data, reliable time shift resolutions of about 1/10 to 1/20 of the original sampling-rate can be achieved [Eiken and Tøndel, 2005; Hagerty et al., 1999]. For a sampling-rate of 2ms, this corresponds to a detection threshold for time shifts of 0.1-0.2ms. Choosing the conservative limit, the predicted timeshifts exceed 0.2ms for the contour line between about 10% saturation and 25% pressure increase in Figure 6.3a. This means that time shifts can reliably be used as a monitoring attribute for saturations above 10%.

The modeled results are based on patchy saturation, if the saturation is homogeneous, both the 1% limit of AI and 0.2ms limit for timeshifts, are reached for saturations below 1%. The assumption of patchy saturation was made to reduce the number of variables in the modeling and can be justified by the following: Considering the low porosity, it is probable that some pores are isolated from the rest of the pore space, this in addition to the presence of cracks can lead to the saturation pattern being more patchy than homogeneous. It is however unlikely that the saturation will be either perfectly patchy or homogeneous, but rather somewhere in between the two. From this it can be concluded that the predicted time shifts and changes in AI, are conservative, and that the detection limit for saturation changes lies somewhere below 10%. The detection limit for pressure changes is not affected by saturation patterns, and is therefore found to be 25 bar by use of the time shift and amplitude changes.

The effects of heterogenities in the reservoir interval have not been treated in this study. Mikkelsen [2008] found that tuning effects increase with heterogenities present in the sandstone. This was found by modeling the seismic response of the reservoir sandstone with and without thin intrabed shale layers, the study also found that the reflected amplitude was reduced by 20% in the case of five, one meter thick shale layers within the sandstone. Such a reduction in amplitude would increase the the detection limit.

From the above discussion, a conservative conclusion is that seismic monitoring of the migration of the CO<sub>2</sub> plume is feasible, provided that the main body of the plume contains more than 10% saturation of CO<sub>2</sub>. If the saturation is not perfectly patchy, the detection limit will decrease.

### 7.1.2 Separating pressure and saturation effects and quantification of changes

The Results from the AVO-analysis show that some degree of separation between saturation and pressure effects might be achieved. The predicted intercept/gradient behavior fit the observed behavior in the synthetic seismic well for some areas, and poor for other areas. The intercept fits better to predicted values than the gradient. The best fits are found in areas that have been most influenced by only one effect. This indicates that AVO will most likely be able to separate areas where pressure increase is the dominant effect, from areas dominated by saturation changes, but may fail to separate the two effects in areas where both pressure and saturation has changed significantly.

Some of the discrepancy in the AVO-data, might be explained by tuning effects. Vertical tuning is known to be offset dependent [Xu and Chopra, 2007] and can therefore cause changes in the relative relationship between intercept and gradient. Horizontal tuning effects can also be influential. As the size of the zones are below horizontal resolution, tuning effects might originate from the abrupt changes across the dividers in the reservoir.

The artifacts visible in Figure 6.7a, might also influence the AVO-data. These diagonal amplitude anomalies spread out from the dividers in the reservoir. The angle of the diagonals are sufficiently low for the anomalies to interfere with the reflections from the reservoir. [Kvam and Landrø, 2005] found that synthetic intercept data is more reliable than the gradient data and argued that part of the reason for this, was due to the gradient being more susceptible to interfering wavefields. The results from this study are in agreement with their argument.

The AVO-behavior of Zone 3 was found to deviate strongly from the predicted. There can be several reasons for this. [Muerdter et al., 2005] showed that dipping reflectors can have substantial different AVO signature from flat lying beds. Zone 3 is located in the steepest dipping part of the model, with a dip of about  $13^\circ$ . Muerdter et al. found that these effects are important only when dip exceeds  $20^\circ$ . Therefore, the large deviation can hardly be credited to this alone. Zone 3 is located around trace 100, and as can be seen from Figure 6.7a, the artifacts from the modeling are strongest in this area. It therefore seems that the strong deviation in AVO-behavior in Zone 3 can be explained by interference from this modeling artifact.

Considering the fact that the AVO-analysis did not give conclusive results on separation of pressure and saturation effects, it seems obvious that a quantification of the same effects will not be possible. However, by a quantitative analysis of amplitude and time shift data, combined with qualitative observations from the AVO-analysis, the possible range of saturation and pressure states was considerably narrowed down. This can be further improved if independent measurements exist. Several monitoring wells are planned at the Longyearbyen CO<sub>2</sub> lab, if these wells are fitted with pressure sensors, the seismic interpretation models can be calibrated [Eiken and Tøndel, 2005; Landrø, 2001].

The synthetic seismic show tuning phenomenas between the separate sandstone units. The influence of these effects increase with increasing CO<sub>2</sub> saturation. All available outcrop logs show that the De Geerdalen Formation consist of a series of sandstones with varying thickness [Knarud, 1980], and although some of the sandstones are above tuning thickness, most are not. Thus it is expected that the tuning phenomenas observed in the synthetic seismic, will occur in real data. The quantification of CO<sub>2</sub> volumes have proven to be difficult at the Sleipner Field due to complex tuning phenomenas from several thin, sealing shale layers [Ghaderi and Landrø, 2009], as the velocities are much higher in the De Geerdalen than at the Sleipner Field, the tuning phenomenas will be an even greater issue. This will complicate the quantification of CO<sub>2</sub> volumes.

From the above discussion, the quantification of CO<sub>2</sub> from time-lapse seismic, is not feasible. The separation of pressure and saturation effects does not give conclusive results, thus is reliable separation not feasible either.

### 7.1.3 Detecting Leakage

The results from the leakage modeling show that the ability to detect leakage is critically dependent on the nature of the leakage. If a detectability limit of 5% change in AI is applied, the results show that leakages that migrate above the critical point of 500m, will be readily detectable for amounts as low as 25 tonnes. This result contradicts the findings of Chadwick et al. [2006b], who estimates a detectability limit of 600 tonnes for the same depth. This estimate is based on a comparison of repeatability noise to the amplitudes of small accumulations of CO<sub>2</sub>. Of course, detectability will be site dependent, but the results in this study also contradicts those of Hoversten et al. [2006]. In a modeling study, they found that the seismic data required a high signal-to-noise ratio in order to identify a 1000 tonnes of CO<sub>2</sub> at 1300 m and 1000 m, while at depths above the critical point, they found that accumulations of as little as 100 tonnes could be detected.

The synthetic seismic in Figure 6.12 show strong amplitude anomalies for an accumulation with a radius as small as 15m. An explanation for this surprising result can be the following: The model is implemented in 2.5D, thus will the properties be constant in the y-direction. This means that a 2D seismic line at any x-z crosssection, will produce the same results, thus is the coverage in the y-direction perfect. In a real survey geometry, this will not be the case. Even though a small accumulation of CO<sub>2</sub> might have sufficient change in AI to be detected, it is not likely that the coverage of the survey will be good enough to detect anomalies as small as 30m. It is also highly unlikely that the fault zone will be imaged in real seismic data, considering the thickness of one meter, and the dip of nearly 80°.

Following this discussion, it can be concluded that the results obtained for small accumulations of CO<sub>2</sub>, are too optimistic. The results for more widespread accumulations are more reasonable; an amount in the scale of 1000 tonnes will be detectable in the lower overburden, while amounts of a few hundred tonnes will be detectable in the upper overburden.

Equations 6.2 and 6.3 might still be valid if lower restrictions are imposed on the radius. Such a restriction could be derived from survey coverage and horizontal resolution limits. This has not been done.

## 7.2 On the validity of the results

Mikkelsen [2008] stated about the velocity of the sandstone that it: "... might be considered to be high, from this observation one might conclude, intuitively, that the rock is quite stiff. However, if seen in context of its porosity, the velocity is actually low." The reason for the relatively low velocity was speculated to be because of high clay content, high pore pressure, or crack porosity.

The description of mineralogy in Knarud [1980], shows no sign of high clay content, quite the contrary, there is an abundance of highly incompressible minerals. Also, Braathen et al. [2009] states that, based on experience from the previous drill holes, no overpressure is expected. It can therefore be stated that the most plausible cause for the low velocity, is crack porosity and/or low aspect ratio pores. The suggestion of crack porosity is further supported by the finds in the crack study, while the occurrence of low aspect ratio pores can be seen in thin-sections depicted in Knarud [1980]. The choice of method for the model was therefore limited to theories that allow non-spherical pores to be modeled.

Each of the various models described in Chapter 2.1, has its range in which it is valid. The contact theory of Hertz-Mindlin are best suited for high porosity rocks, and while the contact cementation model of Dvorkin and Nur aims to incorporate porosity reduction due to cementation, it is not suited in cases where cement fills large portions of the pore space [Dvorkin et al., 1999]. Inclusion models such as KT and DEM are better suited for low porosity rocks, and Draege et al. [2006] showed that DEM can be used to model diagenetic effects in rocks where cementation have almost completely filled primary porosity. For these reasons, inclusion models are considered the best option for the sandstone. Within the inclusion models, KT is not suited for this study, due to the restriction of non interacting pores. Figure 7.1 illustrates the impact of model choice on the velocity-porosity relationship. The critical porosity model, KT-model, and DEM-model are



plotted as a function of porosity. From this plot, it is evident that a simple averaging or heuristic model such as the critical porosity model, overestimates the velocity and are unsuited for this rock, while the KT- and DEM-model deviates only slightly from each other. The velocity drops quite steeply with porosity, due to the presence of the low aspect ratio pores.

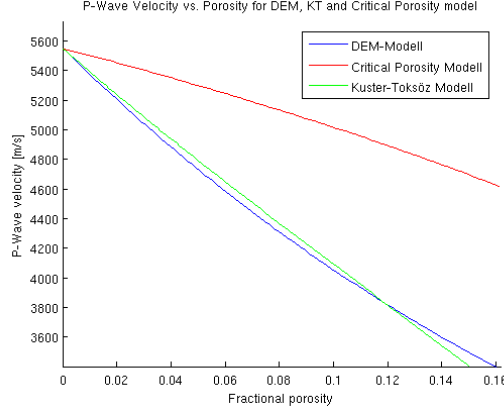


Figure 7.1: Velocity versus porosity for the sandstone modelled with DEM, Critical Porosity Model, and KT-model. Velocity drops steeply for the KT and DEM models due to presence of low aspect ratio pores.

Following this discussion, the choice of applying inclusion models, seem to be the best fit for the DE GEERDALEN sandstone, and indeed the only approach that can explain the low velocity-porosity trend.

The choice of method to model pressure dependency, have been somewhat constrained. The preferred method would be to use empirical data, but no such data exists for De Geerdalen sandstone. The theoretical methods that are easiest to implement, are the contact theories, as pressure is an explicit part of these equations. However, the contact theories are not suited for modeling of low porosity rocks, and thus are unsuited for this study. Therefore, the effects of pore pressure increase have been modeled by changes in pore geometry, and the opening of closed pores. The plots in Figure 6.1, show irregular shapes of the velocity curves. These staircase patterns are due to the opening of closed low aspect ratio pores as pore pressure increases. These sudden drops in velocity does not occur in laboratory measurements, the pressure-velocity curves are more continuous [Christensen and Wang, 1985; Todd and Simmons, 1972; Hoffman et al., 2005]. However, staircase pattern act as an approximation to the unlinear pressure-velocity relationship of porous rocks.

An important assumption in the pressure modeling, is that the rock contains a discrete set of closed low aspect ratio pores. As the pore pressure increase pores of an increasingly low aspect ratio will open. This has been implemented by adding dilute concentrations of pores as the critical pressure for each aspect ratio is reached. The amount of steps and size of the velocity drop for each step in the staircase pattern, are directly proportional to the predefined set of closed aspect ratio pores, and the actual concentrations added for each aspect ratio. The actual values for these properties can be calibrated for laboratory measurements [Toksöz et al., 1976], but in this study they have been chosen to fit laboratory data for other low porosity sandstones. Xue et al. [2005] found a decrease of 3% in  $V_P$  for a 100 bar pressure increase in the 12% porosity Takoa sandstone, they also found that the sandstone contained low aspect ratio pores. Shi et al. [2007] found a velocity decrease of about 11% for 100%  $\text{CO}_2$  saturation and pressure increase of 100 bar for the Takoa sandstone. These results fit well with the results in this study.

As the above discussion shows, the pressure sensitivity of the sandstone is purely an estimate based on results obtained for other sandstones of similar properties, thus is the validity of this result questionable. This impacts the assesment of feasibility for pressure/saturation separation,

and quantification, as the AVO-response will be highly dependant of the pressure sensitivity. For this reason, the assesment of feasibility in Chapter 7.1.2 is not absolute.

Two important assumptions that have been made during the rock physical modeling are that the mineral composition from Knarud [1980] and the P-velocity and density from the Reindalspaset log, are representative for the reservoir sandstone. The combination of data from these two sources form the basis of all rock physical modeling done in this study. The velocity data can be argued to be the least robust, as this originates from a single source and is only strictly representable for a very local area. If the actual P-velocity is considerably higher, this would cause the average pore aspect ratio to increase, and thus reduce the rock's sensitivity to CO<sub>2</sub> saturation and pore pressure increase. As an example, an increase of 5% in the initial P-velocity, would reduce the predicted relative change in AI for full CO<sub>2</sub> saturation, from about 7.5% to 5%. This shows that a large deviation from the assumed P-velocity, could invalidate the results in this study. However, uncertainties have been limited as much as possible by letting the data from the Reindalspaset well, restrain the possible ranges of compressibility and density calculated from the mineralogy data.

## Chapter 8

# Summary and conclusions

### 8.1 Summary and conclusions

This study has been aimed at assessing the feasibility of time-lapse seismic monitoring CO<sub>2</sub> sequestration at the Longyearbyen CO<sub>2</sub> Lab. The target reservoir is a saline aquifer in the De Geerdalen Formation. The feasibility of seismic monitoring is uncertain due to poor reservoir qualities. To do the assessment, four questions was raised:

- Will time-lapse seismic be able to monitor CO<sub>2</sub> migrating in the reservoir?
- Will time-lapse seismic be able to separate pressure and saturation effects?
- Will time-lapse seismic be able to quantify pressure states, and volumes of CO<sub>2</sub> in the reservoir?
- Will time-lapse seismic be able to detect small CO<sub>2</sub> accumulations leaked into the overburden?

The answers to these question was sought through building a rock physical model of the reservoir sandstone and a 2D seismic model of the reservoir. These models have been integrated, and seismic modeling have been used to produce synthetic seismic as CO<sub>2</sub> replace brine in the reservoir. Based on the available data, the DEM-model was found to be the most suitable for the rock physical modeling. The effects of pressure have been modeled by its effect on pore geometry and opening of closed low aspect ratio pores.

The seismic model is based on interpretation of seismic data. Four sandstone units have been defined within the reservoir, these units have been divided into nine zones to allow varying saturations and pressures in the lateral direction. The seismic modeling was performed by the SIMPLi algorithm implemented in the SeisRox software package, this algorithm is based on a spatial convolution technique. In addition to the baseline survey, five cases was modeled; six months, one year, five years and 10 years after injection start, as well as a case for leakage of CO<sub>2</sub> into the overburden.

The most important results from the modeling can be summarized:

- Changes in  $V_P$  is most influenced by variations in saturation, with a maximum change of about -7% for saturation increase. Pressure increase, gives a maximal change of about -2%.
- Changes in  $V_S$  are dominated by pressure variations, with a maximum change of -3% , and a maximum of +0.5% for saturation increase.
- Maximum change in amplitude for pressure increase is about 50%, for saturation increase the maximum change is about 200%, and for maximum saturation and pressure increase the change is 270%.

- The maximum time shift for increase in pressure is -0.55ms, for saturation increase the maximum time shift is -1.7ms, and for full saturation and pressure increase the time shift is -2.65ms
- AVO-analysis show that pressure increase will lead to small negative changes in intercept, and more pronounced positive changes in gradient. Saturation increase will give strong negative changes in both intercept and gradient, while maximum changes in both saturation and pressure, will give a strong negative change in intercept and an almost unaltered gradient.
- Areas with saturations of CO<sub>2</sub> show strong amplitude anomalies in the synthetic seismic, and it is possible to observe the migration of the CO<sub>2</sub>. Strong tuning effects are evident at all reservoir units. The addition of noise masks the time-lapse signal from areas of small saturation/pressure changes.
- AVO-analysis of the synthetic data showed a large degree of similarities to the predicted AVO-behavior. Some large deviations were found though.
- By combining relative changes in amplitude, time shifts and qualitative AVO-observations, the possible range of saturation/pressure states causing a time-lapse anomaly, could be narrowed down to a range of CO<sub>2</sub> saturations of 0.45-0.55 and pressure increase of 2-18 bar.
- The leakage modeling show that volumes of 25 tonnes can be detected above 500m, while 600 tonnes are required at depths of 600-700m.

Based on these results, and the assumptions made in the modeling, the following conclusions was made in the discussion:

- If source signature, positioning, and noise control are good, the repeatability will most likely be sufficient for monitoring.
- Monitoring of migration is feasible given CO<sub>2</sub> saturations above 10%.
- Quantification of saturation and pressure changes are not feasible.
- Reliable separation of pressure and saturation effects are not feasible.
- Leaks in the order of 1000 tonnes will be detectable in the deep overburden, while leaks of a few hundreds of tonnes will be detectable above 500m.
- Pressure sensitivity is an estimate. For this reason, the assesment of feasibility of separation and quantification can not be absolute.
- If actual P-velocity deviates strongly from that found in the Reidnalspasset well, the results obtained in this study could be invalidated.

## 8.2 Future work

The possibilities for improvements and developments to this work, will grow as data from the new well becomes available. The following are suggestions for the continuance of this study:

- When drill cores from the reservoir are available, perform laboratory tests to establish empirical relationships of pressures and velocities.
- Study thin sections from drill cores to establish mineralogy and pore structures.
- Create more exact reservoir model as electrical logs from the new well is available.
- If the sandstone turn out to be heavily fractured, introduce anisotropy to the rock physical model.

- Perform detailed rock physical modeling of the aquifers in the overburden to enable better estimates of detectable leaked volumes. From studies of survey coverage, and horizontal resolution, derive empirical relations to establish detectability limits of leakages.
- Study the faulted zone encountered in Dh1-3. What are the consequences of anisotropy in this layer?

-

# References

- Andresen, A. (2007). Geology of Svalbard. Presentation, Svalex Resource CD.
- Arts, R., Eiken, O., Chadwick, A., Zweigel, P., van der Meer, L., and Zinszner, B. (2004). Monitoring of CO<sub>2</sub> injected at Sleipner using time-lapse seismic data. *Energy*, pages 1383–1392.
- Arts, R. and Winterhaegen, P. (2005). Monitoring options for CO<sub>2</sub> storage. In *Carbon Dioxide Capture for Storage in Deep Geologic Formations*, volume 2, pages 1001–1013. Elsevier.
- Berge, P., Fryer, G., and Wilkens, R. (1992). Velocity-porosity relationships in the upper oceanic crust: Theoretical considerations. *J. Geophys. Res.*, 97:15239–15254.
- Biot, M. and Willis, D. (1957). The elastic coefficients of the theory of consolidation. *J. Appl. Mech.*, 24:594.
- Braathen, A., Jochman, M., Mørk, A., and Hansen, F. (2009). Well programme: LYB CO<sub>2</sub> Dh4. Technical report, University Centre in Svalbard.
- Chadwick, A., Arts, R., Bernstone, C., May, F., Thibeau, S., and Zweigel, P. (2006a). Best practice for the storage of CO<sub>2</sub> in saline aquifers. Observations and guidelines from the SACS and CO<sub>2</sub>STORE projects. Technical report, SACS-CO<sub>2</sub>STORE.
- Chadwick, A., Arts, R., Eiken, O., Williamson, P., and Williams, G. (2006b). Geophysical monitoring of the CO<sub>2</sub> plume at Sleipner, North Sea. An outline review. *Advances in The Geological Storage of Carbon Dioxide*, pages 303–314.
- Cheng, C. (1978). *Seismic Velocities in Porous Rocks: Direct and Inverse Problems*. PhD thesis, Mass. Inst. of Technol., Cambridge, Massachusetts.
- Christensen, N. and Wang, H. (1985). The influence of pore pressure and confining pressure on dynamic elastic properties of Berea sandstone. *Geophysics*, 50:207–213.
- Christiansen, H. (2008). Interannual variations in active layer thickness in Svalbard. In *Proceedings, 9th International Conference on Permafrost, Fairbanks Alaska*.
- Coueslan, M. (2007). Processing and interpretation of time-lapse vertical seismic profile data from the Penn West CO<sub>2</sub> monitoring project. Master’s thesis, University of Calgary.
- Dallman, W. (1993). Geological map of Svalbard. 1:500.000 sheet 1G, Spitsbergen southern part.
- Dallmann, W., Kjærnet, T., and Nøttvedt, A. (2001). Geological map of Svalbard, sheet C95 Adventdalen.
- Dræge, A. (2001). Effekter av trykk på seismiske hastigheter - modellerte og observerte sammenhenger. Master’s thesis, The University of Bergen.
- Dræge, A. (2006). *Impact of Diagenesis on Seismic Properties of Siliciclastic Rocks*. PhD thesis, University of Bergen.

- Draege, A., Johansen, T. A., Brevik, I., and Draege, C. (2006). A strategy for modelling diagenetic evolution of seismic properties in sandstones. *Petroleum Geoscience*.
- Dvorkin, J., Berryman, J., and Nur, A. (1999). Elastic moduli of cemented sphere packs. *Mechanics of Materials*.
- Dvorkin, J. and Nur, A. (1996). Elasticity of high-porosity sandstones: Theory for two North Sea datasets. *Geophysics*, 61:1363–1370.
- Dvorkin, J., Nur, A., and Chaika, C. (1996). Stress sensitivity of sandstones. *Geophysics*, 61:444–455.
- Eastwood, R. and Castagna, J. (1983). Basis for interpretation of  $v_p/v_s$ -ratios in complex lithologies. In *Proceedings of 24th SPWLA annual logging symposium*, pages G1–G17.
- Ebrom, D., Buddery, D., Watts, G., and Taylor, B. (2006). Monitoring activities at In Salah. In *8th International Conference on Greenhouse Gas Control Technologies*, Trondheim Norway.
- EEA (2008). EEA Report No5, greenhouse gas emission trends and projections in Europe 2008. Technical report, European Environment Agency.
- Eide, J., Ree, R., and Rockman, P. (1991). Final well report 7816/12-1. Technical report, Hydro.
- Eiken, . and Tøndel, R. (2005). Sensitivity of time-lapse seismic data to pore pressure changes: Is quantification possible? *The leading Edge*, 24.
- Eiken, O. (1985). Seismic mapping of the Post-Caledonian strata in Svalbard. *Polar Research*, 3:167–176.
- Eiken, O., Brevik, I., Arts, R., Lindeberg, E., and Fagervik, K. (2000). Seismic monitoring of CO<sub>2</sub> injected into a marine aquifer. In *SEG, Calgary, International conference and 70th Annual meeting, Expanded Abstracts*.
- Elvebakk, G., Hunt, D., and Stemmerik, L. (2002). From isolated buildup mosaics: 3D seismic shed new light on upper Carboniferous-Permian fault controlled carbonate buildups, Norwegian Barents Sea. *Sedimentary Geology*, 152:7–17.
- Elvebakk, H. (2008). Borehole logging in CO<sub>2</sub> wells in Longyearbyen, Svalbard. Technical report, NGU.
- Gassmann, F. (1951). Über die elastizität poröser medien. *Vier. der Natur. Gesellschaft in Zurich*, 96:1–23.
- Ghaderi, A. and Landrø, M. (2009). Estimation of thickness and velocity changes of injected CO<sub>2</sub>-layers from prestack time-lapse seismic data. *Geophysics*, 74.
- Hagerty, M., Schwartz, S., Garces, M., and Protti, M. (1999). Analysis of seismic and acoustic observations at Arenal Volcane, Costa Rica, 1995-1997. *Journal of volcanology and Geothermal Research*, 101:27–65.
- Hashin, Z. and Shtrikman, S. (1963). A variational approach to the elastic behavior of multi-phase materials. *J. Mech. Phys. Solids*, 11:127–140.
- Hill, R. (1952). The elastic behavior of crystalline aggregate. In *Proc. Physical Soc., London*, number A65, pages 3349–354.
- Hoffman, R., Xu, X., Batzle, M., Prasad, M., and Pillitteri, A. F. A. (2005). Effective pressure or what is the effect of pressure? *The Leading Edge*, 24:1256–1260.

## REFERENCES

---

- Hoversten, G., Gasperikova, E., and Benson, S. (2006). Theoretical limits for seismic selection of small accumulations of carbon dioxide in the subsurface. In *8th International Conference on Greenhouse Gas Control Technologies*, Trondheim Norway.
- Johansen, T. (1990). *Relations Between Seismic Parameters and Rock Parameters*. PhD thesis, University of Bergen.
- Johansen, T., Digranes, P., Schaack, M., and Lønne, I. (2003). Seismic mapping and modeling of near-surface sediments in polar areas. *Geophysics*, 68:1567–7226.
- Johansen, T. and Gelius, L. (2008). GeoClass. E-Learning Module.
- Knarud, R. (1980). En sedimentologisk og diagenetisk undersøkelse av Kapp Toscana Formasjonens sedimenter på Svalbard. Master's thesis, University of Oslo.
- Koster, K., Gabriels, P., Hartung, M., Verbeek, J., Deinum, G., and Staples, R. (2000). Time-lapse seismic surveys in the North Sea and their business impact. *The Leading Edge*, pages 286–293.
- Kragh, E. and Christie, P. (2002). Seismic repeatability, normalized RMS, and predictability. *The Leading Edge*.
- Kuster, G. and Toksöz, M. (1976). Velocity and attenuation of seismic waves in two phase media. *Geophysics*, 39:587–618.
- Kvam, Ø. and Landrø, M. (2005). Pore-pressure detection sensitivities tested with time-lapse seismic data. *Geophysics*, 70:39–50.
- Landrø, M. (1999). Repeatability issues of 3D VSP data. *Geophysics*, 64:1673–1679.
- Landrø, M. (2001). Discrimination between pressure and fluid saturation changes from time-lapse seismic data. *Geophysics*, 66:836–844.
- Lecomte, I., Gjøystdal, H., and Drottning, Å. (2003). Simulated prestack local imaging: a robust and efficient interpretation tool to control illumination, resolution, and time-lapse properties of reservoirs. *Expanded Abstracts, SEG 73rd Annual Meeting*, pages 1529–1532.
- Li, G. (2003). 4D seismic monitoring of CO<sub>2</sub> flood in a thin fractured carbonate reservoir. *The Leading Edge*, 22:690–695.
- Mavko, G., Mukerji, T., and Dvorkin, J. (1998). *The Rock Physics Handbook, Tools for Seismic Analysis in Porous Media*. Cambridge University Press.
- Mikkelsen, E. (2008). Modelling of possible seismic response to CO<sub>2</sub> sequestration at Svalbard. Directed study report, Norwegian University of Science and Technology.
- Mindlin, R. (1949). Compliance of elastic bodies in contact. *J. Appl. Mech*, 16:259–268.
- Misaghi, A., Landrø, M., and Petersen, S. (May 2007). Overburden complexity and repeatability of seismic data: Impacts of positioning errors at the Oseberg field, North Sea. *Geophysical Prospecting*, 55:365–379.
- Mørk, A. (2008). CO<sub>2</sub> reservoir geology. Presentation status meeting, CO<sub>2</sub> Project at Svalbard, 25/10/2008, UNIS.
- Mørk, A. and Braathen, A. (2008). Permeability study of aquifers in CO<sub>2</sub> drill cores. Presentation status meeting, CO<sub>2</sub> Project at Svalbard, 25/10/2008, UNIS.
- Mørk, A., Dallman, W., Dypvik, H., Johannessen, E., Larssen, G., Nagy, J., Nøttvedt, A., Olaussen, S., Pcelina, T. M., and Worsley, D. (1999). *Lithostratigraphic lexicon of Svalbard*, chapter Mesozoic Lithostratigraphy. Norsk Polar Institutt.



- Muerdter, D., Kell, M., and Koughnet, R. (2005). The effect of reflector dip on AVO analysis. *SEG Expanded Abstracts*, 24:281.
- Nakrem, H. (2002). Sen-Paleozoiske revoppbygninger,-Svalbard og tilstøtende områder.
- Nur, A., Mavko, G., Dvorkin, J., and Gal, D. (1995). Critical porosity: The key to relating physical properties to porosity in rocks. *SEG Expanded Abstracts*, 14:878.
- Onishi, K., Ueyama, T., Matsuoka, T., Nobuoka, D., and Saito, H. (2007). Applying differential analysis to crosswell seismic survey for monitoring CO<sub>2</sub> sequestration. *SEG Extended Abstracts*.
- Rutqvist, J. and Tsang, C. (2002). A study of caprock hydromechanical changes associated with CO<sub>2</sub>-injection into a brine formation. *Environ Geol*.
- Schilling, F., Borm, G., Würdermann, H., Möller, F., and Kühn, M. (2009). Status report on the first European on-shore CO<sub>2</sub> storage site at Ketzin(Germany). *Energy Procedia*, 1:2029–2035.
- Sheriff, R. and Geldart, P. (1995). *Exploration Seismology*. Cambridge University Press.
- Shi, J., Xue, Z., and Durucan, S. (2007). Seismic monitoring and modeling of supercritical CO<sub>2</sub> injection into a water-saturated sandstone: Interpretation of p-wave velocity data. *International Journal of Greenhouse Gas Control*, 1:473–480.
- Skola, I., Pcelina, T., Mazur, V., and Al'ter, S. (1980). [New data on the composition and structure of the sedimaentary platform cover on the basis of materials from the drilling of a parametric hole at Grumantbyen]; translated from Russian. In *[Geology of the Sedimentary Platform Cover of the Archipelago of Svalbard. Collection of Scientific Papers]*. NIGA, Leningrad.
- Span, R. and Wagner, W. (1996). A new equation of state for carbon dioxide covering the fluid region from the triple-point temperature to 1100K at pressures up to 800Mpa. *J. of Phys. and Chem. Reference Data*.
- SSB (2008). Naturressurser og miljø. Technical report, Statistics Norway.
- Todd, T. and Simmons, G. (1972). Effect of pore pressure on the velocity of compressional waves in low-porosity rocks. *J. Geoph. Res.*, 77:3731–3743.
- Toksöz, M., Cheng, C., and Timur, A. (1976). Velocity of seismic waves in porous rocks. *Geophysics*, 41:621–645.
- Tsang, C., Birkholzer, J., and Rutqvist, J. (2008). A comparative review of hydrologic issues involved in geologic storage of CO<sub>2</sub> and injection disposal of liquid waste. *Environ Geol*.
- Urosevic, M., Sherlock, D., Kepic, A., and Dodds, K. (2007). Land seismic acquisition repeatability for time-lapse monitoring of CO<sub>2</sub> sequestration. In *19th International Geophysical Conference & Exhibition*.
- vanAlphen, K., vanVoorst, Q., Hekkert, M., and Smits, R. (2007). Societal acceptance of carbon capture and storage technologies. *Energy Policy*, 35:4368 – 4380.
- Vernik, L. and Hamman, J. (2009). Stress sensitivity of sandstones and 4D applications. *The Leading Edge*, 28:90–93.
- Wang, Z., Cates, M., and Langan, R. (1998). Seismic monitoring of a CO<sub>2</sub> flood in a carbonate reservoir: A rock physics study. *Geophysics*, 63:1604–1617.
- Xu, X., Hoffman, R., Batzle, M., and Tshering, T. (2006). Influence of pore pressure on velocity in low-porosity sandstone: Implications for time-lapse feasibility and pore pressure study. *Geophysical Prospecting*, 54:565–573.

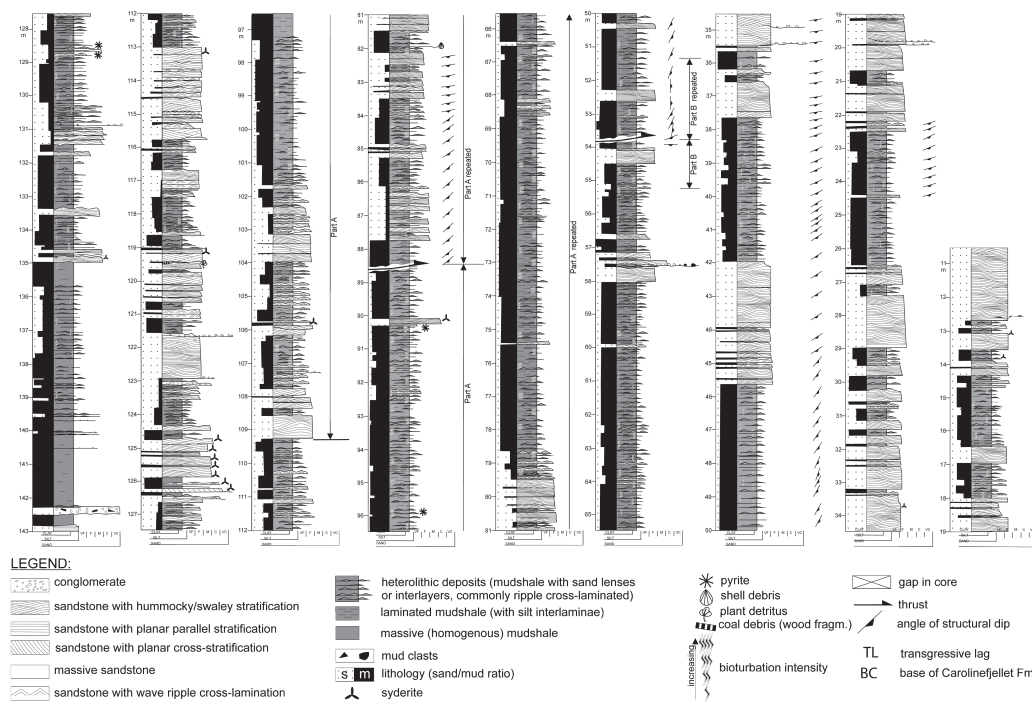
## REFERENCES

---

- Xu, Y. and Chopra, S. (2007). Improving AVO fidelity by NMO stretching and offset-dependent tuning corrections. *SEG Expanded Abstracts*, 26:234.
- Xue, Z., Ohsumi, T., and Koide, H. (2005). An experimental study on seismic monitoring of a CO<sub>2</sub> flooding in two sandstones. *Energy*, 30:2352–2359.
- Zimmerman, R. (1991). *Compressibility of Sandstones*. Elsevier.
- Zoeppritz, K. (1919). On the reflection and propagation of seismic waves. *Göttinger Nachrichten*, pages 66–84.

## Appendix A

### Lithological logs from drill cores in Dh2



Logged by Michal Warchol

Figure A.1: Carlinefjellet Formation

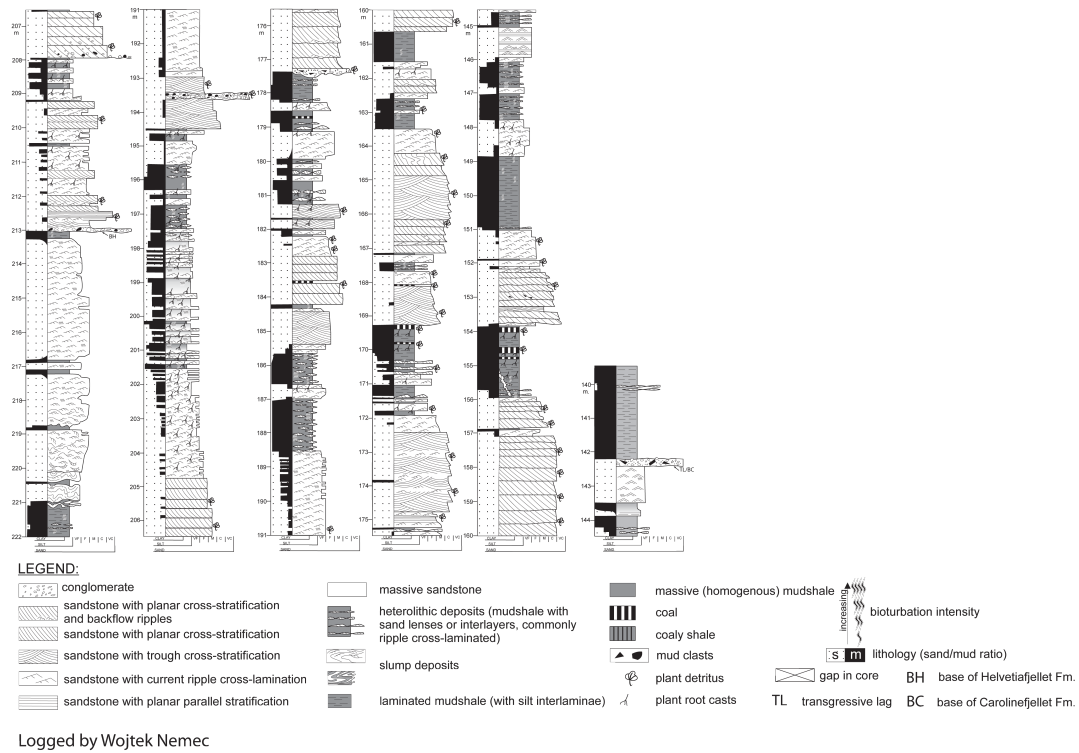


Figure A.2: Helvetiafjellet Formation

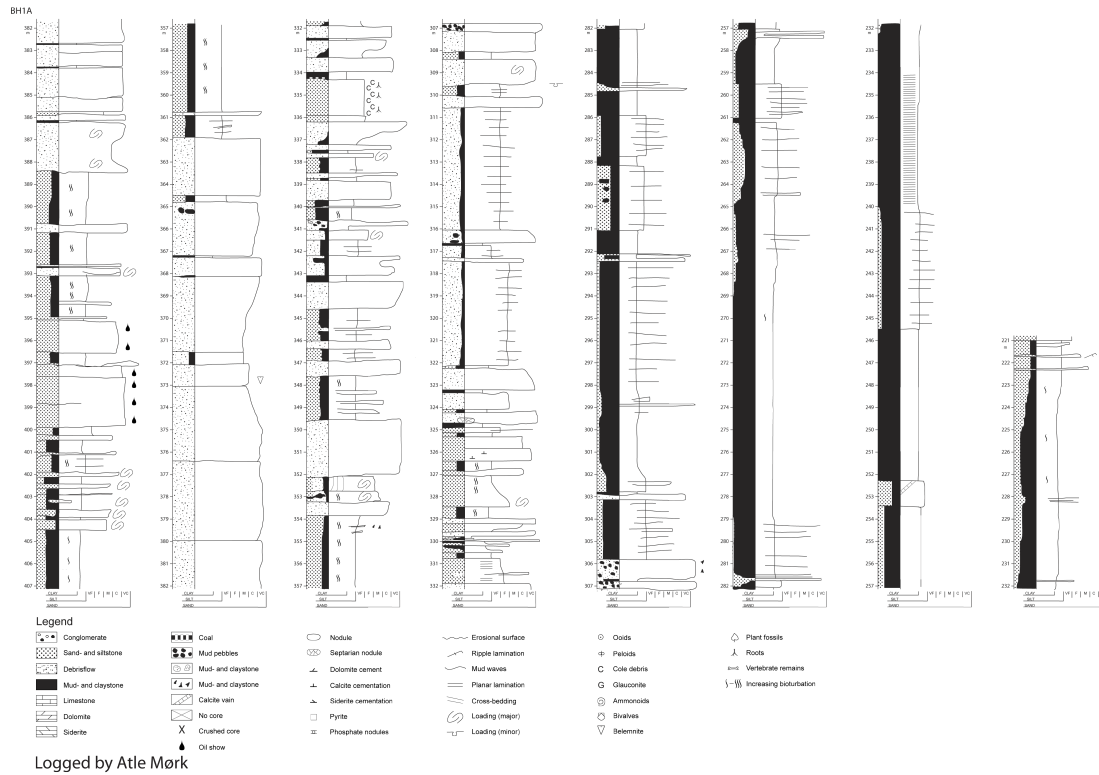


Figure A.3: Rurikfjellet Formation

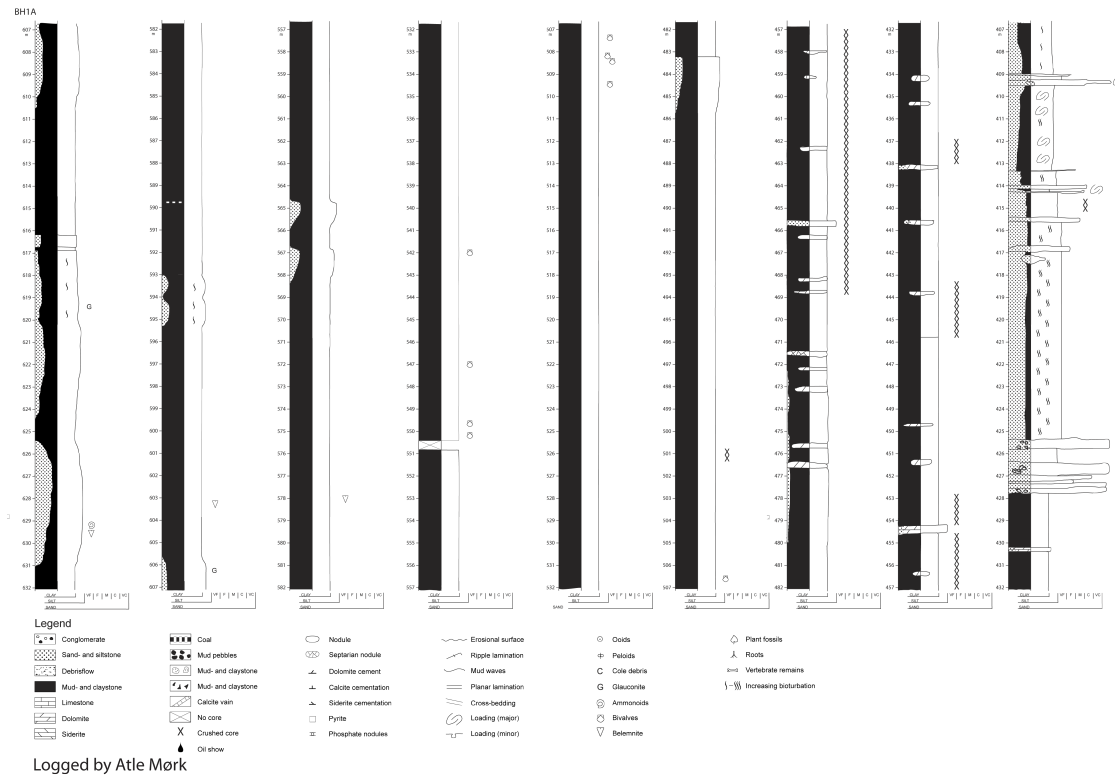


Figure A.4: Agardfjellet Formation

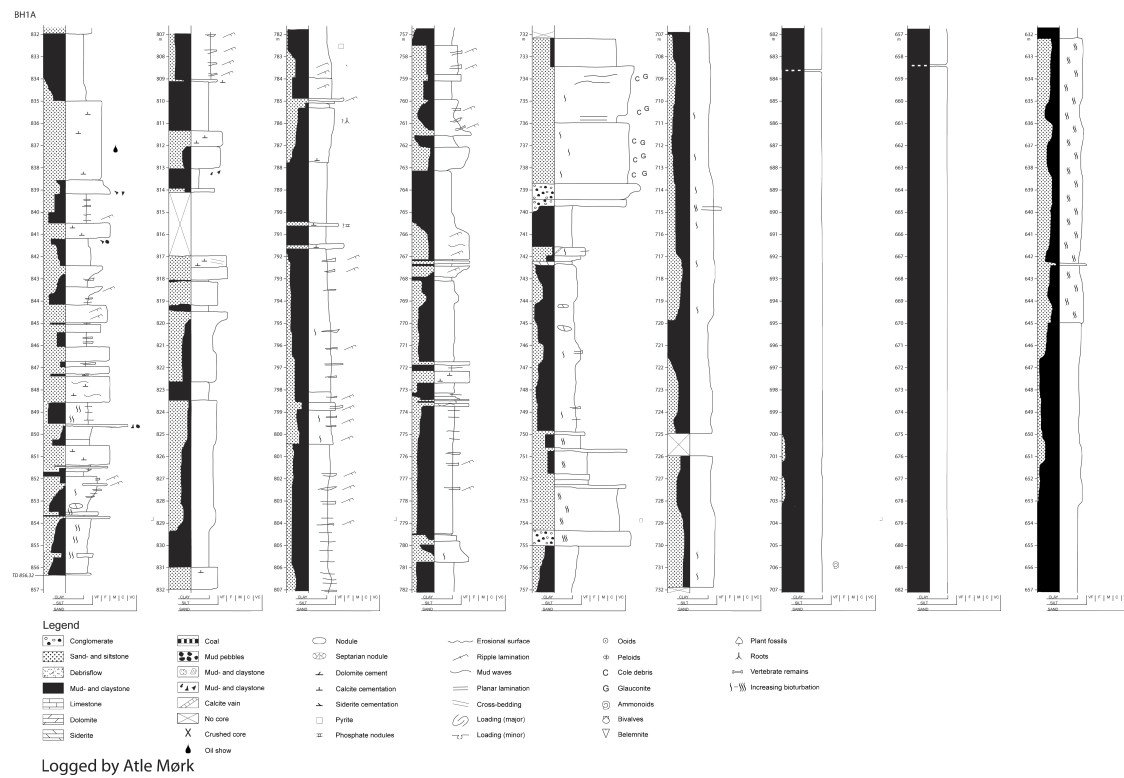


Figure A.5: Agardfjellet Formation, Willhelmøya subgroup, and Isfjorden Member



## Appendix B

### Electrical logs from Dh2

## APPENDIX B. ELECTRICAL LOGS FROM DH2

